

Master's Thesis

Development of Electrical Quality Assurance for Silicon
Vertex Detector in Belle II experiment

Department of Physics, University of Tokyo

Junya Sasaki

Aihara/Yokoyama lab.

February 2, 2015

Abstract

Belle II experiment is the upgrade of Belle experiment. Its purpose is to accumulate the data of integrated luminosity 50 ab^{-1} for searching the phenomena beyond the Standard Model. The center of mass energy of Belle II is 10.58 GeV. That statistics is 50 times larger than that of Belle (1 ab^{-1}). For launching Belle II, the upgrade of the detector and its read out system are now on progress. Silicon Vertex Detector (SVD) is one of the detectors in the Belle II, and SVD is composed of SVD “ladders”. We are now preparing for launching a mass production of SVD ladder. The main topic of this thesis is the method of the assembly of electrical working ladder. For achieving this, the way of the confirmation of the quality is necessary and detection of the problem not only during the assembly but also before and after the assembly is necessary.

Electrical Quality Assurance (EQA) is one of the most important procedures for SVD ladder assembly. In our SVD, quality inspection for all components is implemented, but also step by step electrical quality inspection during is implemented. EQA must be the procedure so that we can trace the quality of SVD ladder or detect the problems in the assembly procedure. Whole EQA procedure is supported by one DAQ system, called APVDAQ, developed by High Energy PHYSics (HEPHY) in Austria. This system can measure noises and gains in all strips and these parameters are the key for completing EQA procedure effectively.

There are mainly three steps in EQA, parts level EQA, assembly level EQA, and whole assembly level EQA. First in parts level EQA, we check the quality of all electrical components such as a read out chip, flexible circuit, and the sensor. Then bad or broken components are excluded by parts level EQA not to use it in a real SVD ladder assembly and only healthy components are used for a real ladder. If one electrical component doesn't work well, of course SVD ladder cannot show its true performance so we must check the quality of all electrical components before the assembly.

Second in assembly level EQA, electrical test is done during the assembly to confirm the quality of all electrical components or to detect the problems *step by step*; in the assembly procedure of SVD ladder, there are many procedures such as a wire-bonding, gluing, alignment of the sensor, and any other assembly procedures are so complicated that some problems are expected to be happen in one procedure. Especially, a wire-bond is so fragile that it is easily broken even by slight shock or by one assembly procedure. Although the number of a wire-bond is very huge, but we can check the condition of all wire-bonds in each wire-bonding procedure effectively by assembly level EQA; we check mainly each channel's noise by electrical test with APVDAQ. The problem during the assembly must be detected by this procedure.

Finally in whole assembly level EQA, a beta ray source test for an assembled ladder is implemented to check its performances; by this evaluation, we evaluate all channel's signal to noise ratio to check whether all channels are working well, or how many channels are not working.

To verify the constructed whole EQA procedure, we applied this procedure for the readable module assembly and we succeeded to detect the broken electrical components before the assembly. Also we succeeded to find out the problem of the broken line in a flexible circuit through that assembly procedure. Furthermore, we performed β -ray source test for an assembled readable module for evaluating its performances. As these procedures shown in above, its procedure allows us not only to trace the quality but also to detect the problems in each assembly procedure. In the SVD in Belle II, we demand a success rate of wire-bonding more than 99 percent. The EQA procedure which we constructed also enables us to achieve its severe requirement. We will see the whole procedure of the EQA, which promises the electrical quality of SVD ladder.

Contents

1	Introduction	3
2	Belle II Experiment	4
2.1	Physics of Belle II	4
2.2	Detector in the Belle II	5
2.3	Super KEKB Accelerator	7
3	Silicon Vertex Detector (SVD)	8
3.1	Requirement for the SVD Ladder	9
3.2	APV25 Readout Chip in Upgraded SVD	9
3.3	Structure of the Layer 6 Ladder	10
3.4	Components of the SVD Ladder	12
3.4.1	Double-sided Silicon Strip Detector (DSSD)	12
3.4.2	APV25 Read Out Chip	14
3.4.3	Origami flexible circuit	15
3.4.4	Pitch Adapter	16
3.4.5	Forward and Backward Module (FW and BW Module)	17
3.4.6	AIREX	18
3.4.7	Rib	18
3.5	APVDAQ for EQA	18
3.5.1	Read out chain	18
3.5.2	Components of APVDAQ	21
3.5.3	Function of APVDAQ Software	22
3.5.4	Calibration constant	24
3.6	Parameter for EQA	24
3.7	Chip on sensor concept	25
4	Assembly Procedure of the Ladder	26
4.1	The Role of EQA in the Assembly Procedure of the Ladder	27
4.2	Gluing PA1 and PA2 on a the DSSD, and wire-bonding	27
4.3	Alignment of Origami flexes, AIREXes, and the DSSDs and Gluing	28
4.4	Wire-bonding in N-side	29
4.5	Wrapping Procedure	31
4.6	Wire-bonding in P-side	31
4.7	Attachment of Origami Modules to Ribs	32
5	Procedure and Method of Study for EQA	33
5.1	Single-DSSD Readable Module for the Study of EQA	33
5.2	Class-D Ladder Assembly for the Study of EQA	34
6	Parts Level EQA	36
6.1	Assumption to Determine the Quality of the Origami flex and APV25	36
6.2	Method of Experiment	37
6.3	Result	39
6.4	Conclusion of Parts Level EQA	40

7	Assembly Level EQA	41
7.1	Study of the Assembly Level EQA	41
7.2	EQA in Start of the Assembly	42
7.3	EQA after Wire-bonding (inner-loop) in N-side	45
7.4	EQA after Wire-bonding (outer-loop) in N-side	48
7.5	EQA after Wrapping	50
7.6	EQA after Wire-bonding on the Bias Voltage Pad	50
7.7	EQA after Wire-bonding in (inner-loop) in P-side	51
7.8	EQA after Wire-bonding (middle-loops) in P-side	55
7.9	EQA in Wire-bonding (outer-loops) in P-side	57
7.10	EQA with a bias voltage after whole wire-bonding	59
7.11	Conclusion in Assembly Level EQA	63
8	Whole Assembly Level EQA	64
8.1	Setup of β -ray Source Test	64
8.2	Method of β -ray Source Scan	67
8.3	Run mode of APVDAQ in the β -ray source test	67
8.4	Fitting Method	69
8.5	Property of Tested Module	69
8.6	Cluster signal to noise ratio	69
8.7	Estimated capacitance	70
8.8	Cluster finding condition	71
8.9	Result of analysis	72
8.10	Strip by Strip Quality Inspection	79
8.11	Conclusion in Whole Assembly Level EQA	82
9	Conclusion	83
A	Diagnosis of Noisy Region in Single-DSSD Readable Module	84
A.1	Property of Assembled Single-DSSD Readable Module	84
A.2	Inspection by laser scan	87
A.3	Inspection by Probe test	88
A.4	Repair crack	89
A.5	Inspection of Short Connection	92
A.6	Result from The Diagnosis	93
A.7	Charge Distribution in the Laser Scan	94
B	Result of β-ray source test in the Single-DSSD Readable Module	96
C	Class-D Ladder : Detail Analysis in β-ray Source Test	100
C.1	Distribution of Peaking Time	100
C.2	Distribution of shaping time	102
C.3	Landau Fit for the Distribution of Cluster Charge	102
C.4	Asymmetry Cluster Charge between P-side and N-side	103
D	Noise and Position Resolution of the DSSD	105
D.1	Shot noise in the DSSD	105
D.2	Position Resolution of the DSSD	106

1 Introduction

Until now, almost all predictions of the Standard Model (SM) are found consistent with experimental results. The SM seems to be one of the most reliable theories to describe the phenomena. However, the SM cannot explain all of phenomena in this world; for example, a dark matter problem, a mass of neutrino, a hierarchy problem, a divergence of self energy of Higgs particle. To solve these problems, we expect the existence of a new phenomena beyond the SM, called a new physics. Many physicists are currently searching for new physics mainly by two methods. One is the direct search, and the other is the indirect search. The direct search means to search for new particle like a Large Hadron Collider (LHC) in Europe or like a cosmological measurement. The indirect search means to search the discrepancy between the SM prediction and the experimental measurement.

Purpose of the Belle II experiment is to search for new physics by using the latter way. The detail of Belle II is discussed in Chapter 2.

The Belle II detector is being developed and constructed. The Belle II detector consists of seven sub-detectors. In this thesis we focus on silicon vertex detector (SVD). This detector plays an important role in accessing to new physics through the time-dependent analyses by providing precise measurement of particle decay vertex. The detail of SVD is described in Chapter 3. The detector is barrel-like detector composed of SVD “ladders”. In Chapter 4, we describe assembly procedure of ladder.

In this thesis, we mainly discuss an Electrical Quality Assurance (EQA) procedure of ladder assembly. The purpose of EQA is to assure the electrical quality of ladder in each assembly procedure so that the assembled ladder works electrically and can hard up with the experiment. To achieve this target, this procedure is divided into mainly three steps.

First, in order not to use broken components for the assembly, we introduced a parts level EQA, which will be discussed in Chapter 6. We implemented electrical quality inspections for the components so that we can exclude the broken components. Also we distributed each component into three classes so that we can keep the good components for the real ladder assembly. Second, to track the electrical quality of ladder and to judge whether we can proceed to the next assembly step or not, we introduced an assembly level EQA, which will be discussed in Chapter 7. In these procedures, we make step-wise inspection of electrical connections of ladder step by step so that we can detect the problems during the assembly. Through the procedure in this step, we obtained the information about the behavior of channels in every assembly procedure, which allow us to detect the broken connections. Finally, to judge whether the assembled ladder is acceptable or not for the experiment, we introduced a whole assembly level EQA, which will be discussed in Chapter 8. In these procedures, a β -ray source test is introduced as the method of quality inspection. We check performance of assembled ladder mainly by detecting the signal from β -ray source. Also we implement the quality inspection channel by channel.

Finally, we conclude by using the result obtained from whole procedures of EQA in Chapter 9.

2 Belle II Experiment

The Belle II experiment is the upgrade of the Belle experiment in KEK (Tsukuba, Japan). The purpose of Belle II is to search new physics by its large statistics. The center of mass energy is $10.58 \text{ GeV}/c^2$, which is almost the same energy as the $\Upsilon(4S)$ mass, which decays into B meson pair.

The Belle experiment is famous for its large luminosity and the proof of Kobayashi-Maskawa theory. In the Belle experiment, they collected the data of integrated luminosity 1 ab^{-1} by using e^+e^- asymmetric collider called KEKB accelerator, which has a circle-like shape. Also the Belle experiment is famous for a lot of discoveries of new hadrons and the precise measurement of a branch fraction of decay modes which may include the contribution from new physics. Although the statistics of the data of Belle is large, it is still difficult to measure the contribution from new physics because of its small signature.

To overcome this difficulty, 50 times larger data than that of Belle will be collected in the Belle II experiment. The Belle II experiment has abundant possibilities in discovering of new physics. The Belle II is famous for not only its large statistics of B meson and other hadrons, but also lepton pair $\tau\tau$. Further statistics of the Belle II will lead us to new phenomena.

2.1 Physics of Belle II

Following physics are searched in the Belle II. Other examples are shown in [1].

- Charged Higgs (2 Higgs Doublet Model (2HDM) type II) in decay mode $B \rightarrow \tau\nu$ [1]
If there is charged Higgs particle, the branching fraction of $B \rightarrow \tau\nu$ is deviated from the value expected from the SM as this $BR_{total} = BR_{SM} \times (1 - (m_B/m_H)^2 \tan^2\beta)$ here $\tan\beta = v_2/v_1$ and these v_1, v_2 are vacuum expectation value appeared in the 2HDM type II (Because of the existence of the 2 doublet scalars, there are 2 vacuum expectation values), and m_B, m_H are the mass of B meson, the charged Higgs respectively.
- τ physics
The τ has a possibility of new physics. In general, the contribution from new physics is proportional to the square of mass, and the τ lepton has the largest mass in the leptons. Therefore, if there is a contribution from new physics, its influences will appear much stronger in the τ physics than other leptons. There are many things we are interested in; for example, anomalous magnetic moment of τ . For the electron and muon, its anomalous magnetic moment are consistent between the value from the SM and the measurement value from the experiment (However, anomalous magnetic moment of muon has a small discrepancy between value from the theory and the experiment). If some new particle couples with the τ , and if its contribution appears largely, then the anomalous magnetic moment of τ is deviated from the SM prediction.
- $b \rightarrow s\gamma$ [1]
The decay process $b \rightarrow s\gamma$ is expected to be sensitive to new physics: for example, dark photon, super symmetry (SUSY), charged Higgs, and other some models. The precise measurement of branching fraction of this process will be done precisely in the Belle II experiment.

2.2 Detector in the Belle II

The Belle II detector is composed by seven sub-detectors. To identify the type of the particle and to measure its energy, momentum, and decay vertex in the Belle II, following detectors are used.

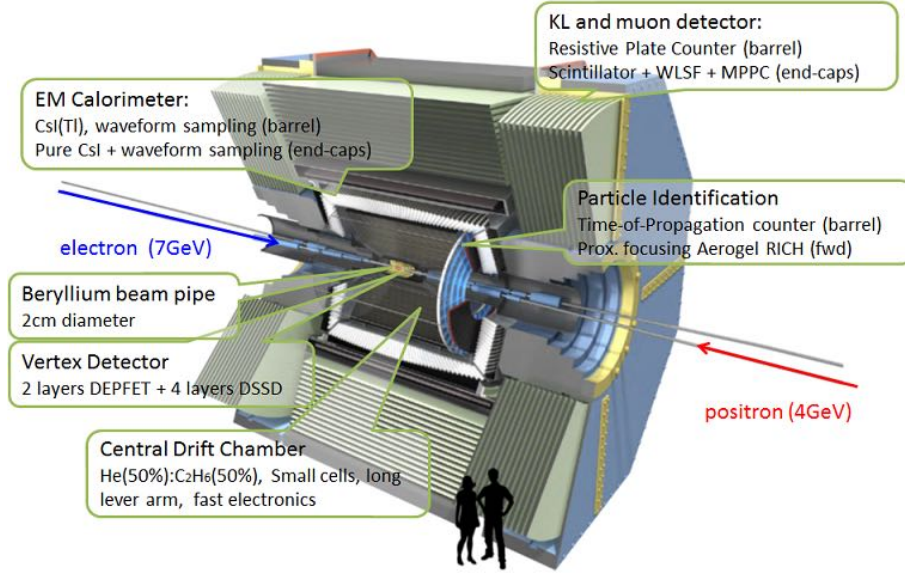


Figure 2.1: The Belle II detector [3].

- Pixel detector (PXD)

The PXD is an innermost detector that covers interaction point (IP) with the polar acceptance ranges from 17 degree to 150 degree. The PXD structure is composed of two layers, where one has that radius 14 mm and one has the radius 22 mm from the IP. The role of PXD is to measure a decay point of particles precisely by using the information of daughter particles. The impact parameter resolution is estimated $\sigma_z = 25 \mu\text{m}$ at 0.5 GeV/c. Although occupancy is expected in the PXD, the region of interest (ROI) from the SVD (see below) allows us to reduce its occupancy. Combining the PXD and the SVD, precise measurement of the vertex point is possible. It is important to access to a new physics through measurement of time dependent physics such as mixing-induced CP asymmetry.

- Silicon Vertex Detector (SVD)

The SVD is located outside the PXD. It is composed of four layers, of which radii are 38 mm, 80 mm, 104 mm, and 135 mm, respectively of which radii from the IP. Impact parameter of the SVD is $\sigma_z = 30 \mu\text{m}$ at 0.5 GeV/c. The SVD plays an important role for a reconstruction of K_S and a reduction of data size in the PXD by reconstructing particle hit position on the sensor. Also the SVD is important for the tracking and extrapolation by using the trajectory from the CDC (see below). By using an APV25 chip (described later) [6], not only a fast shaping time (time constant is 50 nsec) but also the deep pipeline for each read out line are possible. They are beneficial to prevent

the readout system from a pileup and high occupancy; in the innermost layer of the SVD, estimated occupancy is 6.7 % [7]. Furthermore, by combining it with the PXD, tracking of the particles with a low transverse momentum is possible, which is useful to reconstruct the particle from D^* meson efficiently.

- Central Drift Chamber (CDC)

The CDC is located outside SVD. Gas filled in the CDC are ionized by charged particles and generated ions are accelerated by the electrical field in the CDC and collected by the wires. By using the position of ionization we can know the trajectory of the charged particles. The CDC can measure the momentum of charged particles which is bent by the magnetic field of 1.5 T applied parallel to wire direction by the formulae $p(\text{GeV}/c) = 0.3B(\text{T})R(\text{m})$, here p is the momentum of charged particles, B is the magnetic field, and R is the radius of curvature.

The CDC also allows us to measure energy loss dE/dx .

- Time of Propagation counter (TOP)

The TOP is the particle identification detector which identifies charged kaon and charged pion by using the angle of its Cherenkov light. The TOP counter measures the differences of the velocity between those two particles, which is done by measuring the propagation time of the Cherenkov light inside the crystal of the TOP. The Cherenkov light generated in the crystal is reflected many times in the crystal surface and finally it reaches at the sensor put at its backward end.

- Aerogel RICH counter (ARICH)

The ARICH measures expansion of Cherenkov light with aerogel Cherenkov ring image detector. Due to the differences of velocity caused by mass differences between the charged kaon and the charged pion, the angle of emitted light is different with each other. The identification is done by Cherenkov ring image detector.

- Electromagnetic Calorimeter (ECL)

The ECL measures the energy of photon, and can identify the electron. CsI crystal is used for this detector because of its high light output. For the detection of photon, the ECL plays a crucial role. The intrinsic energy resolution of ECL is estimated as

$$\frac{\sigma_E}{E} = \sqrt{\left(\frac{0.066\%}{E}\right)^2 + \left(\frac{0.81\%}{\sqrt[4]{E}}\right)^2 + (1.34\%)^2}, \quad (2.1)$$

where E is in GeV.

- K_L and muon detector (KLM)

The KLM detects K_L and muon. The KLM is the outermost detector of Belle II and is located at barrel and endcap. Its structure is like a sandwich of iron and scintillator layers; iron plays a role of a return yoke scintillator detects the time-of-flight. A good time resolution of the scintillator allows us to measure the momentum precisely; in case of K_L has the momentum 1 GeV/ c , estimated reconstruction efficiency is 80% and its resolution of momentum is 18% [7].

2.3 Super KEKB Accelerator

The Super KEKB accelerator will have performance of the luminosity $8 \times 10^{35} \text{ cm}^{-2}\text{s}^{-1}$, which is the 40 times larger than that of Belle. The luminosity is described by the formulae shown in Eq. 2.2 and its parameter is shown in Tab. 1 [7].

$$L = \frac{\gamma_{\pm}}{2er_e} \left(1 + \frac{\sigma_y}{\sigma_x}\right) \left(\frac{I_{\pm}\xi_{y\pm}}{\beta_{y\pm}^*}\right) \left(\frac{R_L}{R_{\xi_y}}\right) \sim \frac{\gamma_{\pm}}{2er_e} \left(\frac{I_{\pm}\xi_{y\pm}}{\beta_{y\pm}^*}\right) \left(\frac{R_L}{R_{\xi_y}}\right) \quad (2.2)$$

Here, + and - denotes positron and electron respectively. γ represent the Lorentz factor, r_e represent the electron classical radius, and R_L, R_{ξ_y} represent a reduction factor for the luminosity and the beam-beam parameter. Other parameters are shown in Tab. 1. Since the ratio R_L/R_{ξ_y} is not far from unity, the dominant factor for the luminosity is therefore I , ξ_y , and β_y^* .

The Super KEKB accelerator has a ring-like shape and finite crossing angle of 83 mrad collision type (Fig. 2.2). Accelerated electrons from high energy ring (HER) and positrons from low energy ring (LER) collide each other at the interaction region (IR) located inside the Belle II detector. The electron beam energy is 7 GeV and the positron beam energy is 4 GeV. Lorentz-boost factor of the center of mass system is $\beta\gamma = 0.28$.

Severe background is expected in the Belle II because of large luminosity. The size of beam becomes much smaller as shown in Table. 1. Because of this, the Touschek effect become more severe and dominated the background near the IR of Belle II detector. The touschek effect is an intra-bunch scattering which is caused by Coulomb scattering between two electrons or two positrons. To reduce this background, the energy of electron and positron beam changed. Also, this change of energy is helpful to eliminate the emittance of HER/LER beams by increasing the life time of LER.

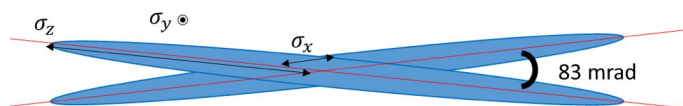


Figure 2.2: Image of the crossed beam.

Table 1: Information of beam [7]. Values in parentheses denote parameters at zero beam currents.

	LER (e^+)	HER (e^-)	unit
Beam Energy	4	7	GeV
Horizontal Beam Size σ_x	10.2(10.1)	11.2(11.1)	μm
Vertical Beam Size σ_y	48.3	61.8	nm
Vertical beam-beam parameter ξ_y	0.090	0.088	no unit
Vertical beta function at the IP β_y^*	0.27	0.41	mm
Beam current I	3.60	2.62	A

3 Silicon Vertex Detector (SVD)

The SVD [7] is located at the center of Belle II detector. The SVD measures the vertex point as shown in Fig. 3.1. As shown in the figure in next page, the SVD has a four-layer structure. Detailed geometrical information of each layer is listed in the Tab.2. Layer 1 and 2 are the PXD, Layer 3 - 6 are the SVD. The Lorentz-boost of $\beta\gamma = 0.28$ enables us to measure the difference of the flight length of two B mesons with an accuracy of $\sim 100 \mu\text{m}$ as shown in Fig. 3.2. This accuracy of the flight distance corresponds to an accuracy of the flight time of a few picoseconds.

The SVD also be used to reduce the data size in the PXD. Because of high occupancy in the PXD, it is difficult to distinguish the true signal from other backgrounds only by the PXD. Combining the performances of the PXD and the SVD, we can eliminate the background. Furthermore, its combination enables us to reconstruct low transverse momentum (a few tens of MeV/c) tracks, which do not leave so much hits in the CDC. The low momentum tracks are very important to reconstruct D^* mesons, which is used to tag its parent B meson flavor.

The SVD is essential to reconstruct K_S for the channels such as $B \rightarrow K^*\gamma$, $B \rightarrow K_S K_S K_S$. The detail of the SVD is written in [7].

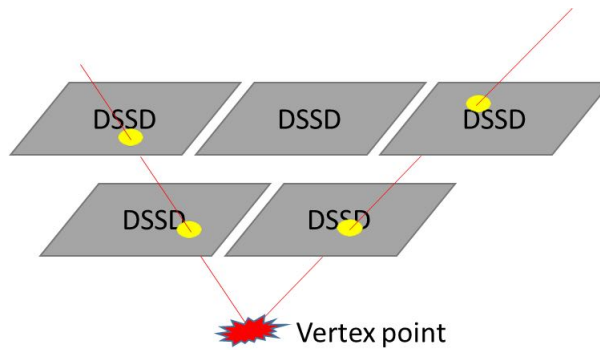


Figure 3.1: Image of measurement of vertex point.

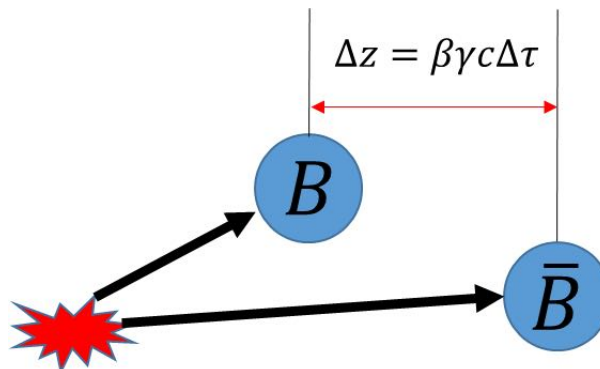


Figure 3.2: Image of difference of time-of-flight. We measure this time-of-flight between B meson pair.

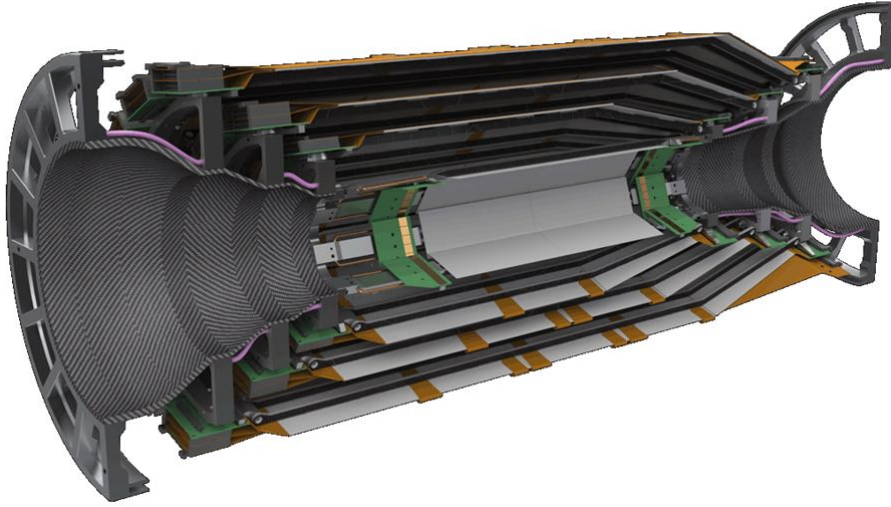


Figure 3.3: The cross-sectional view of the SVD in the Y-Z plane [3]. The beam direction is Z, and vertical direction is Y. The 4-layer structure of SVD is seen.

Table 2: The geometrical information of each layer.

Layer	Radius [mm]	Ladders	DSSDs/Ladder	Slant	Windmill angle [deg]	Overlap [%]
6	135	16	5	yes	9	9
5	104	12	4	yes	5	3.8
4	80	10	3	yes	6	15.4
3	38	7	2	no	6	7.1

3.1 Requirement for the SVD Ladder

In the SVD, we use the wire-bonding technique to connect strips and the input channel of the APV25 chip. We demand the success rate of the wire-bonds to be larger than 99 percent.

It is also required that the occupancy should be less than 10 percent [7]. To achieve this, the APV25 chip is considered to be suitable due to its various performances. Other requirements of the SVD are described in [7].

3.2 APV25 Readout Chip in Upgraded SVD

To accommodate with the severe backgrounds, the SVD is designed to be read out the data with less trigger dead time. The high occupancy are expected due to large backgrounds and pileup [7].

We use the APV25 chip to read out the SVD hit signals to reduce the influences from the severe background. It has 192 deep pipeline for each channel, 128 channels of readouts line, high tolerance against severe radiation (at least 300 kGy) [7], and fast shaping amplifier (time constant 50 nsec). In the previous experiment Belle, we used a VA1TA readout chip [4] [5]. Replacing the VA1TA by the APV25, the occupancy reduction is possible as shown in Fig. 3.4.

A multi-peak mode of APV25 enables us to measure the hit timing with the resolution of a few nsec. The multi-peak mode takes the consecutive samples; by taking multiple samples as shown in Fig. 3.4, we can find the hit timing. Knowing the hit timing is useful to eliminate the background.

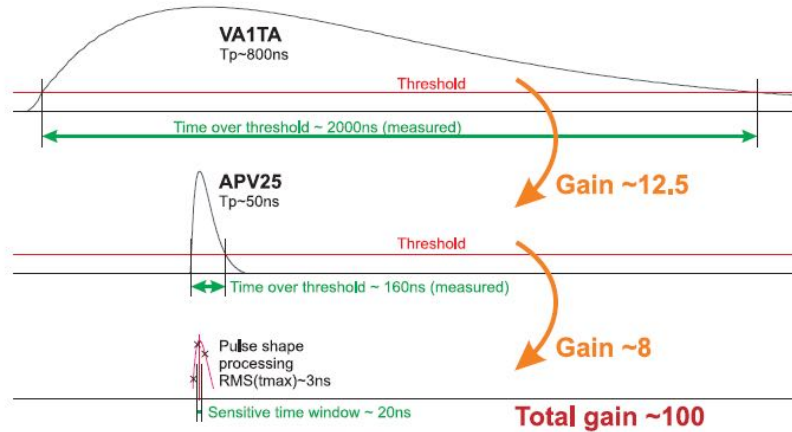


Figure 3.4: Image of hit timing finding [7]. Comparing to the VA1TA, the APV25 allows us to find the hit timing with the resolution of a few nsec.

3.3 Structure of the Layer 6 Ladder

The structure of the SVD “ladder” is shown in Figs. 3.5, 3.6. Each component is described in the next section. There are five sensors (named DSSD, which is described in Chapter. 3.4.) on the ladder. To read out three DSSDs located in the center of the ladder, we use Origami flexible circuit (, which is described in Chapter. 3.4). Also to read out two DSSDs located in the edge of the ladder, we use hybrid board with the APV25 chips mounted. To prevent the heat from the propagation, thermal insulator named AIREX (, which is described in Chapter. 3.4) is inserted between the DSSD and the Origami flexible circuit.

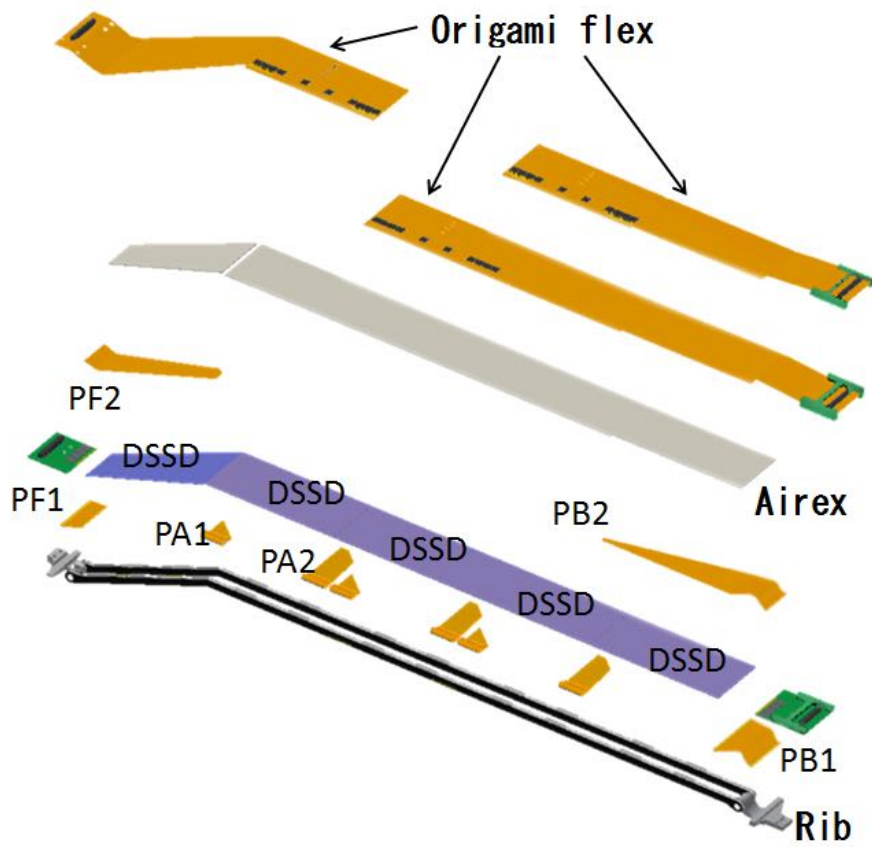


Figure 3.5: Structure of Layer 6 SVD ladder. In Layer 6, five DSSDs and three type of Origami flex are used as this picture. Origami flex is used for reading out three DSSDs located central of the ladder and hybrid board is used for reading out the two DSSDs located on edge of the ladder.

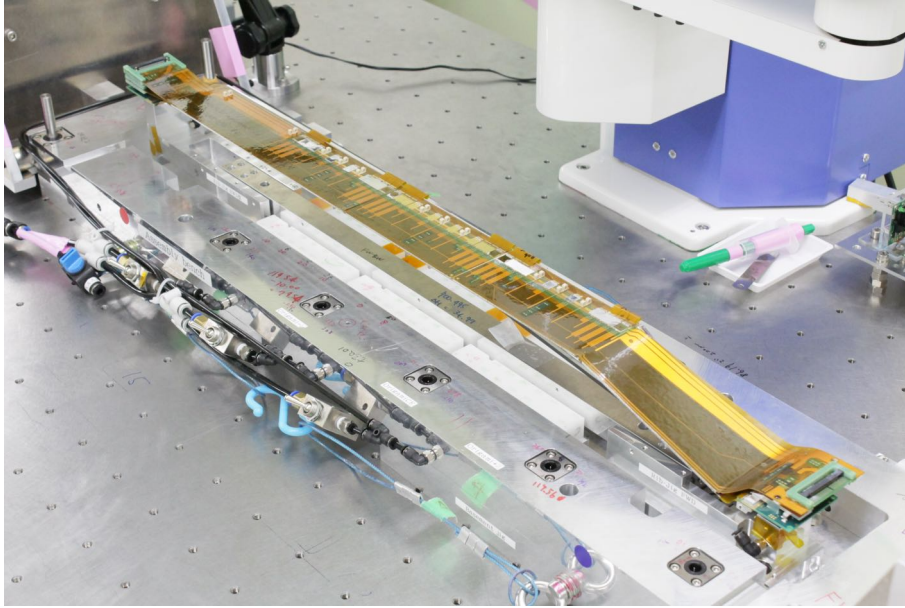


Figure 3.6: Composed Layer 6 SVD ladder.

We define a central Origami part where we use the Origami flexes as the Origami module.

3.4 Components of the SVD Ladder

The SVD components are listed below:

- Double-sided Silicon-Strip Detector (DSSD)
- APV25 read out chip
- ORIGAMI flexible circuit
- Pitch Adapter (PA)
- Forward & Backward Module (FW&BW Module)
- AIREX
- Rib

3.4.1 Double-sided Silicon Strip Detector (DSSD)

The DSSD has a crossed pn semiconductor strip structure. Its structure enables us to measure the hit position 2-dimensionally. To avoid short circuit between the strips in n-side, p^+ -stop is implemented between two n^+ -strips as shown in Fig. 3.7.

The DSSD is used with a bias voltage to make the DSSD full depleted. Mean energy to produce electron-hole pairs is 3.6 eV in silicon. Mechanism of detection is as follows; when a charged particle passes through the DSSD, it produces electron-hole pairs in the depletion region and electrons are collected by strips on the n-side and holes are collected by strips on the p-side. By calculating the center of mass of the collected charge, we can know the particle hit position two dimensionally.

The DSSD is manufactured by Hamamatsu Photonics (HPK) and Micron. There are three types of the DSSD, trapezoidal DSSD (used for Layer 4, 5, 6) shown in Fig. 3.9, large rectangular DSSD (used for Layer 4, 5, 6) shown in Fig. 3.8, and small rectangular DSSD (used for Layer 3). Each DSSD has different strip length and number, of which information are listed in Tables. 3 - 5.

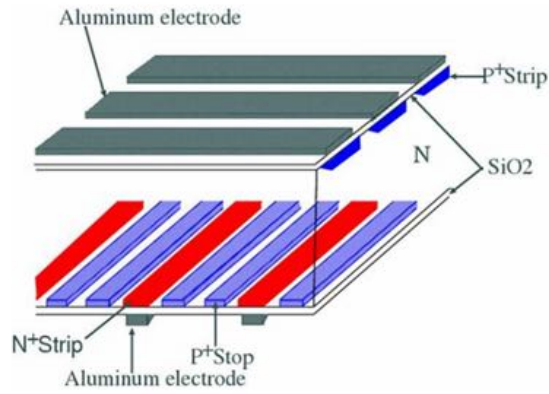


Figure 3.7: Structure of the DSSD [8]. The gap between p^+ and n^+ strip is filled with n-type silicon. To prevent the n-side from short connection, p^+ -strips are implemented between n^+ -strips.

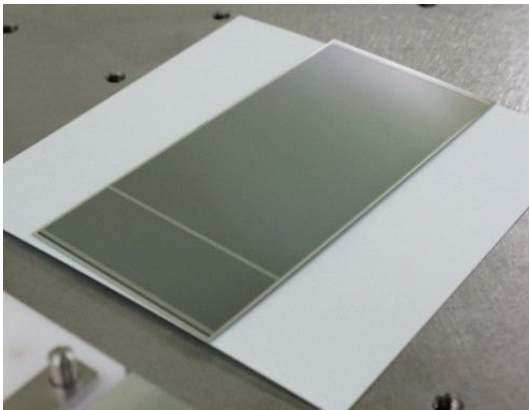


Figure 3.8: Rectangular DSSD



Figure 3.9: Trapezoidal DSSD

Table 3: Feature of rectangular and trapezoidal DSSD [7].

Quantity	RectangularLarge DSSD	RectangularSmall DSSD	Trapezoidal DSSD
Thickness	320 μm	320 μm	300 μm
strips p-side	768	768	768
strips n-side	512	768	512
intermediate strips p-side	767	767	767
intermediate strips n-side	511	767	511
Pitch p-side	75 μm	50 μm	75 ... 50 μm
Pitch n-side	240 μm	160 μm	240 μm
Area (total)	7442.85 mm^2	5048.90 mm^2	6382.6 mm^2
Area (active)	7029.88 mm^2	4737.80 mm^2	5890 mm^2

Table 4: Electrical performance of the rectangular DSSD [7].

Quantity	Value for Rectangular DSSD
Base material	Si n-type 4 $\text{k}\Omega\text{cm}$
Full depletion voltage (FD)	$< 120\text{V}$
Breakdown voltage	$\geq FD + 50\text{V}$
Polysilicon resistor	4 $\text{M}\Omega$ (min), 10 $\text{M}\Omega$ (typ.)
Coupling capacitance	> 100 pF
Breakdown voltage of AC coupling	> 20 V
Bias leak current at FD	1 μA (typ.), 10 μA (max.)

Table 5: Electrical performance of the trapezoidal DSSD [7].

Quantity	Value for Trapezoidal DSSD
Base material	Si n-type 8 $\text{k}\Omega\text{cm}$
Full depletion voltage (FD)	40 V (typ.), 70 V (max.)
Operation voltage	FD ... $2 \times \text{FD}$
Breakdown voltage	$\geq 2.5 \times \text{FD}$
Polysilicon resistor	10 $\text{M}\Omega$ (min), 15 + 5 $\text{M}\Omega$ (max.)
Interstrip resistance, p-side	100 $\text{M}\Omega$ (min.), 1 $\text{G}\Omega$ (typ.)
Interstrip resistance, n-side	10 $\text{M}\Omega$ (min.), 100 $\text{M}\Omega$ (typ.)

3.4.2 APV25 Read Out Chip

The APV25 chip is shown in Fig. 3.10. The APV25 is an analog output readout chip. Its equivalent noise charge (ENC) vary depending on the capacitance of the DSSD as the formulae $ENC(e) = 246 + 36/\text{pF}$ [10]. In addition to the function of APV25 chip, the gain of each channel is calculated by detecting the test pulse generated in the APV25 chip. This function is useful to know the shape of the signal calibration curve for each 128 channel.

Also the APV25 chip has high tolerance to the radiation. It can endure the radiation of up to 300 kGy , which is acceptable in the Belle II experiment for its ten-year operation [7]. The

APV25 chip has multi-peak mode which enables us to know the hit timing and to reject the background in off-line analysis. By using data sample, we can calculate the hit timing, height of signal peak (ADC count). The time resolution of a few nsec is achieved in the SVD [7].

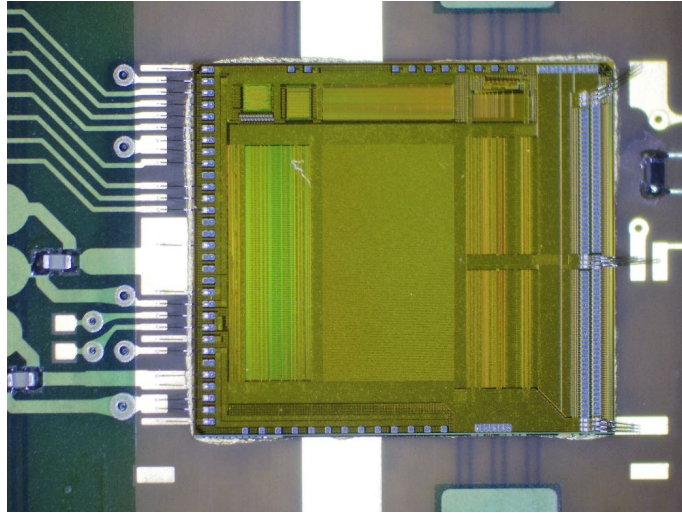


Figure 3.10: The APV25 read out chip

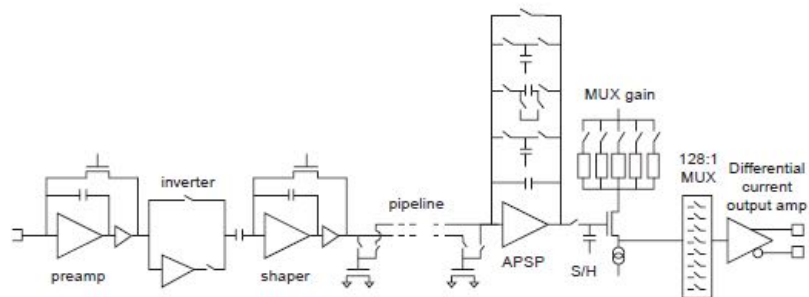


Figure 3.11: Block diagram of APV25 [7] [10].

3.4.3 Origami flexible circuit

There are three types of Origami flexible circuit (Origami flex) as shown in Fig. 3.12. The Origami flex is introduced to minimize the length of connection between the DSSD and the APV25 chip as described in the Chapter 3.7. As shown in Fig. 3.12, totally ten APV25 chips are put on each type of Origami flex.

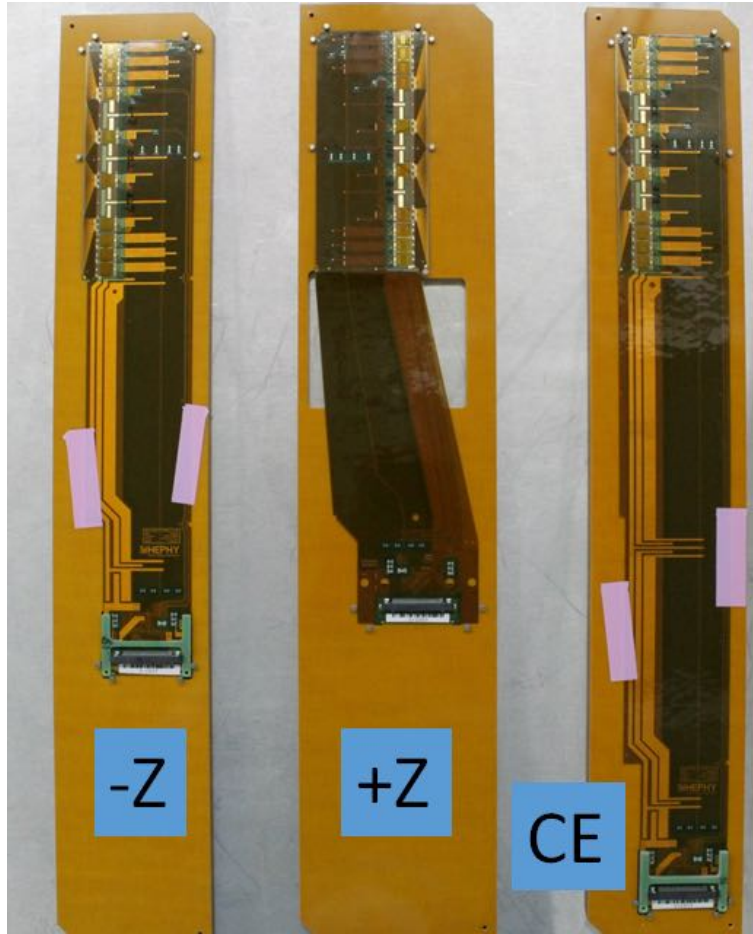


Figure 3.12: The Origami flexible circuit with the APV25. Left, center, and right Origami flexes are -Z, +Z, and CE respectively.

3.4.4 Pitch Adapter

A Pitch adapter (PA) is another flexible circuit, which is shown in Figs. 3.13 and 3.14. There are totally six PAs, which is used to connect the APV25s and the DSSD.

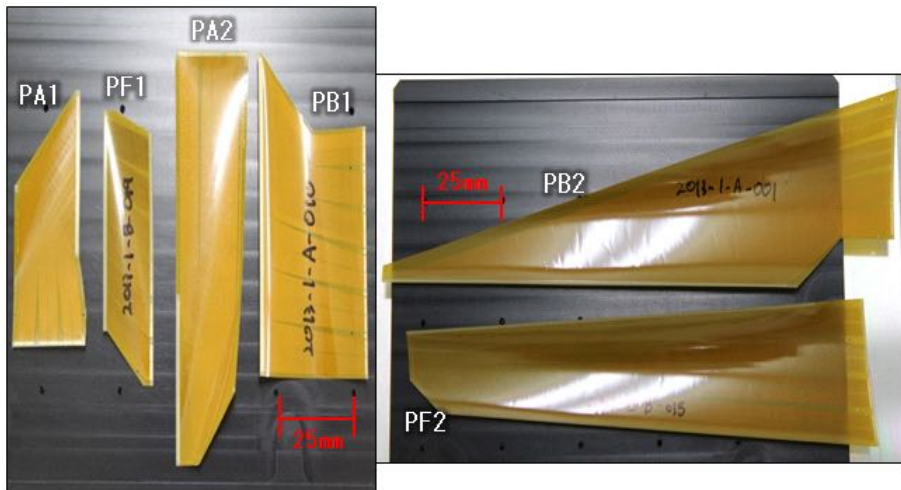


Figure 3.13: The Pitch Adapter (PA)

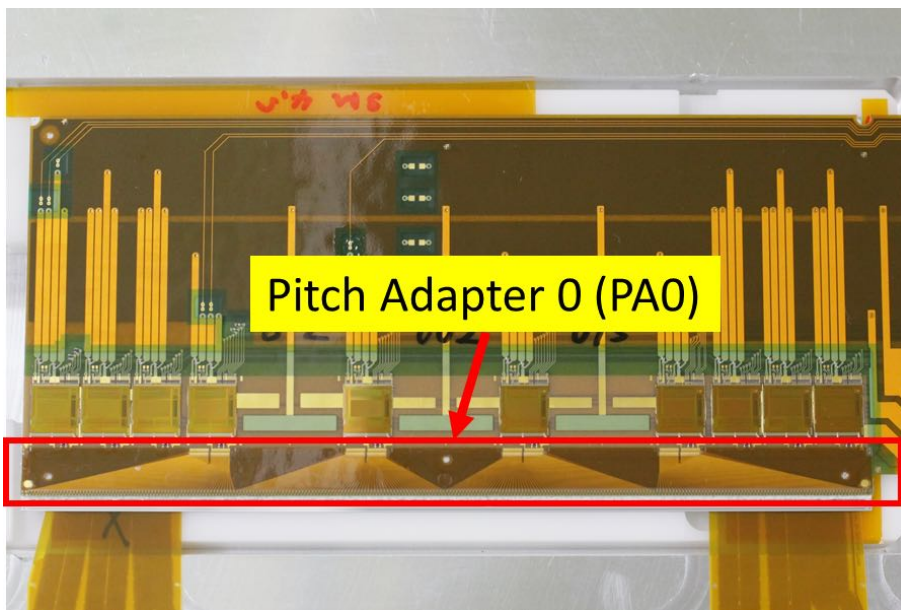


Figure 3.14: The PA0 implemented on the Origami flex.

3.4.5 Forward and Backward Module (FW and BW Module)

Forward and backward modules are located at the both edges of ladder. Picture of modules is shown in Fig. 3.15.

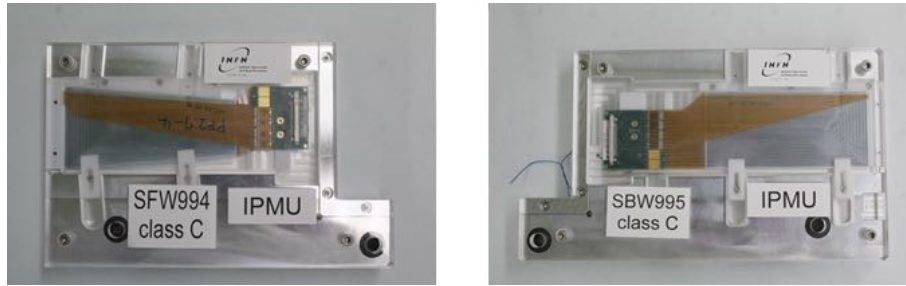


Figure 3.15: The FW and BW module. Left is the FW module and right is the BW module.

3.4.6 AIREX

An AIREX [9] is a heat insulator inserted between the DSSD and the Origami flex as shown in Fig. 3.5. Because of the heat from the APV25 chips (350 mW per one APV25 chip), there is the possibility that the DSSD becomes hot and that strips become noisy. Also to separate the Origami flex electrically from the DSSD, the AIREX is used.

3.4.7 Rib

The rib supports all components: the DSSD, AIREX, Origami flex, Forward and Backward module, and the AIREX. Support structure is composed of two ribs and two mount blocks at each end.

3.5 APVDAQ for EQA

The APVDAQ [11] was developed by High Energy PHYSics (HEPHY) in Austria. In this section, we first see the whole readout chain of the APVDAQ. After this, we see the components to use the APVDAQ. In the last of this section, we see the functions of APVDAQ, which are used for the EQA procedures.

3.5.1 Read out chain

Fig. 3.16, 3.17 shows the signal line of APVDAQ.

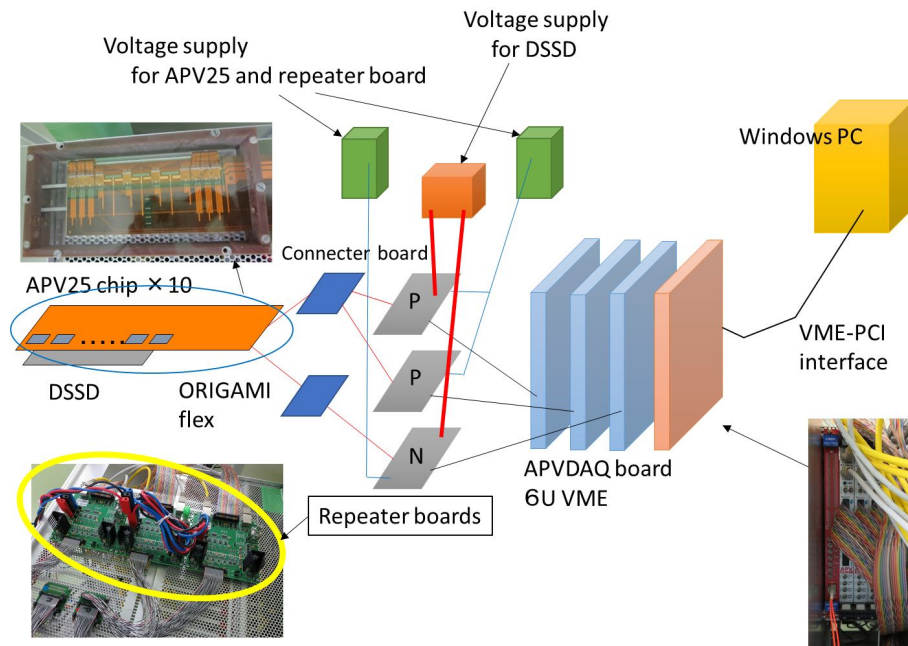


Figure 3.16: Image of the cabling of APVDAQ.

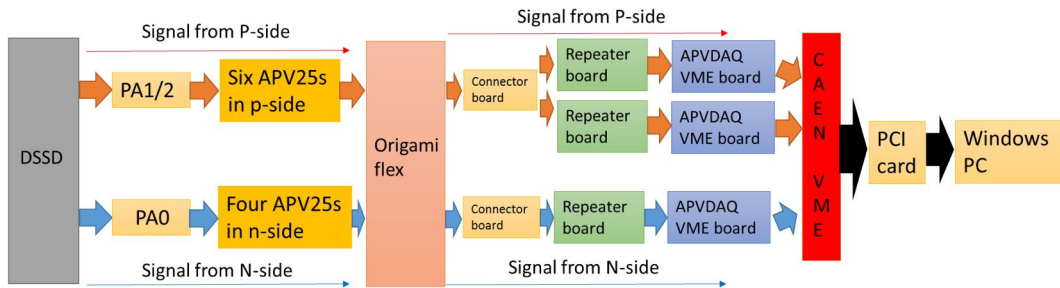


Figure 3.17: Readout chain of the signal.

Fig. 3.18 shows how each component is connected in the Origami flex. DSSD - PA and PA - APV25 are connected by the wire-bonding.

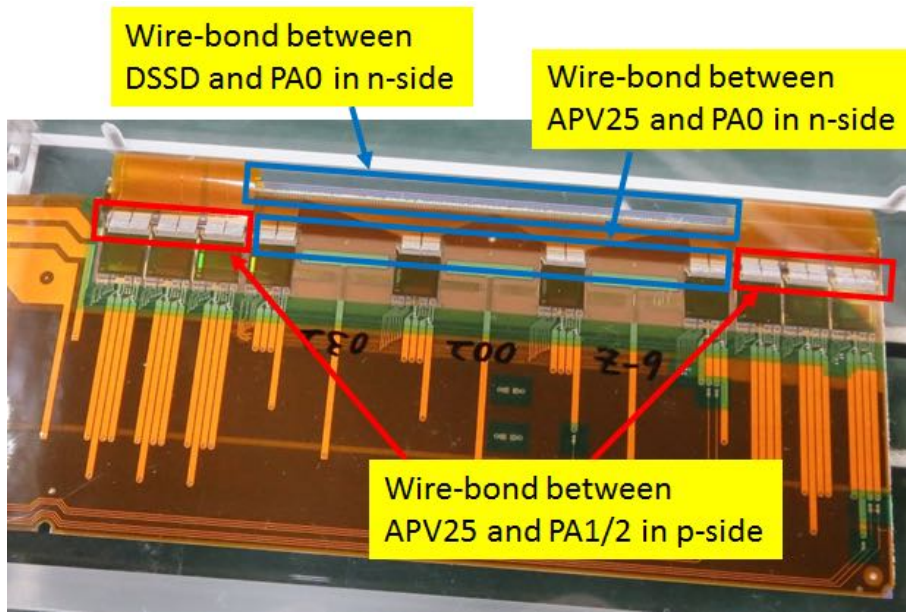


Figure 3.18: Places of the wire-bonds on the Origami flex.

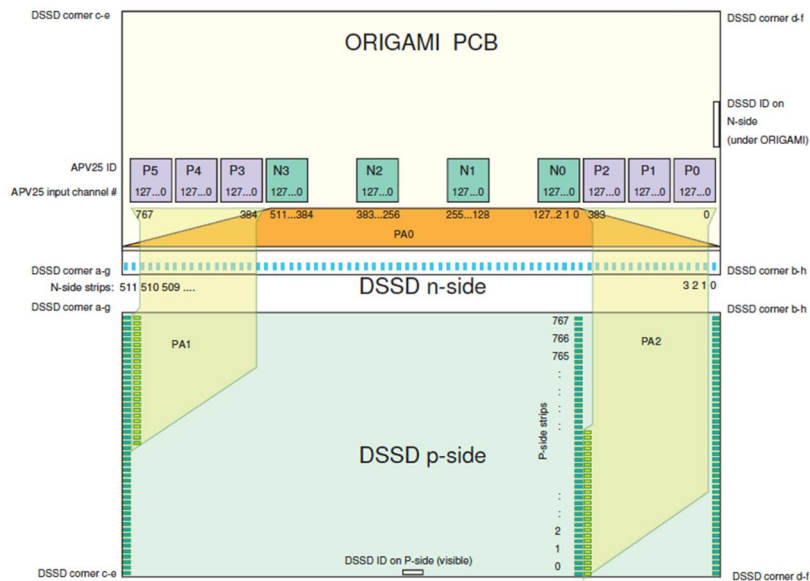


Figure 3.19: Ordering of strip numbers and the APV25's numbers. P-side is bottom side of the DSSD and n-side is top side of the DSSD.

We define the numbering of each APV25 as shown in Fig. 3.19; the APV25 in n-side is defined as N_i , ($i = 0 \sim 3$) and the APV25 in p-side is defined as P_i , ($i = 0 \sim 5$).

The APVDAQ allows us to read the signals from ten APV25 chips. The APVDAQ performs analog to digital converter (ADC) and has a 10-bit format of data thus output ADC count is

from 0 to 1023. The ADC count is used to measure each parameter for EQA such as the noise. These parameters are discussed in this section.

In the next section, we see the components of APVDAQ.

3.5.2 Components of APVDAQ

We use following components to read out hit signals from the SVD.

- Three APVDAQ VME boards (Fig. 3.20)
The APVDAQ board digitizes of the signal sent from APV25. One board can read up to four APV25 chips. We can input a trigger from the front panel of the board.
- Three repeater boards (Fig. 3.21) and connector boards
This board is used to provide the voltage to APV25 chips, and we can impose a high voltage (HV) to the DSSD through this board. Also this board is used to send the signal to the APVDAQ boards. The connector boards are used to divide the signals sent from the APV25 chips to the APVDAQ VMEs. To read out the signal from p-side, we use two APVDAQ boards. For sending the signals to two APVDAQ boards, we use this connector board to branch the signals in p-side to two repeater boards.
- Bias voltage supply for the DSSD
We supply ± 40 V for a large DSSD and ± 50 V for a trapezoidal DSSD.
- Voltage supply (± 5 V and ground) for the APV25 and the repeater boards.
We supply the voltage to the APV25 chips and the repeater boards.
- CAEN 2718 VME interface (Fig. 3.22)
To receive the signals from the APVDAQ boards, the CAEN boards is used. The CAEN board communicates with the PCI card for sending the signals from the APVDAQ boards.
- PCI card to communicate with the CAEN VME interface
The PCI card inserted to the PC receives the data from the CAEN VME.
- APVDAQ software
To read out the signals digitalized by the APVDAQ VME, we use the APVDAQ software. This software has functions that we can check the signal of all channels in the APV25 chips. Detail explanation is written in the next section.
- Windows PC
We use Windows PC to use the APVDAQ software.



Figure 3.20: The APVDAQ VME board. We use totally three APVDAQ boards; two boards are used to read out p-side, and one board is used to read out n-side signals.

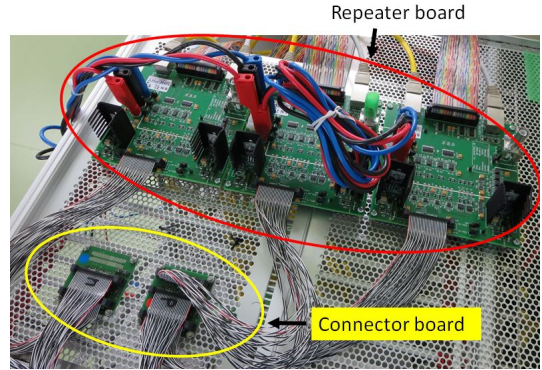


Figure 3.21: Three repeater boards and two connector boards. Two repeater boards are for p-side, and one repeater board is for n-side signals. One connector board has signal cables branched to two cables for sending the signals from p-side to two repeater boards. Another connector board does not have the branch, is used to send the signals from n-side to one repeater board.

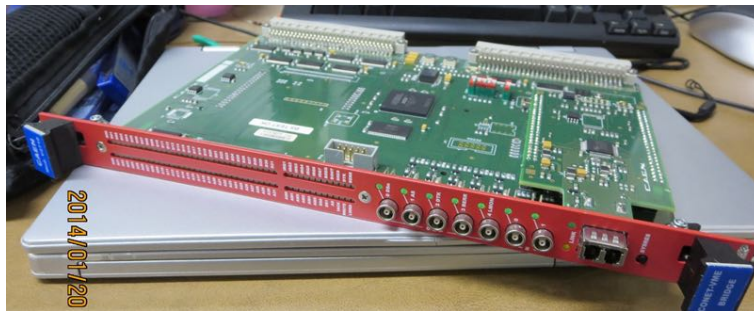


Figure 3.22: CAEN VME interface

3.5.3 Function of APVDAQ Software

Run modes of APVDAQ explained in next page are used in our EQA procedure. The APVDAQ software allows us to read out the ADC count of the ten APV25 chips. Also it can save the data as the binary format. To read out the signals of ten APV25 chips, we can use following

function depending on the situation.

- **Hardware Run**
We use this run mode to take data by using an external trigger.
- **Software Run**
We use this run mode to take data by using a random trigger generated by the APVDAQ. The data taken by this run mode is not associated with the signal; we therefore can evaluate the noise of each channel by evaluating the root mean square of ADC count. We can set the number of events to take.
- **Internal Calibration Scan**
We use this run mode to obtain the calibration curves for each channel by using the test pulse generated by the APV25 chip. The calibration curve is the signal shape of each channel made by test input of the APV25 chip. This run mode measures the signal calibration curve for all channels. The APV25 chip has the function of test pulse and it can send 1 MIP charge (in our case, 22400 electrons) to each channel. Also by using the delay trigger, the APVDAQ can measure the ADC count in each time. Then by connecting each point, we can obtain the calibration curves as shown in Fig. 3.23.

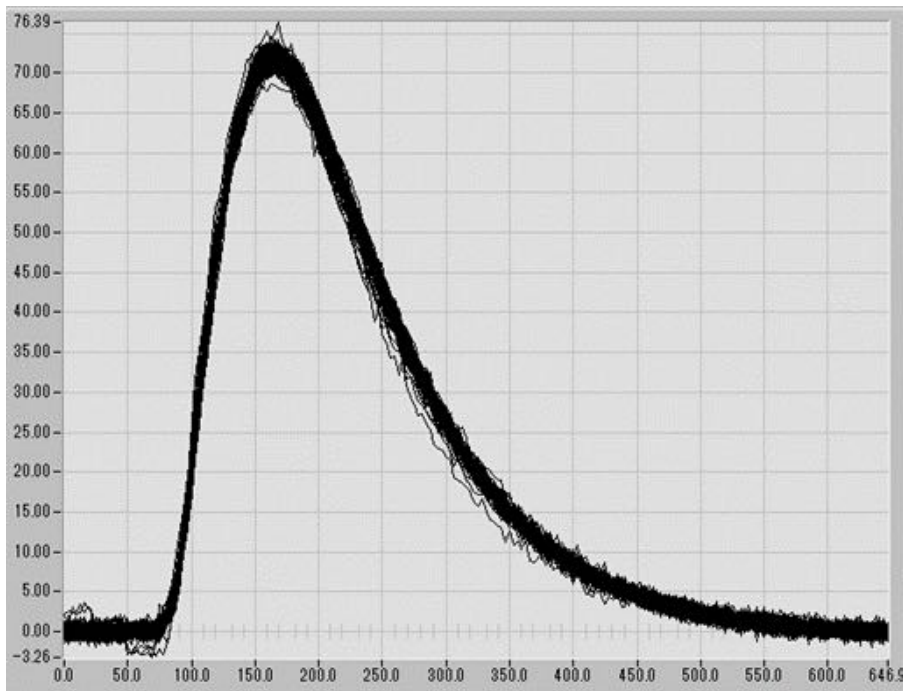


Figure 3.23: Calibration curve displayed by the APVDAQ. Horizontal axis indicates time (nsec) and Vertical axis indicates ADC count. There are 128 curves superimposed.

In order to obtain the calibration curve, the ADC count is sampled every 3.125ns.

In these run mode, the APVDAQ takes 600 events to calculate the pedestal, and the noise of the channel.

3.5.4 Calibration constant

We can calculate the calibration constant (number of electron/ADC count) by “Internal Calibration Scan”. In our setting, 22400 electron is used as a 1 MIP charge of the test pulse and by using its total charge and the pulse height of the calibration curve, calibration constant (e/ADC) is calculated for each channel; thus, the calibration constant is explained by the following formula

$$\frac{e}{ADC} = \frac{1 \text{ MIP charge}}{\text{Pulse height of calibration curve}} \quad (3.1)$$

This calibration constant is used for the analysis in Chapter 8. Calculation of pulse height is done by the APVDAQ and the result of calculated pulse height is recorded in the text file.

3.6 Parameter for EQA

In this section, we see how many parameters are used and how each parameter is calculated. Following parameters will be used for the EQA.

- Raw ADC count
ADC count which has no any correction sampled by the APVDAQ.
- Common mode shift (CMS)
A global shift of ADC count in one APV in each sampled event.
- Common mode corrected ADC count (CMC ADC count)
ADC count whose CMS is subtracted.
- Noise (Pedestal noise)
RMS of the CMC ADC count, same definition as in the previous section.
- Raw noise
RMS of the raw ADC count (without CMC)
- CalAmp (pulse height)
pulse height of the calibration curve, same definition as in the previous section.

Mainly we use the ADC count for evaluating the signal, the noise, and the pedestal. Following formulae are used to calculate the parameters. Index i is the number of APV, j is the number of channel, and n is the event number.

$$PED[i][j] = \frac{1}{300} \sum_{n=0}^{299} Raw\ ADC[n][i][j] \quad (3.2)$$

$$Raw\ noise[i][j] = \sqrt{\frac{1}{300} \sum_{n=300}^{599} (Raw\ ADC[n][i][j] - PED[i][j])^2} \quad (3.3)$$

$$CMS[n][i] = \frac{1}{128} \sum_{j=0}^{127} (Raw\ ADC[n][i][j] - PED[i][j]) \quad (3.4)$$

$$Signal[n][i][j] = Raw\ ADC[n][i][j] - PED[i][j] - CMS[n][i] \quad (3.5)$$

$$Noise[i][j] = \sqrt{\frac{1}{300} \sum_{n=300}^{599} (Signal[n][i][j])^2} \quad (3.6)$$

We use $Signal[n][i][j]$ as CMC ADC count. The number 0 - 599 means the first 600 events taken by the APVDAQ with random trigger.

3.7 Chip on sensor concept

The signal line length between the APV25 and the DSSD is minimized since long signal line introduces more noise. In our SVD, the structure shown in Fig. 3.24 is used for minimizing the noise. To transmit the backside (p-side) signals to the APV25 chips mounted on the front side, we use flexible circuits as shown in the picture.

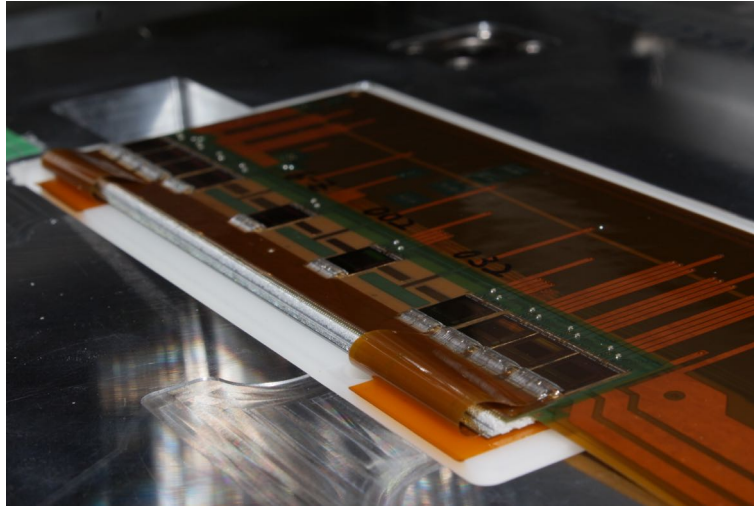


Figure 3.24: The structure of the chip on sensor concept.

4.1 The Role of EQA in the Assembly Procedure of the Ladder

Before when we saw each assembly procedure, we explain how EQA procedure is performed. As showing in Fig. 4.1, we perform the EQA in every wire-bonding procedure so that we can detect the electrical problems; for example, unconnected wire-bond, short-connected wire-bond, and noisy strips in the DSSD. To perform the EQA during the wire-bonding, we use movable APVDAQ, which is shown in Fig. 4.2.

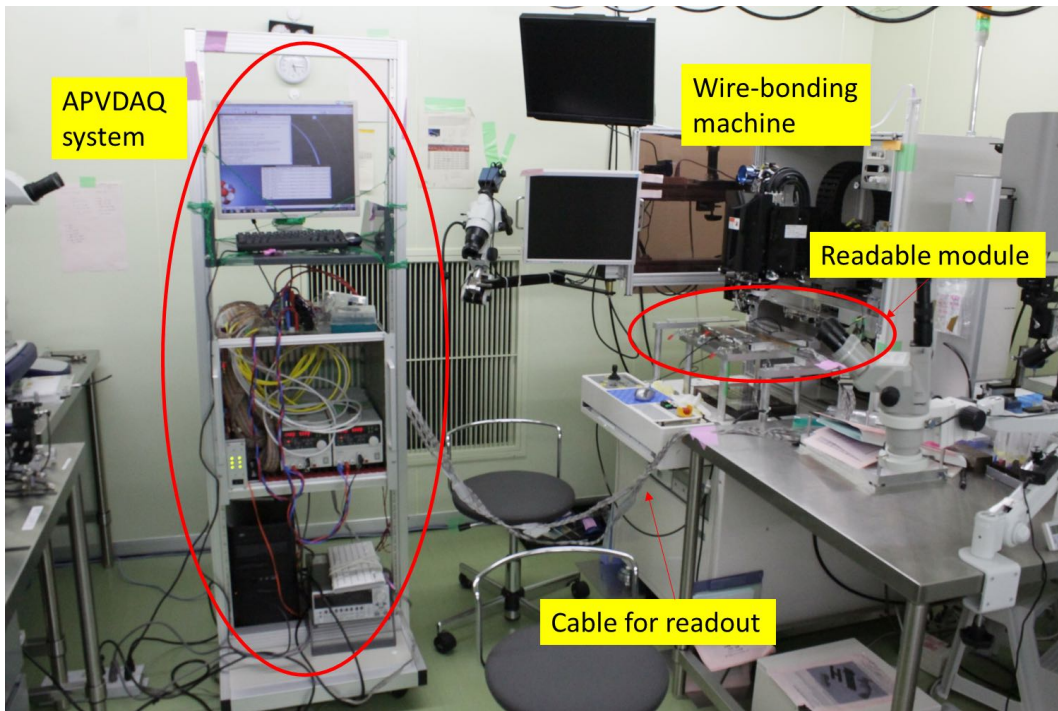


Figure 4.2: EQA during the assembly by the APVDAQ. In order to perform the EQA during the assembly, we insert the cable to the readable module (part of ladder), which is put on the wire-bonding machine.

By using this movable setup, we can perform the EQA in every assembly procedure, and also in everywhere.

4.2 Gluing PA1 and PA2 on a the DSSD, and wire-bonding

First, we glue the PA1/2 on the the DSSD. After gluing, we wait at least 24 hours until the glue has been cured. Then, we make wire-bonding between the PA1/2 and the DSSD. In this step we do not check the condition of a wire-bonding electrically because there is no connection between the APV25 and the DSSD. We make eye-inspection every 30 bonds by microscope. If a broken connection is found, we repair it.

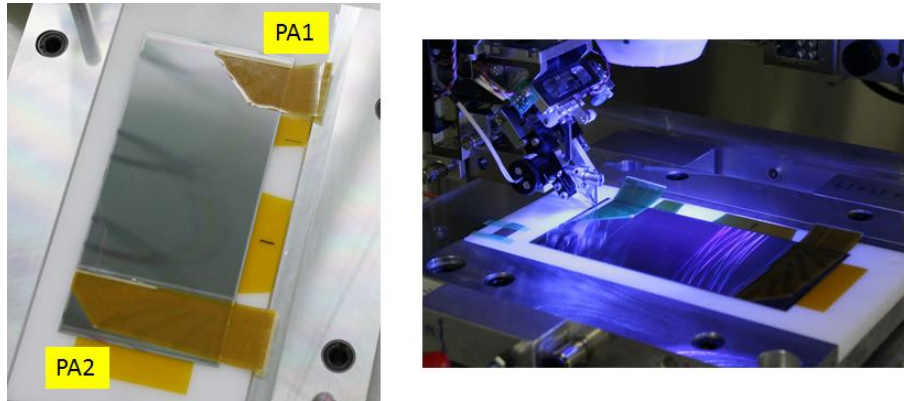
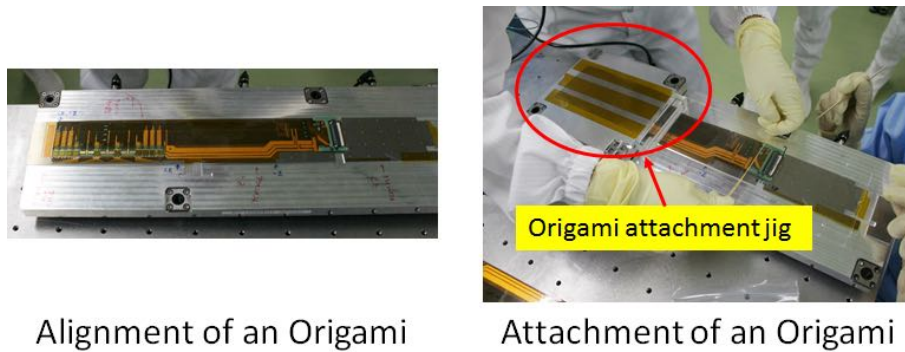


Figure 4.3: Glued PA1 and PA2 on the the DSSD (left) and wire-bonding between them (right).

4.3 Alignment of Origami flexes, AIREXes, and the DSSDs and Gluing

Next, we align an the Origami flex as shown in Fig. 4.4. After this alignment, we put glue on the AIREX to attach it on the DSSD. Then, we put glue on the Origami flex (Fig. 4.5) and attach on the Airex as Fig. 4.6.



Alignment of an Origami

Attachment of an Origami

Figure 4.4: Alignment and attachment of Origami flex. Left picture shows the alignment of Origami to adjust the position of Origami. Right picture shows the attachment of Origami to a carrier jig.



Figure 4.5: Putting glue on the Origami flex

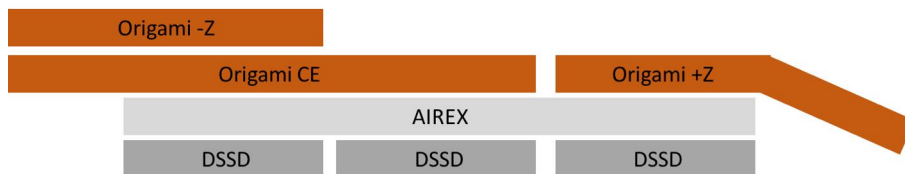
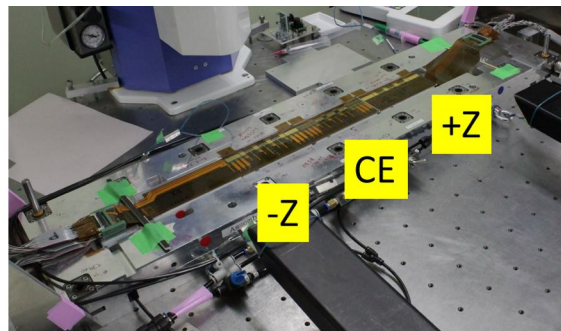


Figure 4.6: Glued three Origami flexes, AIREXes, and the DSSDs. Three DSSDs and AIREXes are under the Origami flexes.

4.4 Wire-bonding in N-side

From this step, EQA inspections start for checking the condition of the wire-bonding. Until this step, there is no wire-bond between the APV25 and the DSSD. In this step, we do wire-bonding as the procedure shown in Fig. 4.1 so that we can find out a defect of the wire-bond and repair it. First, inner loops are wire-bonded and tested electrically so that we can repair bad connections easily. If we detect a failure wire-bond in the inner-loops, it is difficult to be repaired because wire-bonds in outer-loops interfere in accessing to the inner-loops as shown in Fig. 4.8. After the confirmation of no broken connection, we make outer-loop wire-bonds. Figure. 4.9 shows the wire-bonds between the APV25 and the PA0, and Fig. 4.10 shows the wire-bonds between the PA0 and the DSSD.

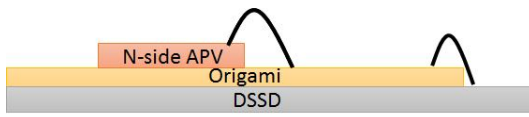


Figure 4.7: Wire-bonding on the N-side inner-loop. Black curve in this picture is the wire-bond.

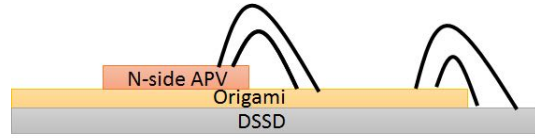


Figure 4.8: Wire-bonding on the N-side outer-loop. Black curve in this picture is the wire-bond. These outer-loop prevents the inner-loop bonds from repairing.

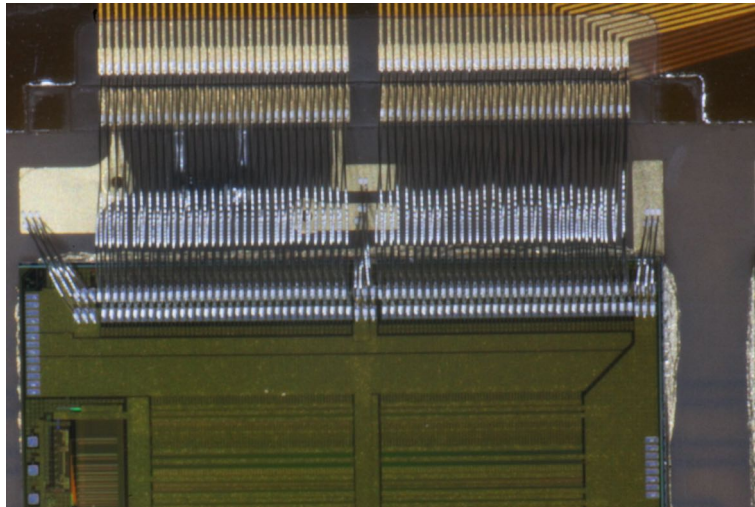


Figure 4.9: Wire-bonding on the n-side between the APV25 chip and the PA0. Lower pads are APV25's, and upper pads are PA0's.

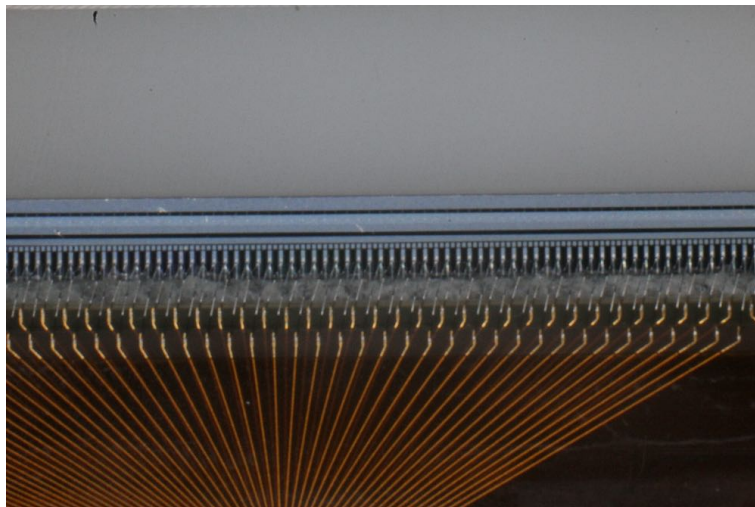


Figure 4.10: Wire-bonding on the n-side between the PA0 and the DSSD. Upper pads are DSSD's, and lower pads are PA0's.

4.5 Wrapping Procedure

As shown in Fig. 4.11, we wrap the PA1/2 on the DSSD backside to the Origami flex over the wire-bonds on the n-side. In order not to break the wire-bonds below the wrapped PAs, we developed a special wrapping jig to control the PA motion.

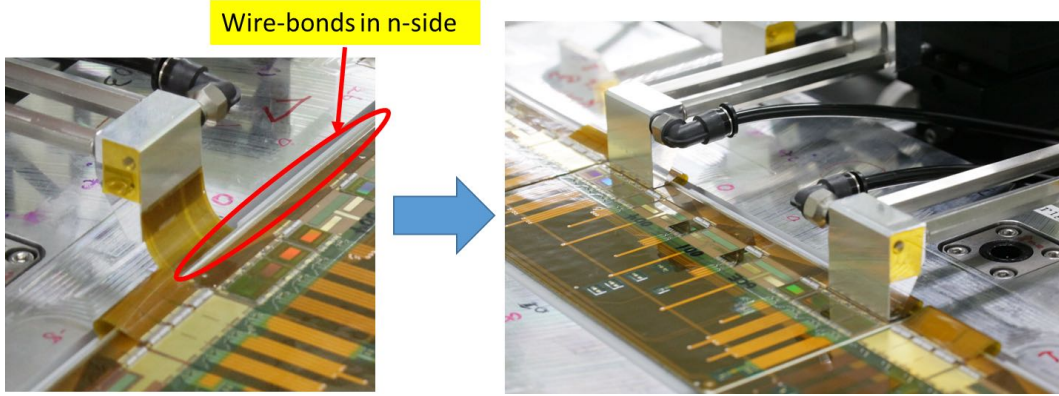


Figure 4.11: Wrapping procedure. Under the PA1/PA2, there are the wire-bonds in n-side. If the PA1/PA2 hits the wire on n-side when we curl the PA1/PA2 and attach it on the surface of the Origami flex, fragile wire is broken.

4.6 Wire-bonding in P-side

Wire-bonding in P-side is done as following steps. Image of these procedures are shown in Fig 4.12-4.14.

- 1. Wire-bonding of inner-loops (Fig. 4.12)
Even number strips are wire-bonded, where the numbering of the DSSD strips are defined in Fig. 3.19.
- 2. Wire-bonding of middle-loops (Fig. 4.13)
Strips of 1, 5, 9, 13, ... , 121, 125, 129, ... are wire-bonded, where the numbering of the DSSD strips are defined in Fig. 3.19.
- 3. Wire-bonding for outer-loops (Fig. 4.14)
Remaining strips 3, 7, 11, 15, ... , 123, 127, 131, ... are wire-bonded, where the numbering of the DSSD strips are defined in Fig. 3.19.

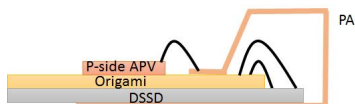


Figure 4.12: Wire-bonding in P-side inner-loops

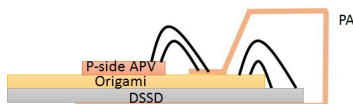


Figure 4.13: Wire-bonding in P-side middle-loops

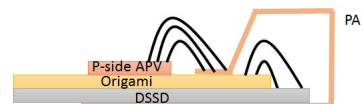


Figure 4.14: Wire-bonding in P-side outer-loops

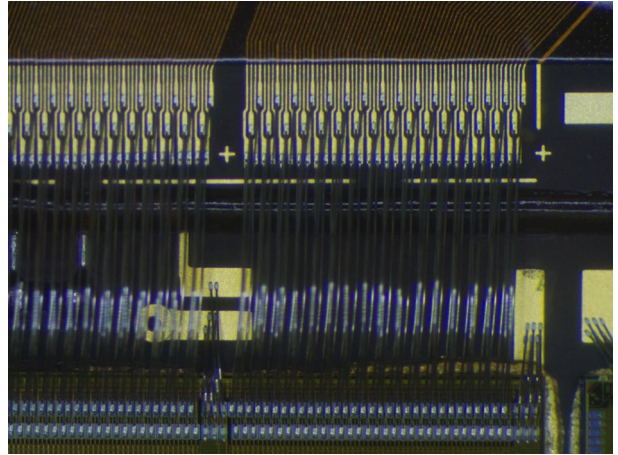
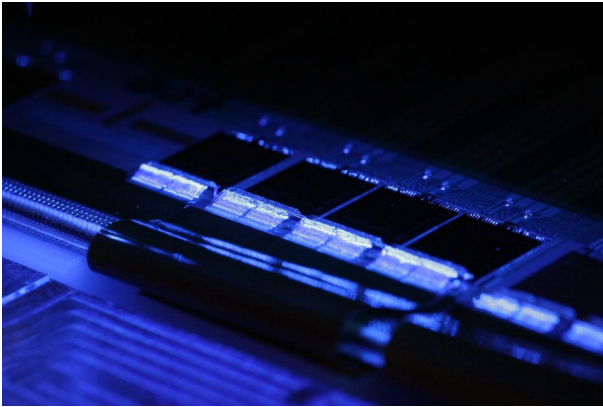


Figure 4.15: Left picture shows wire-bonds on p-side (part of curled PA). Right picture shows wire-bonds in P-side; upper pads are of PA1/2, lower pads are of APV25.

4.7 Attachment of Origami Modules to Ribs

As the final step, we glue the Origami modules and the FW and BW module on the ribs as shown in Fig. 4.16. For the attachment of the Origami modules, we let them down on the ribs where the FW and BW modules are attached on it.

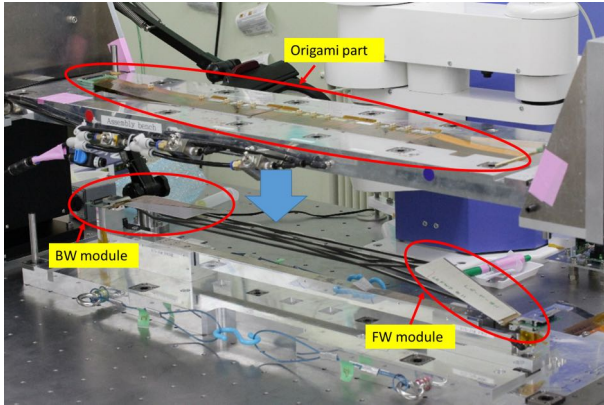


Figure 4.16: Left shows when we attach the Origami parts on the ribs, and right shows after the attachment of the Origami parts.

5 Procedure and Method of Study for EQA

Purpose of EQA is to assemble electrically working ladder. To achieve this purpose, three methods are implemented in the whole the assembly procedures.

First, to exclude broken components in the ladder assembly, we perform parts level EQA. In this procedure, we check an electrical functionality of the Origami flexes with the APV25 chips. The Origami flexes are delivered from the company after the APV25 chips are glued. Since the company does not check the quality of APV25 chips after gluing, it is needed to check the quality of APV25 chips electrically by us. We read out the APV25 chips through the signal line in the Origami flex by the APVDAQ. In this procedure, we detect malfunctioning APV25 chips and exclude the Origami flex from the assembly.

Second, to determine whether we can proceed to the next assembly step or not, we perform the assembly level EQA. In this procedure, we concentrate whether we can detect the bad channels: such as unconnected channel, short-connected channel, and noisy strip in the DSSD. After each wire-bonding procedure, we check the connection electrically by the APVDAQ. In our measurement, we mainly check each channel's pulse height, raw noise, and noise. Since the number of wire-bonds is quite large (there are 12800 wire-bonds which we perform per ladder), an effective way for the quality inspection is needed.

Finally, to check whether the assembled ladder is acceptable for the experiment, we perform whole ladder level EQA. In this procedure, quality inspection by β -ray source test is carried out. We mainly check cluster charge and signal to noise ratio of each channels to confirm whether assembled module is functioning or not. Detail explanation of the whole assembly EQA is given in Chapter 8.

In order to understand the behavior of the channels during the assembly procedure and the β -ray test, we studied the response of the strips. The studies and results are given in Chapter 8 and Appendix C. For this purpose, we assembled two readable modules as the pre-experiment shown in below.

5.1 Single-DSSD Readable Module for the Study of EQA

We first assembled the Single-DSSD readable module, which is shown in Fig. 5.1. This is a part of the ladder. We used following components for this module. The purpose of this module is to study the behavior of the bad channels, whose detail is described in Appendix A.

- Readable DSSD
Electrically working DSSD. This DSSD has only two pin-hole strips in p-side. Other strips are readable.
- Class-C Origami -Z flex with the APV25 chips
This Origami has one malfunctioning APV25 in p-side. This Origami is classified before the assembly not to use in a real ladder assembly. The way how to classify the Origami flex is described in Chapter 6.
- AIREX
As mentioned in Chapter 3.4.6.
- Rib
As mentioned in Chapter 3.4.7.

As described in Appendix A, we succeeded to detect the problem of the broken line in PA0 by the EQA. Also we succeeded to know the behavior of short-connected channel and unconnected channel.

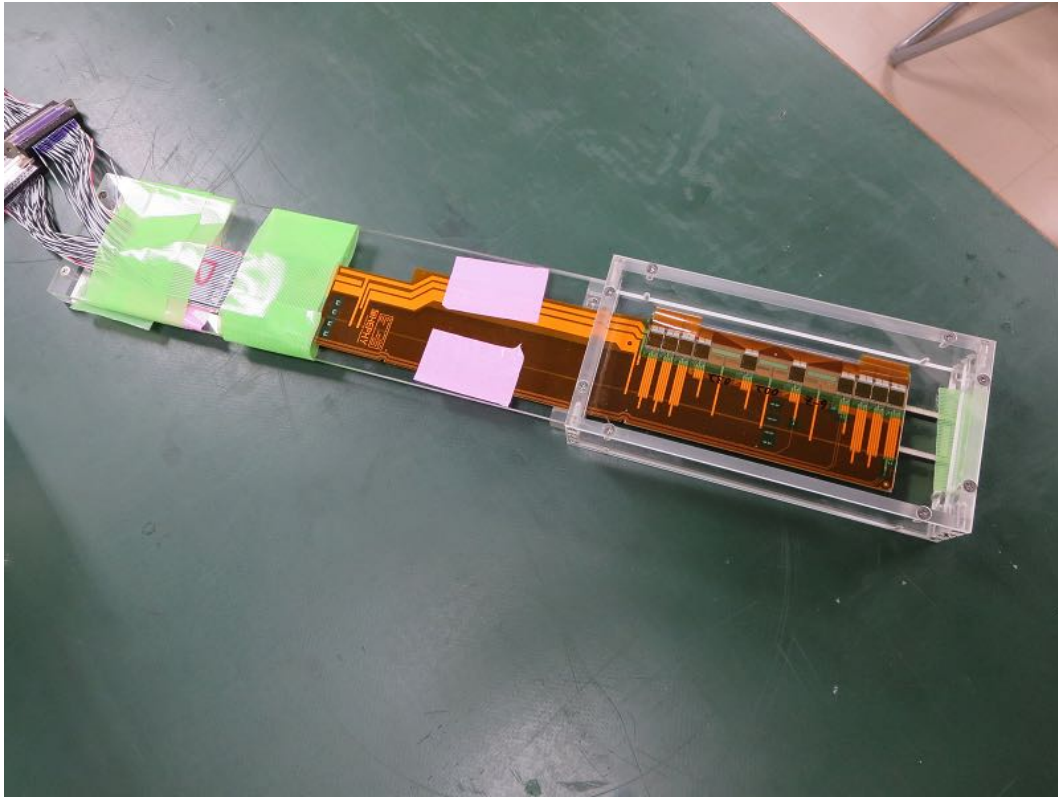


Figure 5.1: Single-DSSD readable module.

5.2 Class-D Ladder Assembly for the Study of EQA

After the assembly of Single-DSSD readable module we assembled class-D ladder as shown in Fig. 5.2.

- One Readable DSSD
Electrically working DSSD. This DSSD has only three broken strips in n-side.
- Four Unreadable Dummy DSSDs
Cannot be used as the readable DSSD.
- Class-C Origami CE flex with APV25 chips
This Origami has one broken APV25 in p-side.
- Mock-up (Class-D) Origami +/-Z flex
This Origami has no APV25.
- AIREX
As mentioned in Chapter 3.4.6.
- Rib
As mentioned in Chapter 3.4.7.

The purpose of this class-D ladder assembly is to confirm whether the established assembly procedure is working or not, but also to confirm the EQA procedure whether it is working or not.

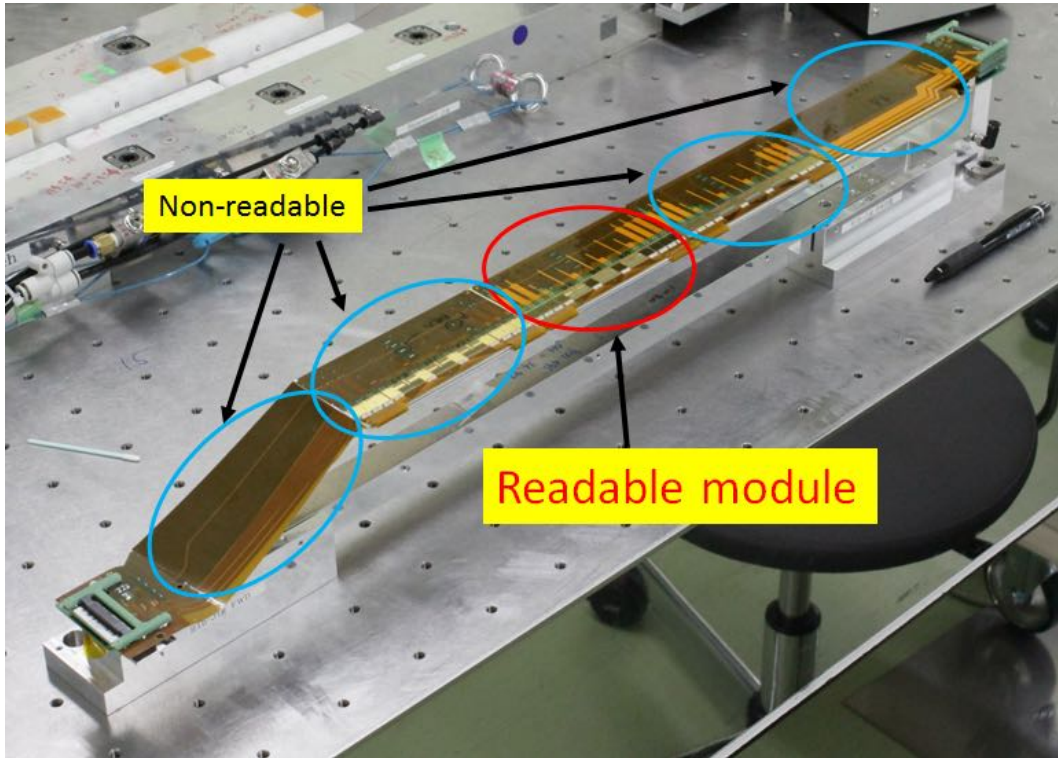


Figure 5.2: Assembled class-D ladder. Only Origami CE part is readable as shown in picture. Other parts are composed without APV25 and thus not readable.

Through the assembly of the class-D ladder, we verified constructed EQA procedures: assembly level EQA and whole assembly level EQA. The detail explanation of assembly level EQA procedures is described in Chapter. 7, and whole assembly level EQA is described in Chapter. 8.

6 Parts Level EQA

Parts level EQA is important to exclude the electrically broken components before the assembly. Each component's quality is confirmed as below.

- The quality of DSSD is assured by HPK and Micron. One DSSD has 1280 strips in total. Company gives us the DSSD whose yield of bad channels in the DSSD to be less than 5%. This 5% is acceptable for our SVD.
- The quality of Origami flex and APV25 module is assured by our measurement by the APVDAQ. As mentioned in Chapter. 3.4, there are three types of Origami flex, Origami -Z, Origami CE, and Origami +Z.
- The quality of PA is assured by its manufacturing company.

In our EQA procedure, we mainly check the quality of Origami flex and APV25 (Fig. 6.1).

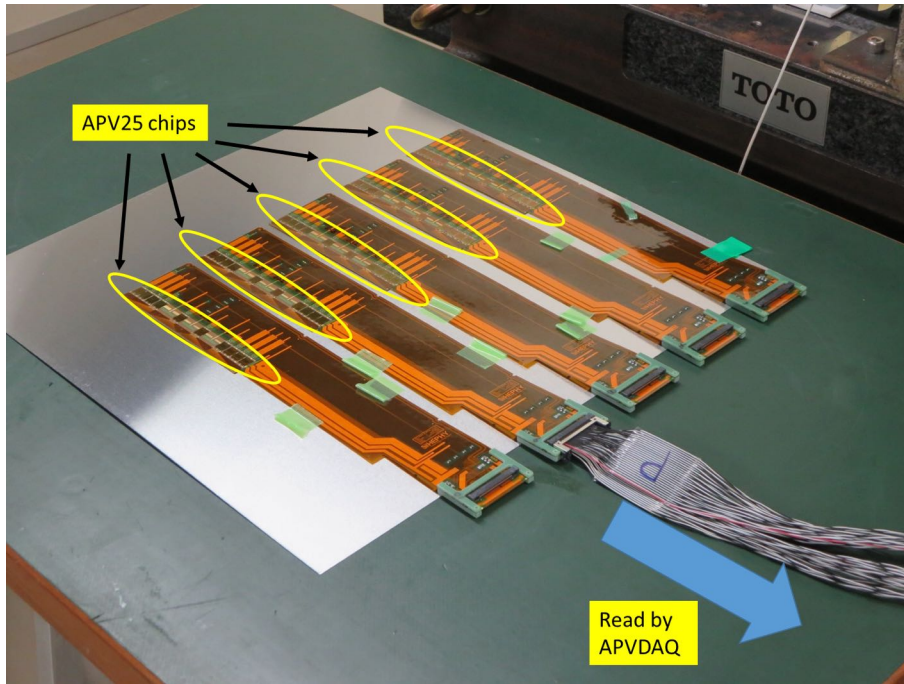


Figure 6.1: Parts level EQA for the Origami flex and the APV25s.

6.1 Assumption to Determine the Quality of the Origami flex and APV25

We read the APV25 chips on the Origami flex through the control line in the Origami flex by the APVDAQ to check the connection of the Origami. We built following hypothesis to confirm the electrical quality of the Origami flex and the APV25 chips.

- If we read the APV25 chips on the Origami flex successfully, we assume all control lines in the Origami flex have no problem. Also if all APV25 chips on Origami flex are read without problem, the APV25 chips have no problem.

The meaning of “read” is explained in the next section.

6.2 Method of Experiment

When we read out the APV25, the APVDAQ sends the signal to APV25s to initialize the I²C interface. Some malfunctioning APV25s fail to do this I²C initialization. In this section, if we succeed this initialization, we express APV25 is “read” successfully. In general, the APV25 with I²C error cannot output any signals; in such a case, the APVDAQ shows error message.

After confirming the APV25 is initialized, we proceed to the next step to check the quality of APV25. To quantify the quality of Origami flex and APV25, we used two parameters, the pulse height and the noise. The definition of pulse height and noise as follows.

- Pulse height
As mentioned in Chapter 3.5, the calibration curve for each channel is available by the APVDAQ. We define pulse height as the height of calibration curve. See Fig. 6.2.
- Noise
The noise is defined as the root mean square (RMS) of common mode corrected (CMC) ADC count. See Fig. 6.2.
- Signal to noise ratio (SNR)
SNR is defined as pulse height / noise.

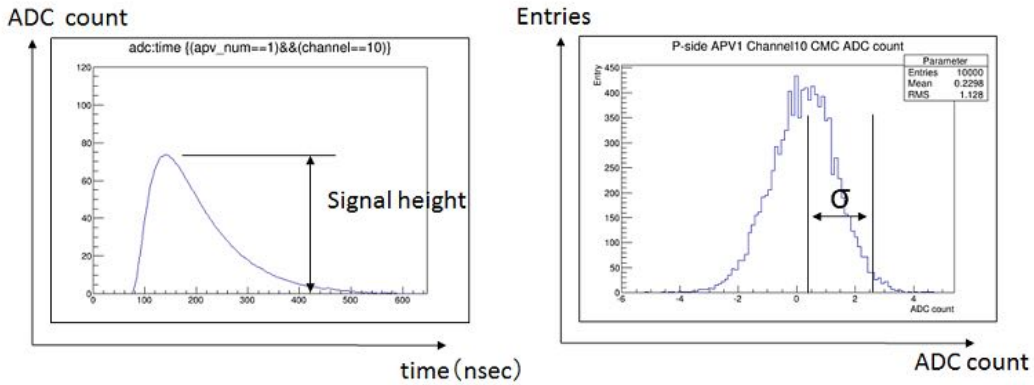


Figure 6.2: Definition of pulse height and noise. Pulse height is defined as the height of calibration curve and noise is defined as the RMS of CMC ADC. The figures are obtained when APV25 is not connected to the DSSD.

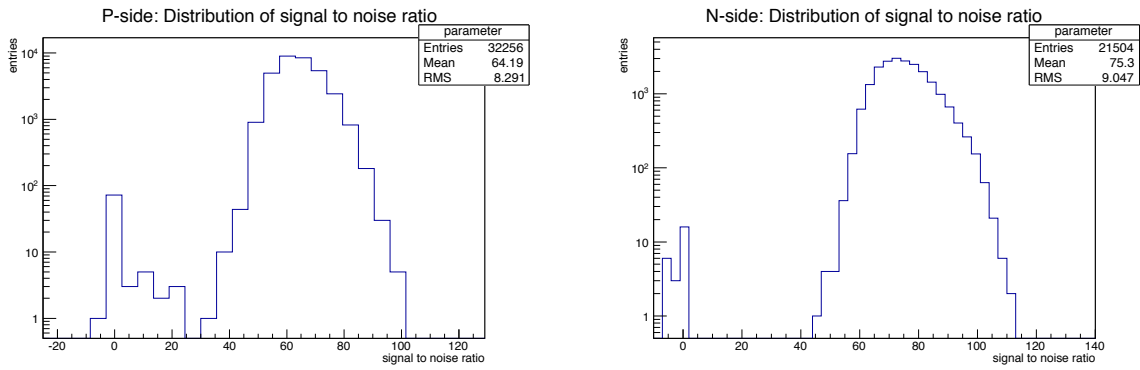


Figure 6.3: Distribution of SNR of the 42 Origami -Z flexes. Left is for p-side and right is for n-side. The number of entries is the total number of channels.

For the ladder assembly, we need to define the class of the Origami into two classes, A and C. To determine the classes, we defined two types of channel, good channel and dead channel.

We determined to use the SNR to choose the bad and dead channel. First, as the result shown in Fig. 6.2, we observed two groups whose SNR is less than 25 and more than 25. We therefore considered it is reasonable to define the dead channel as the channel whose SNR is less than 25. Then we defined class-C Origami as the Origami has dead channel. We define class-A Origami as the Origami has no dead channel.

- dead channel
The channel whose SNR is smaller than 25.

We define Origami-flex classes as below.

- Class A
There is no dead channel.
- Class C
If there is at least one dead channel, we define class-C.

Examples of the distributions of SNR of these classes of Origami flexes are shown in Figs. 6.4, 6.5.

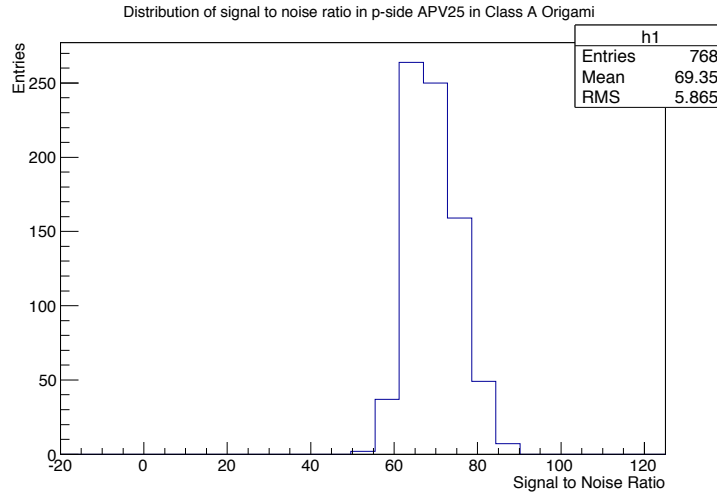


Figure 6.4: Distribution of signal to noise ratio of p-side APV25 in class A Origami. In p-side there are totally six APV25 chips thus the number of Entry is $128 \times 6 = 768$. There is no any dead channel.

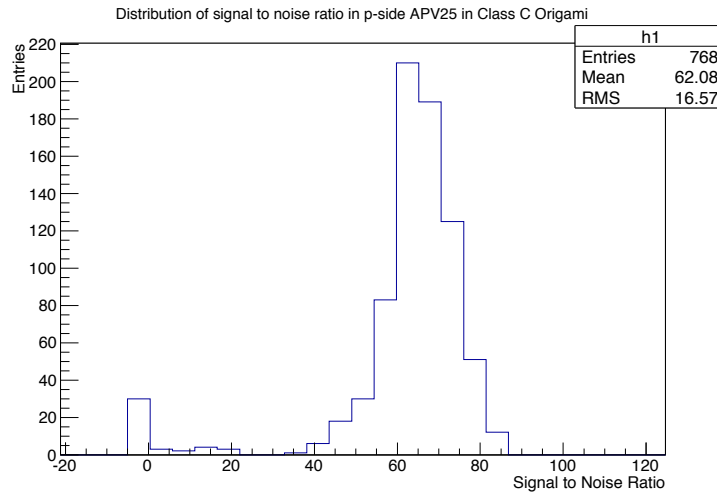


Figure 6.5: Distribution of signal to noise ratio of p-side APV25 in class C Origami. In p-side there are totally six APV25 chips thus the number of Entry is $128 \times 6 = 768$. There are dead channels in the region $SNR < 25$.

6.3 Result

Through the measurement of APV25 chips, we confirmed the quality of Origami flexes with the APV25 chips by the APVDAQ. We succeeded to read the APV25 chips through the signal lines in the Origami flex, and we judged readable Origami flex has the healthy connections.

Table. 6 is our result of the measurement of Origami flex and APV25.

Table 6: The class of the Origami flex with the APV25 chips.

Origami flex	Total measured Origami flex	Class-A	Class-C
Origami -Z	45	39	6
Origami CE	27	24	3
Origami -Z	19	14	5

6.4 Conclusion of Parts Level EQA

We read out the APV25 chips through the signal line of Origami flex. We then succeeded to exclude the broken Origami flexes and APV25 chips by evaluating the SNR. Class-C Origami flexes are used for non-readable ladder, and class-A Origami flexes are used for the ladder production.

7 Assembly Level EQA

The purpose of “Assembly Level EQA” is to trace the quality of the ladder, and to judge whether we can proceed to next assembly procedures. In this section, we see the procedures which allow us to trace the quality of the ladder during the assembly by using the data of class-D ladder. The electrical test is performed in each wire-bonding procedure to confirm whether the quality of electrical components and wire connections are acceptable or not. The number of wire-bonds we perform per ladder is 12800.

In this procedure, there are three important things. First, we must know the behavior of the good channels in each assembly procedure. Second, we must understand the differences of the behavior between un-bonded channel and bonded channel. Finally, we must study whether we can distinguish bad channel such as open and short from good channels by using the information of the electrical test. The purpose of “Assembly Level EQA” is to achieve these three things.

For this, we mainly check how the parameters such as the noise, the raw noise, and the pulse height of calibration curve change in every wire-bonding procedure. These parameters are measured by the APVDAQ. From its information we can check the quality of the ladder step by step, and also can detect the problems such as broken connections during the assembly. All EQA procedures are implemented as mentioned in Chapter 4.

7.1 Study of the Assembly Level EQA

As the pre-experiment for the study of assembly level EQA, we assembled the Single-DSSD readable module, which is described in Appendix A. As mentioned above, we need to know the behavior of the bad channels, which should be detected during the assembly.

In order to detect the bad channels from good channels, we need to know how much the noise level becomes in open channels or short channels in each assembly procedure. From the Single-DSSD readable module assembly, it turned out that there are three patterns of the behavior of channels as follows.

- High noise
High noise channel is open, or short connected channel. Pin-hole strip is also considered as the cause of high noise.
- High pulse height
High pulse height is caused by low capacitance of the channel. In many cases, this is caused by open connection.
- Low pulse height
This is caused by, for example, short connection. If channels have a large capacitance and the provided charge is invariant, pulse height becomes lower.

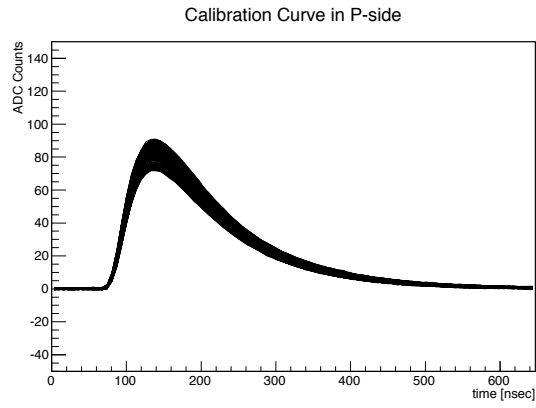
We use “Software Run” and “Internal Calibration Scan” of APVDAQ during the ladder assembly. We calculate the raw noise and the noise by using the data taken from “Software Run”. Also we get the calibration curve for each channel by “Internal Calibration Scan”.

7.2 EQA in Start of the Assembly

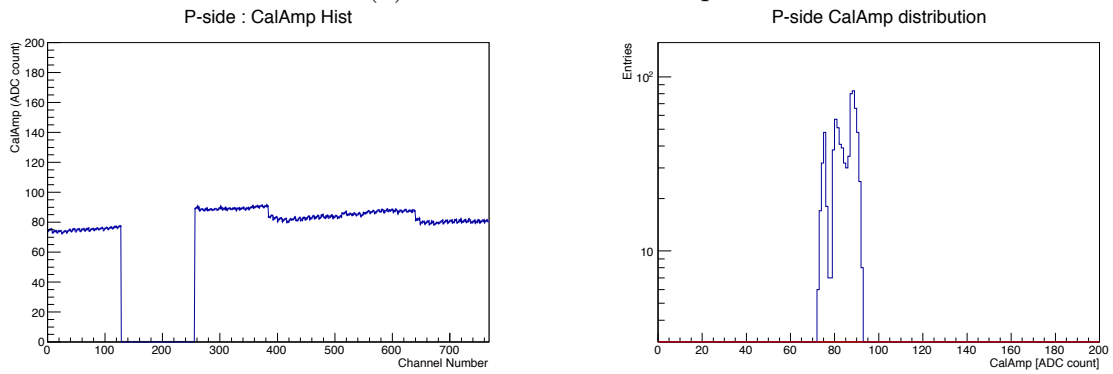
First of all, we check the quality of Origami flex with the APV25 chips before we start wire-bonding. We measure the calibration curve (Fig. 7.1(a), 7.2(a)) and its pulse height, raw noise, and noise. We show the result in this step as following picture. In this step, anything is not connected to the APV25 readout channels. As explained in Chapter. 5.2, there is one broken APV25 (APV P1: channel 128-255) in p-side thus the region of p-side channel 128-255 in following histograms are empty.

In this step, all channels show smooth calibration curve. In p-side, there are totally 640 curves superimposed; this number 640 means the number of readable channels in p-side (128 (the number of channels in APV25) $\times 5$ (the number of readable APV25 chips) = 640). On the other hand in n-side, there are totally 512 curves; this number 512 means the number of channels in n-side ($128 \times 4 = 512$). Pulse height is $70 \sim 100$ in p-side (Fig. 7.1(b)) and $80 \sim 110$ in n-side (Fig. 7.2(b)). The raw noise in p and n-side are shown in Fig. 7.1(c), 7.2(c). The level of raw noise is $1 \sim 3$ ADC (RMS) in p-side, and $2 \sim 4$ ADC (RMS) in n-side.

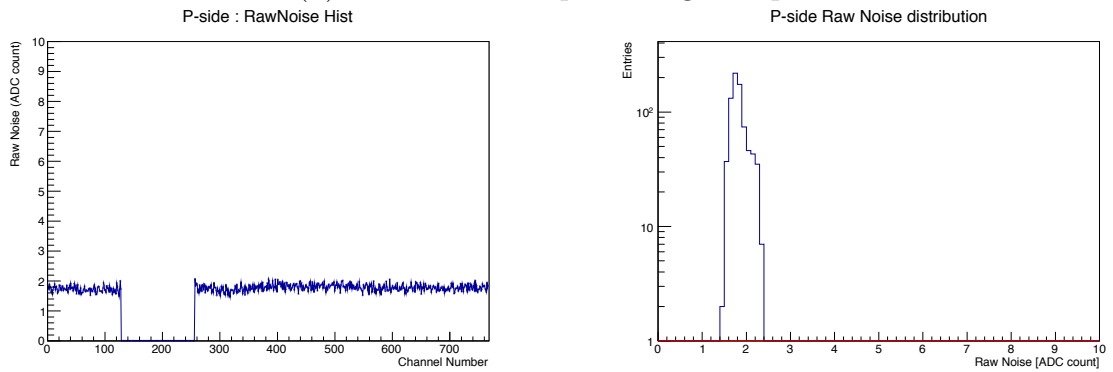
The noise in p and n-side are shown in Fig. 7.1(d), 7.2(d). The noise level is $1 \sim 2$ ADC (RMS) in both side p and n.



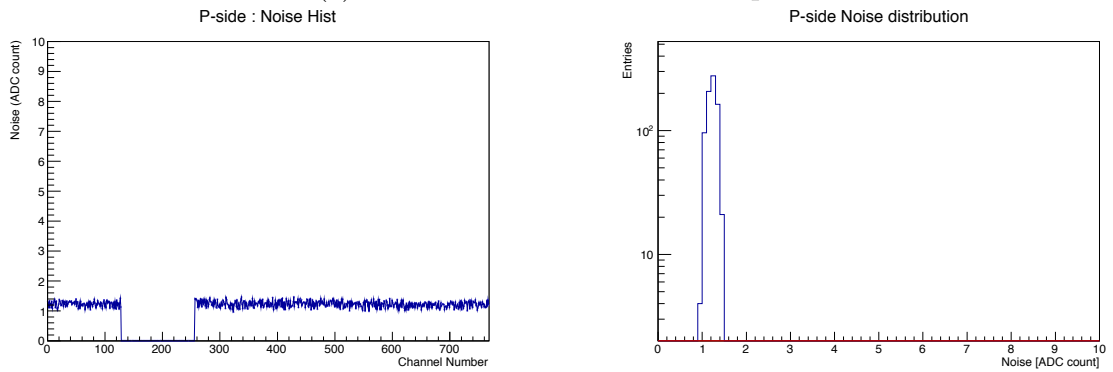
(a) Calibration curve in p-side



(b) Distribution of pulse height in p-side

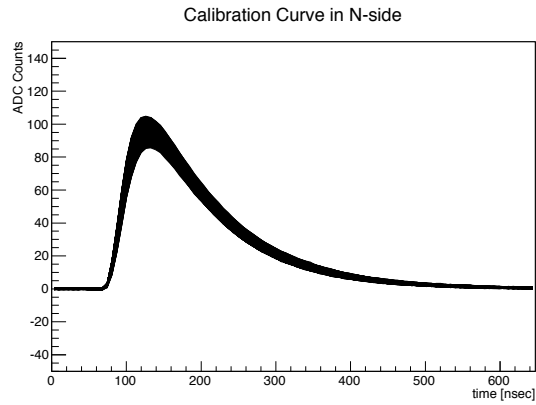


(c) Distribution of raw noise in p-side

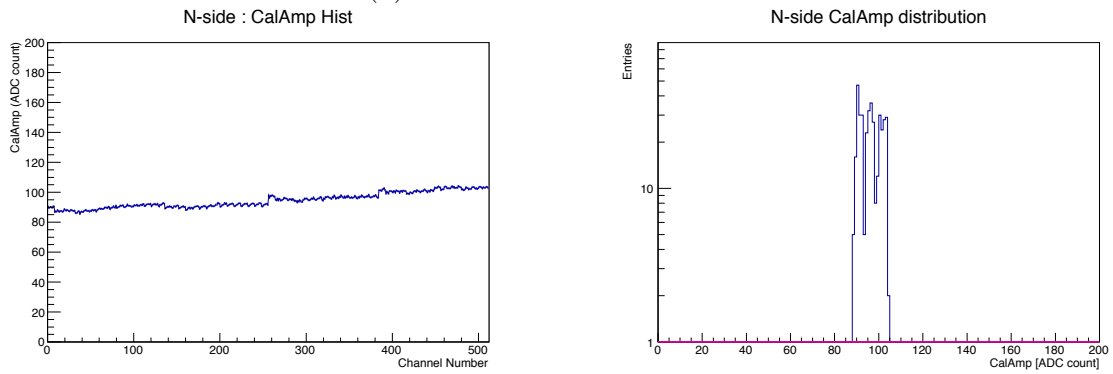


(d) Distribution of noise in p-side

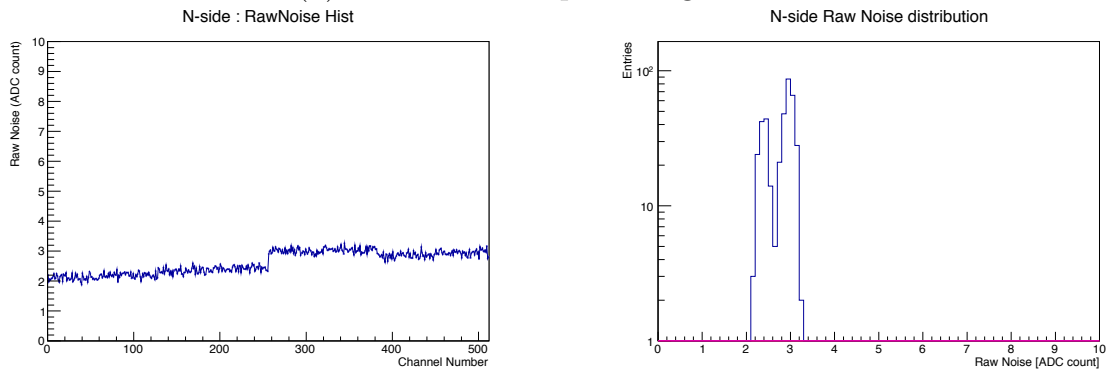
Figure 7.1: EQA data for Origami p-side before ladder assembly



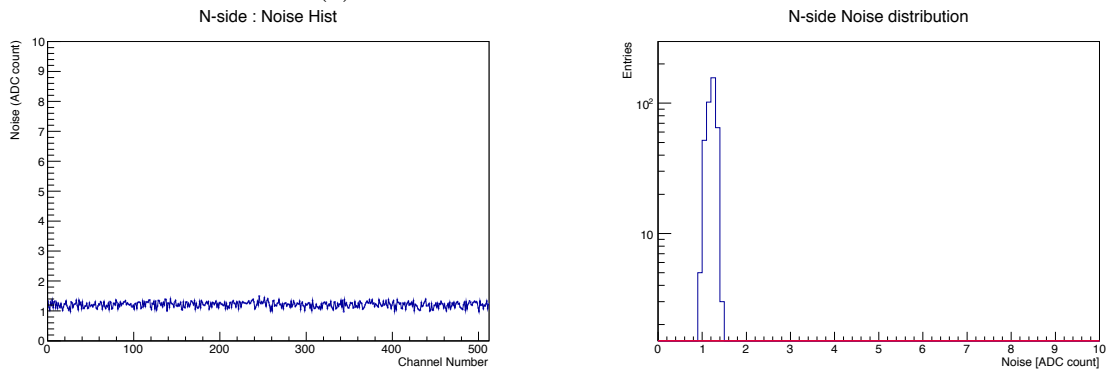
(a) Calibration curve in n-side



(b) Distribution of pulse height in n-side



(c) Distribution of raw noise in n-side



(d) Distribution of noise in n-side

Figure 7.2: EQA data for Origami n-side before ladder assembly

7.3 EQA after Wire-bonding (inner-loop) in N-side

In this section we see the result after the wire-bonding in n-side inner-loops (Fig. 4.7). In this step, n-side APV25 - PA0 and PA0 - DSSD are connected (only even number strips).

For evaluating the noise correctly, we developed the method of calculation of noise by following way. Because the common-mode shifts between connected and unconnected channels are different due to the capacitance of the channels, we must separate them into two groups in the CMC calculation. Since the inner-loop wires correspond to even channel numbers, common-mode shifts are different between even and odd channels. Considering this point, we invented the method of the calculation of noise as following formulae.

$$CMS_{\text{inner}}[n][i] = \frac{1}{64} \sum_{j=0}^{63} (Raw\ ADC[n][i][2j(\text{ch})] - PED[i][2j(\text{ch})]) \quad (7.1)$$

$$CMS_{\text{outer}}[n][i] = \frac{1}{64} \sum_{j=0}^{63} (Raw\ ADC[n][i][2j + 1(\text{ch})] - PED[i][2j + 1(\text{ch})]) \quad (7.2)$$

Here, index n and i mean event and number of APV25 chip, respectively. Results of noise in this section are calculated by these formulae. Since the APV25 and the DSSD are connected electrically, the noise level in n-side becomes higher because of increase of the capacitance. As shown in Fig. 7.3(a), calibration curves in n-side become noisier. Calibration curves in n-side are divided into two groups. There are totally 512 curves. Yellow curve means the un-bonded one, and red curves are considered to be open one in inner-loops thus should be similar shape to un-bonded channels. Black curves are the curves of bonded channel.

We use two colors red and purple to show the bad channels: red indicates the open channels whose connection was not performed and we verified its connection directly by the electrical probe test, and purple channels are considered to be open channels from its behavior but not verified by the electrical probe test.

The raw noise in n-side is shown in Fig. 7.3(c). The raw noise of connected even number channels (blue one) ranges from 35 to 50. The raw noise of unconnected even number channels (red and purple one) ranges from 20 to 30. Odd number channels show the raw noise ranging from 20 to 30.

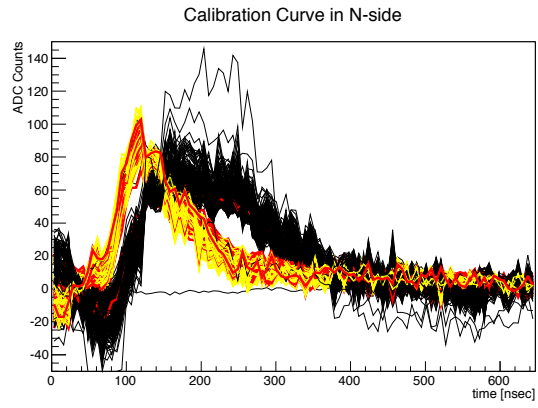
The noise in n-side is shown in Fig. 7.3(d). Connected even number channels (blue one) show the noise ranging from 10 to 20, and unconnected even number channels (red and purple one) show the noise ranging from 50 to 60 while some are ranging from 10 to 15 and from 35 to 40. Odd number channels show the noise ranging from 1 to 5. Again this noise is defined as the CMC noise and there are two type of common-mode shifts. There are some high noise channels show 60 ADC (RMS), these are considered to be caused by the wrong method of CMC in even number channels.

In this procedure, CMC for even number channels works for connected channels because common-mode shifts in even number channels are calculated by averaging the common-mode shift of each even number channel as shown in Eq. (7.1). After the calculation, these common-mode shifts are subtracted from each channel. This CMC is done for even number channels globally. However, if there are unconnected channels whose common-mode shift is different from that of connected channels, this CMC will not work for unconnected channels. These unconnected channels therefore are expected to be noisier because of the wrong CMC method.

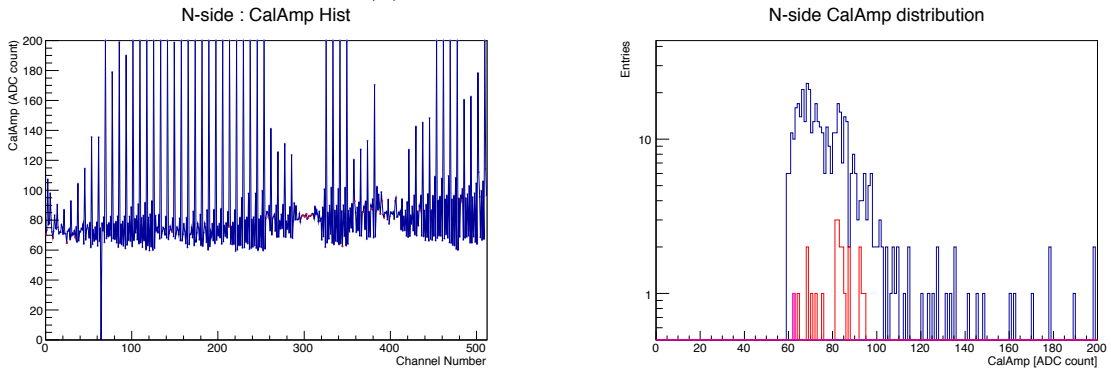
From these results, following behaviors of the observable in healthy channels and bad channels are observed.

- Calibration curve
Shapes are divided into two types, one is higher another is relatively lower.
- Raw noise
Divided into two types. Unconnected channels show the raw noise ranging from 10 to 20, and connected good channels show the raw noise ranging from 20 to 30. Bad channels are detectable by this information.
- Noise
Divided into two types. Odd number channels are not connected and thus show low noise (ranging from 1 to 5). On the other hand in even number connected channels, the noise ranges from 10 to 20 for good channels. There are channels show the noise ranging from 50 to 60 which considered to be open. Thus bad channels are detectable by checking the existence of the high noise channels.

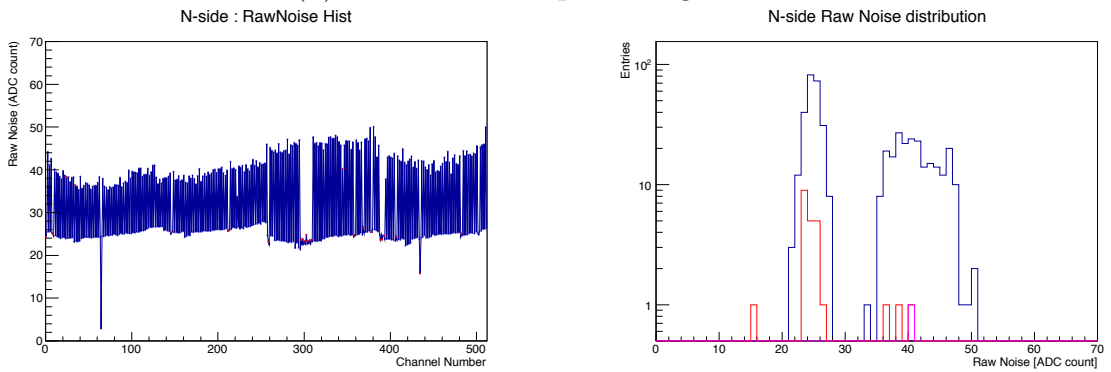
As the results shown in 7.3, we can recognize the differences of the behavior of unconnected bad channels and connected good channels by using the information of noise. In Fig. 7.3(b), there are some channels whose pulse height is high (more than 200). This high value is caused by the internal calculation of the APVDAQ; in the APVDAQ, pulse height is calculated by fitting the curve. The pulse height is defined as the height of the fitted curve. However, if the fitting is performed badly, the pulse height would show unusual value as shown in Fig. 7.3(b). That is the reason why there are many channels whose pulse height is very high.



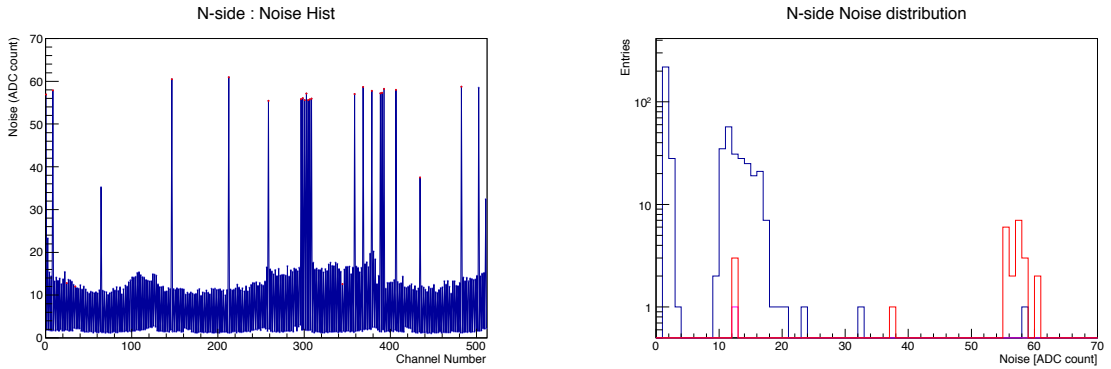
(a) Calibration curve in n-side



(b) Distribution of pulse height in n-side



(c) Distribution of raw noise in n-side



(d) Distribution of noise in n-side

Figure 7.3: EQA data for n-side after wire-bonding in inner-loop of n-side

7.4 EQA after Wire-bonding (outer-loop) in N-side

In this section we see the result after the wire-bonding in n-side outer-loops (Fig. 4.8). In this procedure, odd number strips are wire-bonded and thus all channels in n-side are wire-bonded; all APV25 chips in n-side are connected to the DSSD.

First calibration curves in n-side are divided into three groups as shown in Fig. 7.4(a) (There are totally 512 curves). One is black curve whose pulse height is lower, second is black curve whose pulse height is higher, and third is red one showing high pulse height. As the result shown in Fig. 7.4(b), bonded channels (blue points) show pulse height ranging from 30 to 50. Channels considered to be open (red and purple points) show pulse height of more than 70.

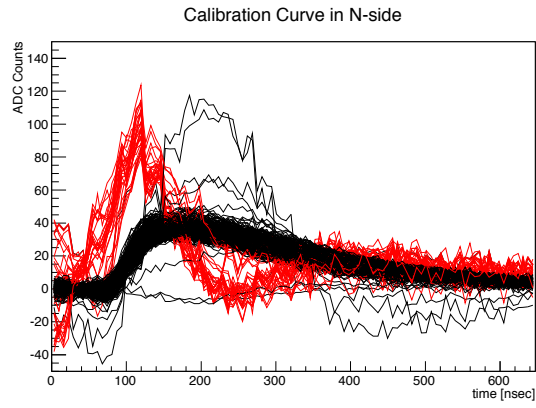
The raw noise in n-side is shown in Fig. 7.4(c). Connected channels (blue one) show the raw noise ranging from 10 to 20 while some are showing the value of outside that range. On the other hand, channels considered to be open (red and purple one) are showing the raw noise ranging from 20 to 30.

The noise in n-side is shown in Fig. 7.4(d). Connected channels (blue one) show the noise ranging from 5 to 20 while some are showing the value of outside that range. On the other hand channels considered to be open (red and purple one) are showing the noise ranging from 25 to 35. These noisy channels are considered to be caused by the wrong method of CMC as described in Chapter. 7.2.

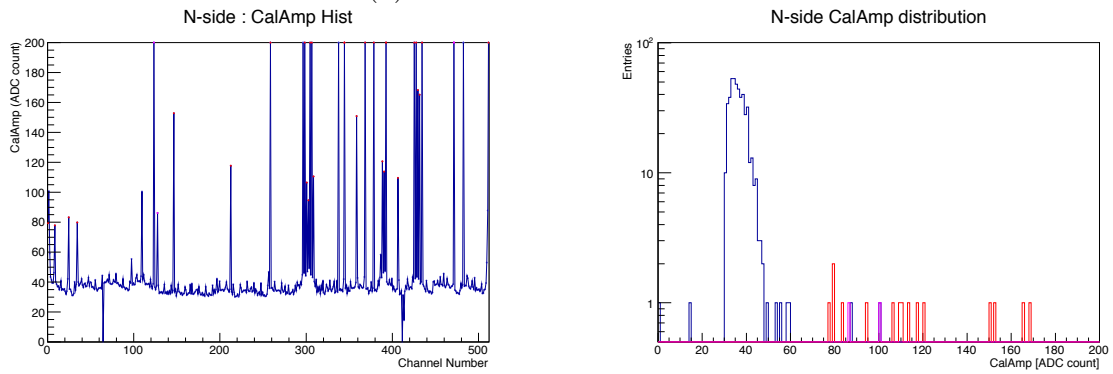
From these results, following behaviors of the observables in healthy channels are observed.

- Calibration curve
Good channels are showing pulse height ranging from 30 to 50. On the other hand, bad channels are showing pulse height of more than 70.
- Raw noise
Divided into two patterns. Connected good channels show the raw noise ranging from 10 to 20. On the other hand bad channels considered to be open show the raw noise ranging from 20 to 30. This differences is distinguishable.
- Noise
Divided into two types. Connected good channels show the noise ranging from 5 to 20. On the other hand in bad channels considered to be open, the noise becomes more than 25. As shown in Fig. 7.4(d), good channels and bad channels are distinguishable.

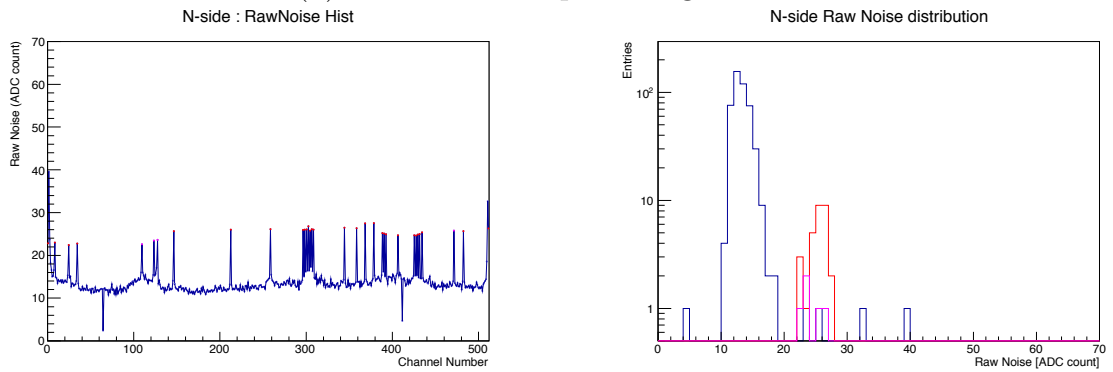
We checked that we can recognize the differences of the behavior of good and bad channels by using these information. Comparing the result taken before the wire-bonding, the noise level becomes higher and pulse height becomes lower. This is considered to be caused by the capacitance of the DSSD. These results shown above are consistent with this aspect.



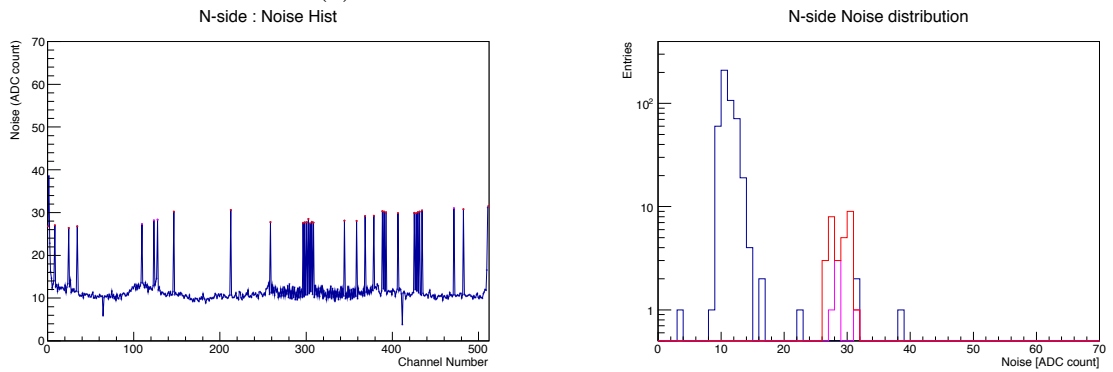
(a) Calibration curve in n-side



(b) Distribution of pulse height in n-side



(c) Distribution of raw noise in n-side



(d) Distribution of noise in n-side

Figure 7.4: EQA data for n-side after wire-bonding in outer-loop of n-side

7.5 EQA after Wrapping

As mentioned in Chapter 4, wrapping procedure may break the wire-bonds in n-side when we attach the PA1/2 on the Origami flex. To check the condition of the wire-bonds in n-side, the electrical test in this step is required. However in this step, we only check whether there are any changes in the data taken after the wire-bonding procedure in n-side. If it is turned out that there is a crucial accident, for example, a lot of broken wire-bonds caused by wrapping, we suspend the assembly if repair of wire-bonds seems to be difficult.

7.6 EQA after Wire-bonding on the Bias Voltage Pad

Until this procedure, all the bias pads have not been performed. After this procedure, there are the wire-bonds on the bias pad in both p and n-side as shown in Fig. 7.5. We therefore can impose the bias voltage on the DSSD and can measure the I-V curves shown in Fig. 7.6. We confirmed that the DSSD shows the behavior expected by the inspection of company (HPK). As the result shown in Fig. 7.6, we observed healthy value of current showing $3 \mu\text{A}$ at 100 V (+50 V for n-side and -50 V for p-side).

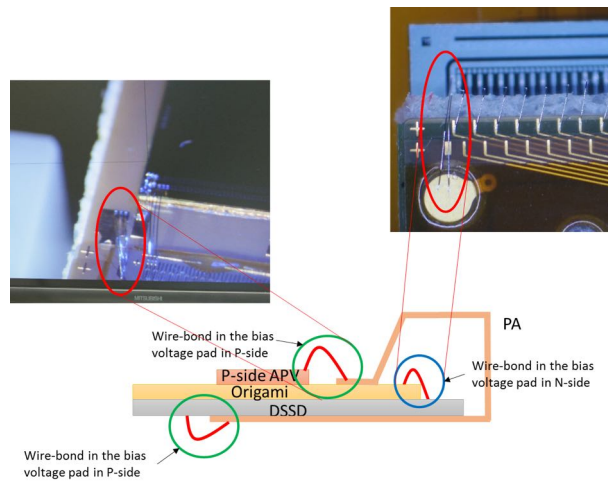


Figure 7.5: The wire-bonding on the bias voltage pad.

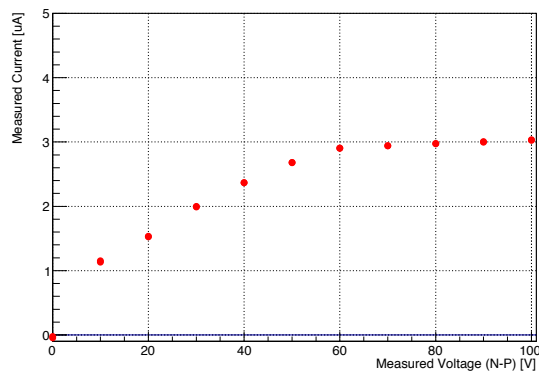


Figure 7.6: I - V curve of the DSSD.

7.7 EQA after Wire-bonding in (inner-loop) in P-side

In this section we see the result after the wire-bonding in p-side inner-loops (Fig. 4.12). After this wire-bonding, even number channels on the APV25 chips and the DSSD are connected electrically.

First we see the data of p-side in this wire-bonding procedure. The calibration curves in p-side are divided into two groups as shown in Fig. 7.7(a). There are totally 640 curves. Black curves are of bonded channels, and yellow curves of un-bonded channels. Red curves are of bad channels (open channels) in bonded channels. We changed the width of the red curves so that we can see. There are channels showing high pulse height as shown in Fig. 7.7(b). Red point channels are open bad channels, blue point channels are considered to be good connected channel. Only by this information of the pulse height, the bad channel is not distinguishable from the good channels.

The raw noise in p-side is shown in Fig. 7.7(c). Connected (or un-bonded) good channels (blue) show the raw noise ranging from 60 and 110. Also bad channels considered to be open in bonded channels (red) show the raw noise around 40. The noise in p-side is shown in Fig. 7.7(d). Connected good channels (blue one) show the noise ranging from 10 to 30, and un-bonded channels showing the noise of less than 10 - 15. On the other hand bad channels considered to be open (red) show the noise ranging from 55 to 60. These noisy channels (red) are considered to be caused by the wrong method of CMC, which is described in the procedure of wire-bonding in n-side. From this procedure, we calculated the CMS in n-side without distinguishing the even and odd number channels because even and odd number channels are wire-bonded, thus both even and odd number channels have same CMS. For p-side, we calculated the CMS for the even and odd number channels respectively.

Next, we see the result of n-side. Although there is no any new wire-bond in n-side, noises in the open channels become larger as shown in Fig. 7.8.

The raw noise in n-side also becomes larger as shown in Fig. 7.8. Comparing the result shown in Fig. 7.4, the raw noise in connected channels changed from 10 - 20 to 20 - 50 and in channels considered to be open (red and purple one) changes from 20 - 30 to 80 - 100. The noise in n-side connected channels changes from 5 - 20 to 10 - 30 and in channels considered to be open (red and purple one) changes from 25 - 35 to 100 - 130.

From these results, following behaviors of the observables in healthy and bad channels are observed.

- Calibration curve

In p-side, shapes of calibration curves are mainly divided into two groups, one is relatively high, another is low. Connected channels show low pulse height and unconnected channels show high pulse height. However from the result of Fig. 7.7(b), connected good channels and bad channels are not distinguishable.

On the other hand in n-side, result is similar to the previous one. However, noisy channel becomes noisier as shown in Fig. 7.8 after the wire-bonding in p-side inner-loops.

- Raw noise

In p-side, although the number of samples of open channels is quite few, open channels in bonded inner-loops showing low raw noise of 40 as shown in Fig. 7.7(c) and unconnected or bonded inner-loop channels show the raw noise of around 60 - 110.

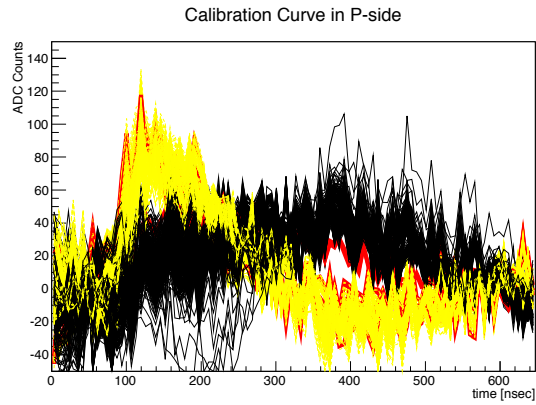
On the other hand in n-side, raw noise becomes larger for all channels even there is no any new wire-bond in n-side. Especially for open bad channels, change of raw noise is larger than that of connected good channels.

- Noise

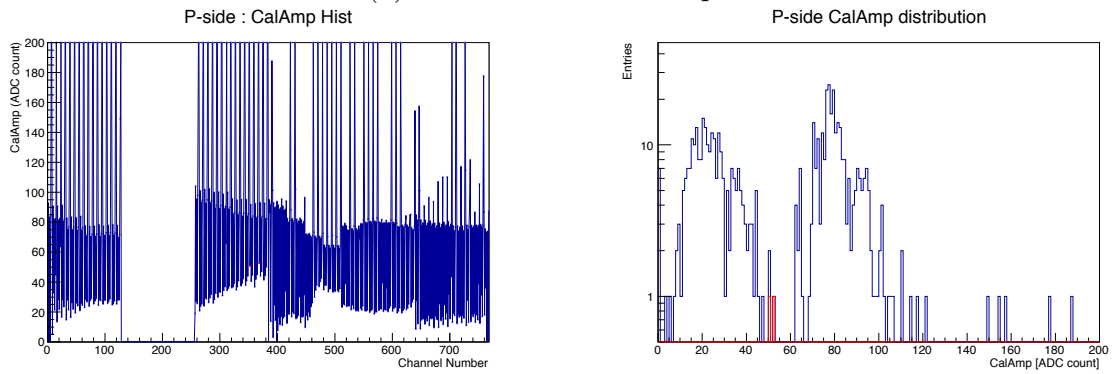
In p-side, open bad channels in wire-bonded even number channels show high noise. Also, wire-bonded even number good channels shows the noise ranging 10 - 30. In this procedure, good and bad channels are distinguishable.

On the other hand in n-side, the noise level is divided into two patterns; good and bad channels are distinguishable.

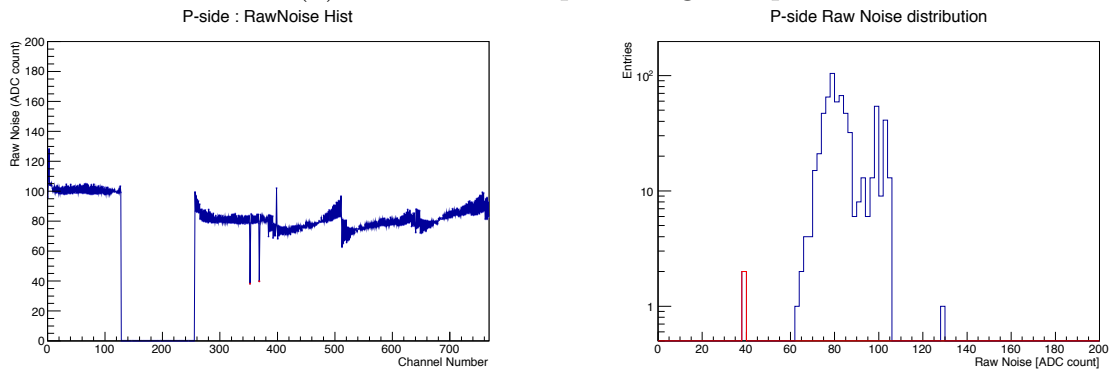
We checked that we can recognize the differences of the behavior of good and bad channels in p-side by using the information of noise and raw noise in this step. We therefore can detect bad channels. After this procedure, there is almost no change in n-side. We therefore see only the result of p-side until we see the data with a bias voltage.



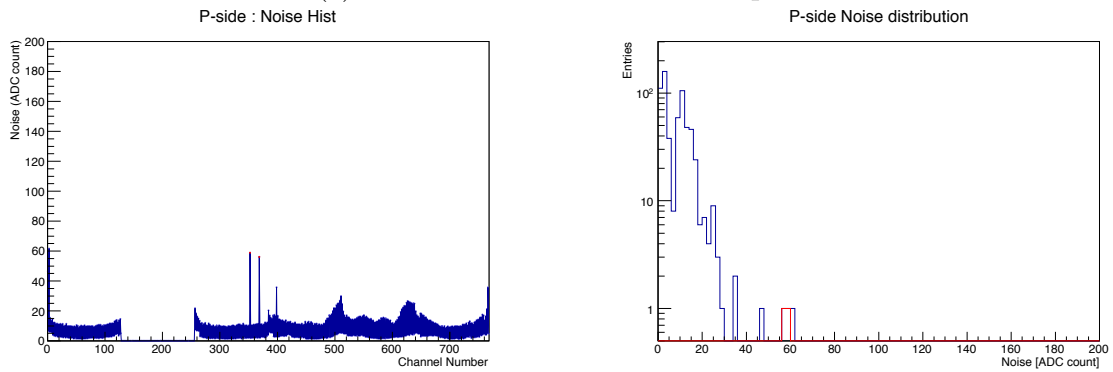
(a) Calibration curve in p-side



(b) Distribution of pulse height in p-side

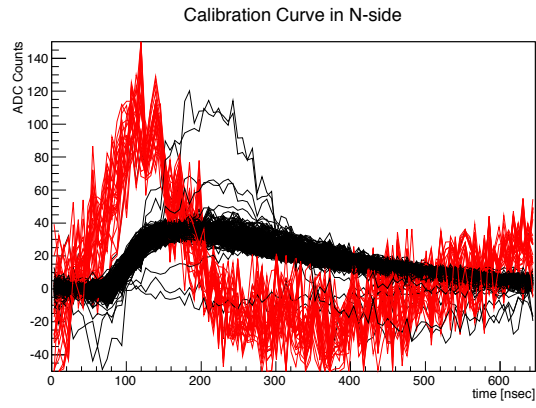


(c) Distribution of raw noise in p-side

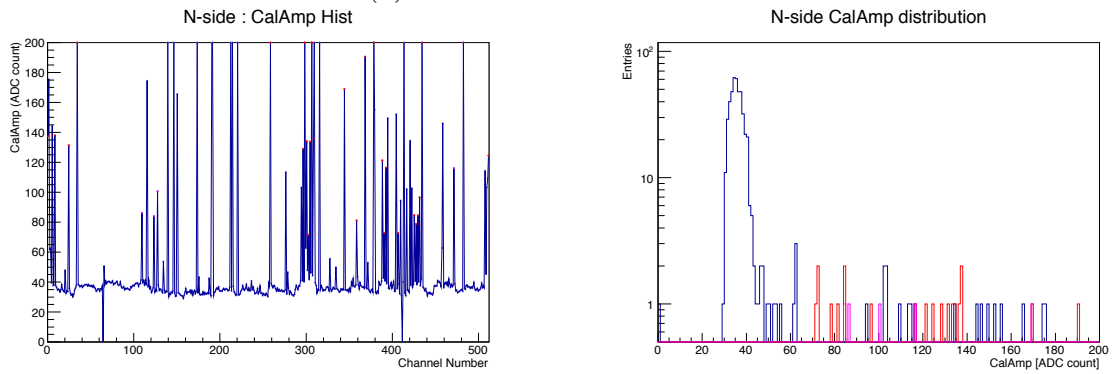


(d) Distribution of noise in p-side

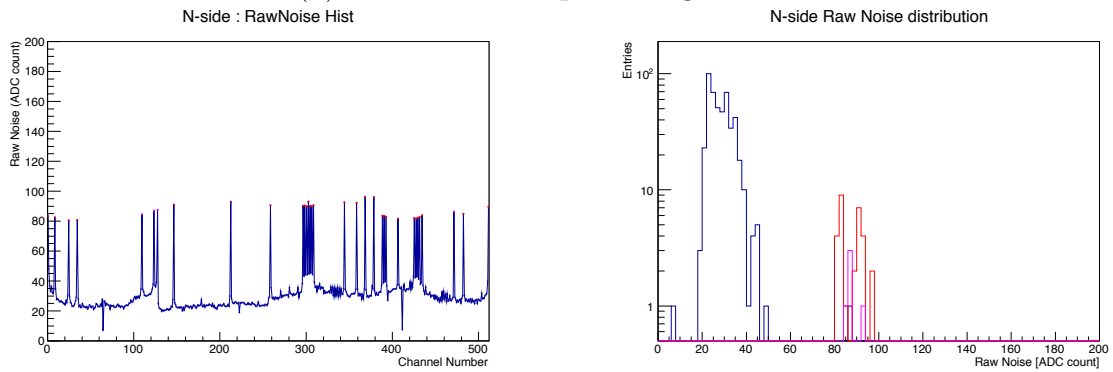
Figure 7.7: EQA data for p-side after wire-bonding in inner-loop of p-side



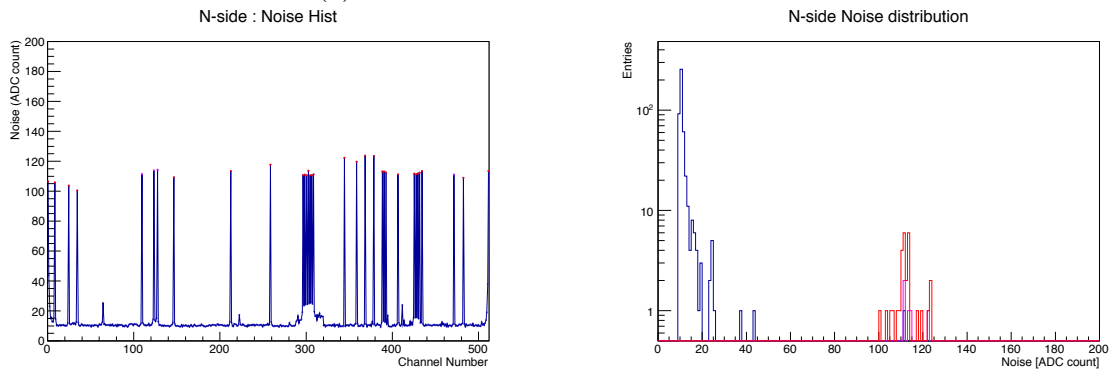
(a) Calibration curve in n-side



(b) Distribution of pulse height in n-side



(c) Distribution of raw noise in n-side



(d) Distribution of noise in n-side

Figure 7.8: EQA data for n-side after wire-bonding in inner-loop of p-side

7.8 EQA after Wire-bonding (middle-loops) in P-side

In this section we see the result after the wire-bonding in p-side middle-loops (Fig. 4.13), thus only some odd strips (1, 5, 9, 13, 17, ... , 121, 125, ...) in p-side are wire-bonded. In this procedure, even number channels and channel 1, 5, 9, 13, 17, ... , 121, 125, ... on the APV25 in p-side are connected to the DSSD.

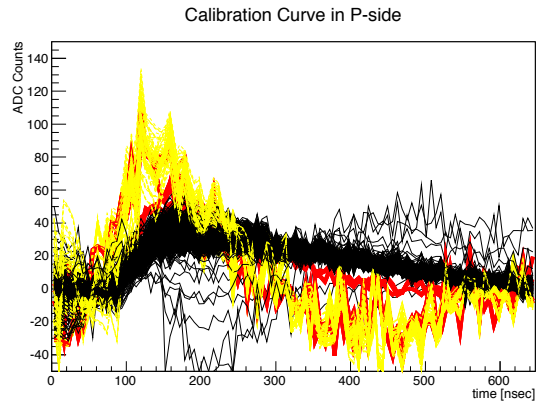
First, calibration curves in p-side are divided into two groups as shown in Fig. 7.9(a). There are totally 640 curves superimposed; black curves are bonded channels whose pulse height is lower, and yellow curves are of un-bonded odd number channels 3, 7, 11, 15, ..., 123, 127, ... whose pulse height is higher than black curves. Red curves are of the bad channels. As shown in Fig. 7.9(b), bad channels (red one) is not distinguishable from good channels.

The raw noise in p-side is shown in Fig. 7.9(c). Connected channels (blue except channel 3, 7, 11, ... , 123, 127, ...) show the raw noise ranging from 20 - 60 and un-bonded channels show 70 - 100. Channels considered to be open in bonded channels (red) show the raw noise of 25 or 80. We can recognize two spikes near channel 350 and 370 as shown in left of Fig. 7.9(c). The noise in p-side is shown in Fig. 7.9(d). There are two groups as shown in right of Fig. 7.9(d). One group show the noise ranging from 5 to 20 and another group shows the noise ranging from 70 to 100. Channels considered to be open show un-distinguishable noise.

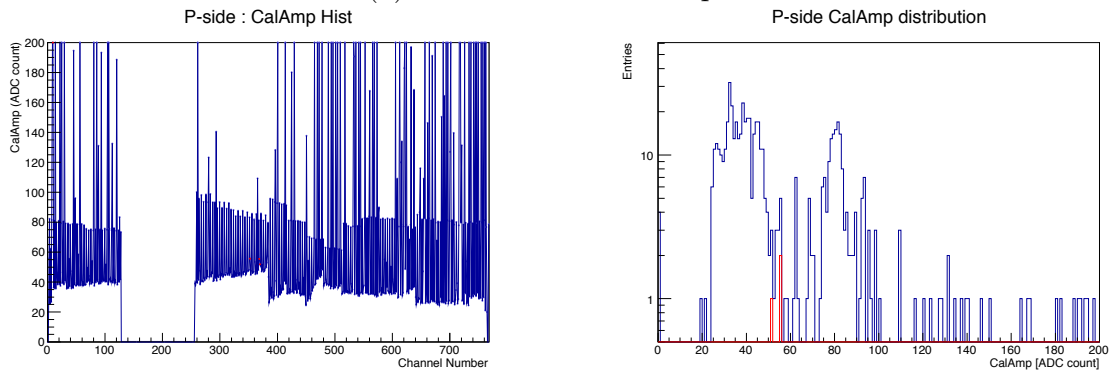
From these results, following behaviors of the observables in healthy and bad channels are observed.

- Calibration curve
From this information, it is difficult to distinguish the bad channels from good channels.
- Raw noise
As shown in left of Fig. 7.9(c), bad channels near channel 350 and 370 in bonded region show the raw noise of 25 which is relatively low comparing with adjacent channels. We can distinguish bad channels by this information.
- Noise
From this information, it is difficult to distinguish the bad channels from good channels.

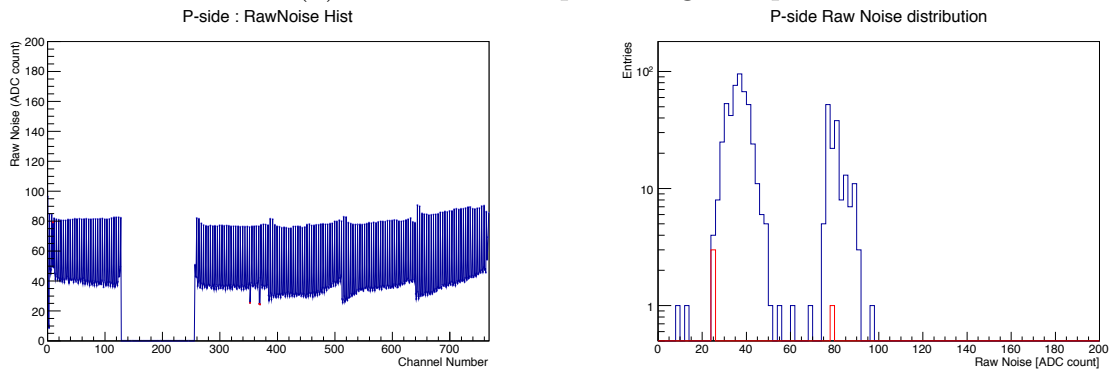
Bad channel is recognizable by using the distribution of raw noise. Connected channels become noisier and its pulse height becomes lower.



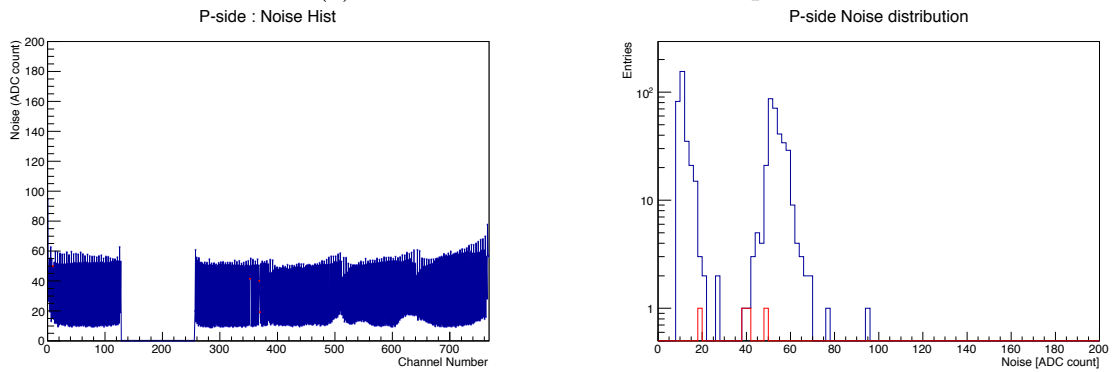
(a) Calibration curve in p-side



(b) Distribution of pulse height in p-side



(c) Distribution of raw noise in p-side



(d) Distribution of noise in p-side

Figure 7.9: EQA data for p-side after wire-bonding in middle-loop of p-side

7.9 EQA in Wire-bonding (outer-loops) in P-side

In this section we see the result after the wire-bonding in p-side outer-loops (Fig. 4.14), thus all channels in p-side are wire-bonded in this procedure. As shown in Fig. 7.10, different from the result in previous section, the noise level in p-side becomes lower.

First calibration curves in p-side mainly divided into three groups as shown in Fig. 7.10(a). There are totally 640 curves. Black is of connected channel, and red is of bad channel whose pulse height is higher. We changed the width of the red curves so that we can see. Although the distribution of pulse height in p-side becomes flatter as shown in left of Fig. 7.10(b), there are still channels show high pulse height. Red channels are open, blue channels are connected channels. Bad channel shows high pulse height, although some good channels also show high pulse height.

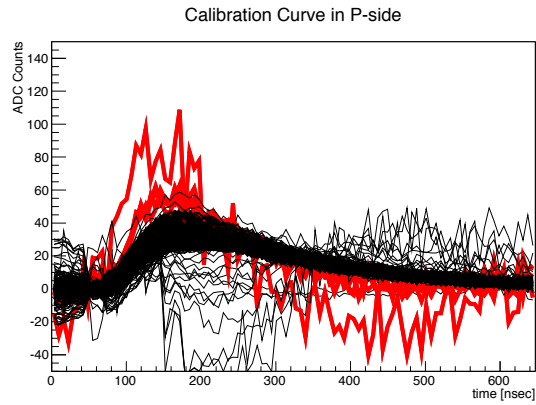
The raw noise in p-side is shown in Fig. 7.10(c). Connected good channels (blue) show the raw noise ranging from 5 to 20 and bad channels considered to be open (red) show the raw noise of 30 or 85. Bad channel is distinguishable from good channels by histogram of raw noise.

The noise in p-side is shown in Fig. 7.10(d). Connected good channels (blue) show the noise ranging from 5 to 20 while some blue channels show the noise out of that range. Also bad channels considered to be open show the noise of 30 or 85. Bad channels are distinguishable from good channels by histogram of noise.

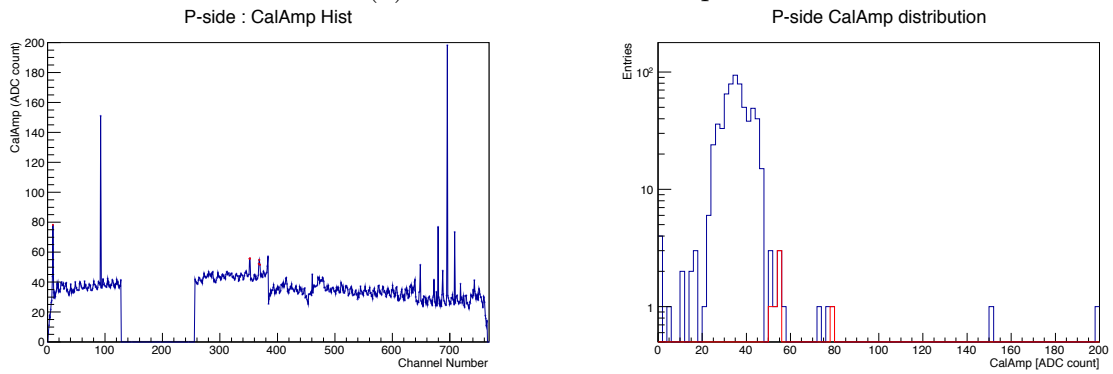
From these results, following behaviors of the observables in healthy and bad channels are observed.

- Calibration curve
As shown in Fig. 7.10(b), bad channels show the pulse height ranging from 50 to 80. This is relatively high value comparing with good channels and we can detect such a bad channel. By using the left of Fig. 7.10(b), we can detect the bad channels.
- Raw noise
As the result shown in Fig. 7.10(c), bad channels show high raw noise of 30 or 85. These bad channels are distinguishable from good channels.
- Noise
As shown in Fig. 7.10(d), bad channels show high noise of 30 or 85. These bad channels are distinguishable from good channels.

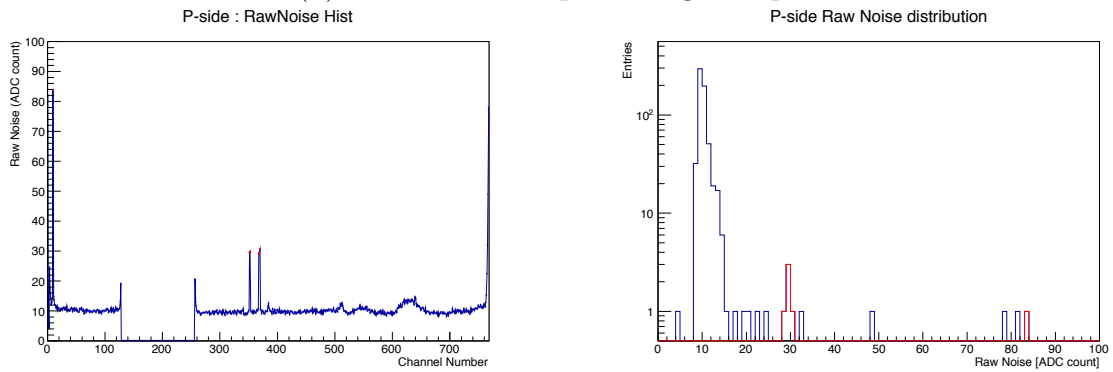
In this procedure, we can detect the bad channels by using the distribution of raw noise and noise. Bad channels show high pulse height, raw noise, and noise comparing to that of good channels.



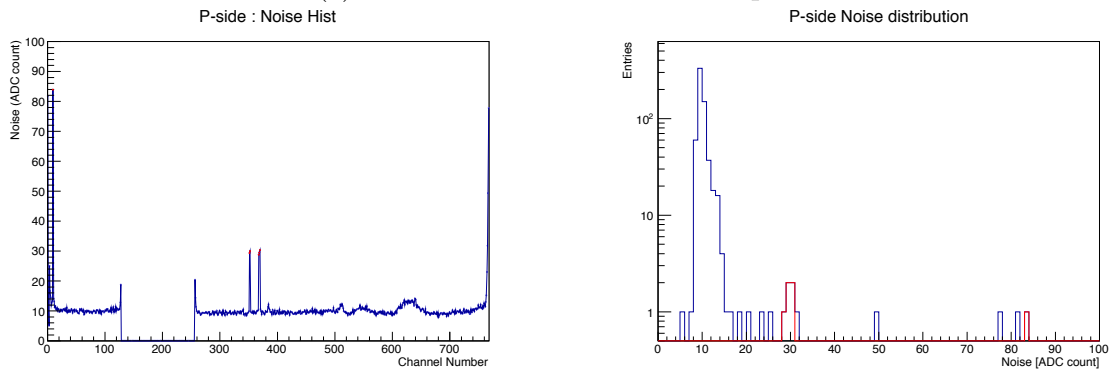
(a) Calibration curve in p-side



(b) Distribution of pulse height in p-side



(c) Distribution of raw noise in p-side



(d) Distribution of noise in p-side

Figure 7.10: EQA data for p-side after wire-bonding in outer-loop of p-side

7.10 EQA with a bias voltage after whole wire-bonding

In this section we see the result after whole wire-bonding procedures with the bias voltage (± 40 V). We first see the result of p-side, after p-side we see the result of n-side.

First calibration curves in p-side become higher after imposing a bias voltage as shown in Fig. 7.11(a). There are totally 640 curves. Black one (connected channel) becomes higher, however red one (open channel) does not become higher. We changed the width of the red curves so that we can see. After imposing the bias voltage, the distribution of pulse height becomes flat as shown in Fig. 7.11(b). Red channels are open showing pulse height of 80. As the result shown in Fig. 7.11(b), pulse height of good channels ranges from 60 to 90 in p-side.

The raw noise in p-side is shown in Fig. 7.11(c). Almost all connected good channels (blue) show the raw noise ranging from 4 to 10 and open bad channels (red) show the raw noise ranging from 10 to 35. The raw noise level becomes lower after imposing a bias voltage; this cause is considered to be the effect of the depletion of the DSSD. After full depletion, there is almost no charge in the DSSD thus it is considered this depletion makes the channels non-noisy. Similar things are appeared in the distribution of noise. The noise in p-side is shown in Fig. 7.11(d). Connected good channels (blue) show the noise ranging from 4 - 10 and bad channels (red) show the noise ranging 10 to 35. The noise is also decreased after imposing the bias voltage. As shown in these results, bad channels are distinguishable from good channels. Similar things are also appeared in the result of n-side.

Next, we see the result of n-side shown in Fig. 7.12. First, calibration curves in n-side changes from 30 - 50 to 70 - 100 after imposing the bias voltage. Calibration curves in n-side are shown in Fig. 7.12(a). There are totally 512 curves superimposed. Red curves considered to be of open bad channels. Black curves are of connected good channels. Distribution of pulse height is shown in Fig. 7.12(b). Bad channels considered to be open (red and purple) show pulse height ranging from 80 to 120. Other almost all good channels (blue) show pulse height ranging from 70 - 100. Bad channels are detectable from the histogram shown in left of Fig. 7.12(b) because bad channels are appeared as the spike. There are two channels show low pulse height near channel 410. These channels are considered to be short, however we have not confirmed by direct inspection such as probe test.

Distribution of raw noise in n-side is shown in Fig. 7.12(c). Connected good channels (blue) show the raw noise ranging from 10 to 40, and bad channels considered to be open (red and purple one) show the raw noise ranging from 30 to 50 while one bad channel show 10. The raw noise level also decreased after imposing the bias voltage comparing with the result in Chapter. 7.3. The noise in n-side is shown in Fig. 7.12(d). Connected good channels (blue) show the noise ranging from 2 to 30, but almost all good channels show 2 - 5. From the result shown in Fig. 7.12(d) bad channels considered to be open (red and purple one) show the noise ranging from 40 to 60 while one bad channel shows the noise of 5.

In p-side, degree of noise and raw noise becomes almost same, however in n-side, there are large differences between the noise and the raw noise. From these results, following behaviors of the observables in healthy and bad channels are observed.

- Calibration curve

In p-side, by using the information of pulse height, it is difficult to detect the bad channels because bad channel has similar pulse height to that of good channel.

On the other hand in n-side, bad channels are detectable by using the distribution of pulse height shown in left of Fig. 7.12(b) because bad channel show detectable high pulse height (80 - 120).

- Raw noise

In p-side, bad channels show high raw noise (10 - 35) comparing with good channels. Thus we can detect the bad channels.

On the other hand in n-side, bad channels show detectable high raw noise (30 - 50) as shown in Fig. 7.12(c).

- Noise

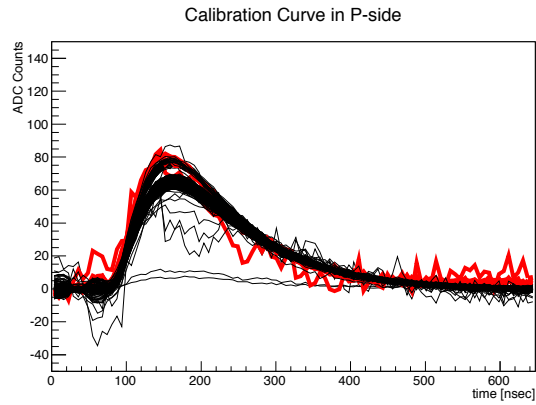
In p-side, the noise level becomes 2 - 10 for connected good channels as shown in Fig. 7.11(d). On the other hand, unconnected bad channels show high noise (10 - 35) as shown in Fig. 7.11(d).

As the result of n-side shown in Fig. 7.12(d), the noise level of bad channels become higher (30 - 50) comparing to the good channels and thus bad channels are detectable.

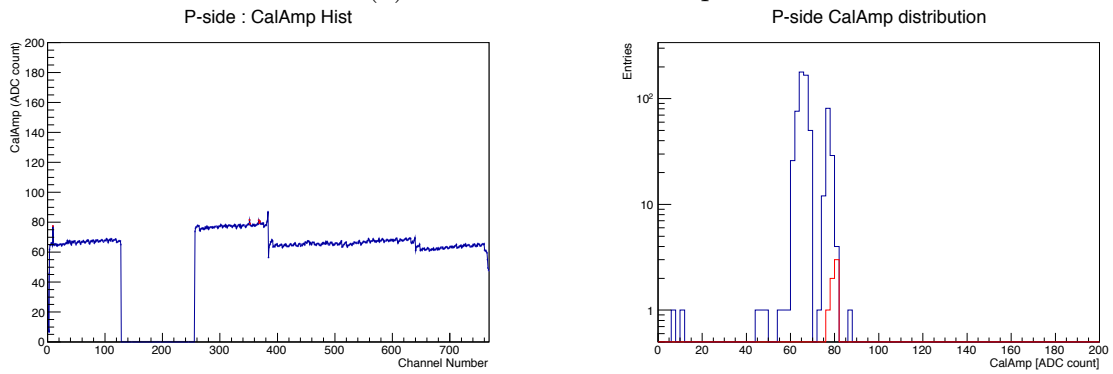
In these EQA procedures, we succeeded to know the behavior of the channels in each wire-bonding procedure. We especially saw the calibration curve and its pulse height, raw noise, and noise. By using the information how each parameter changes in every wire-bonding steps, we can detect the electrical problems and repair it during the assembly.

We confirmed that “Assembly Level EQA” procedures can detect the bad channels through this class-D ladder assembly. Actually, constructed EQA method is already confirmed in the Single-DSSD module assembly and we succeeded to detect the problems through the Single-DSSD module assembly. Detail is described in Appendix A.

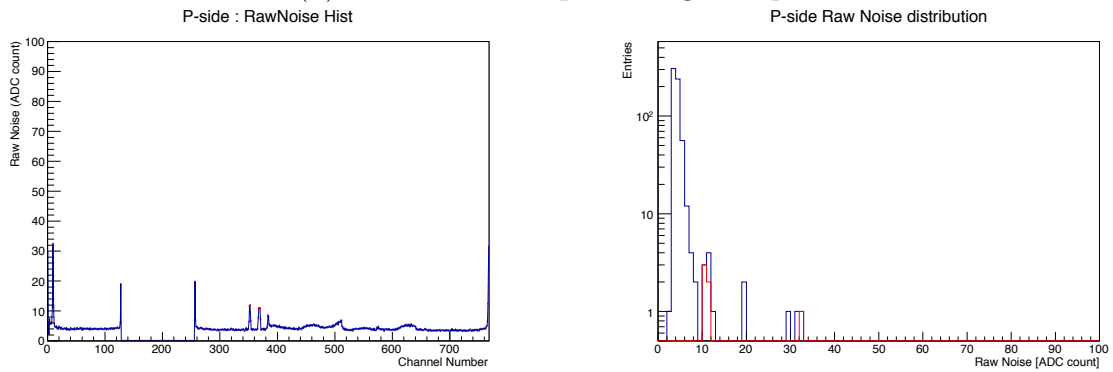
All of these information and the constructed EQA procedures are used for the real ladder (class-A ladder) assembly.



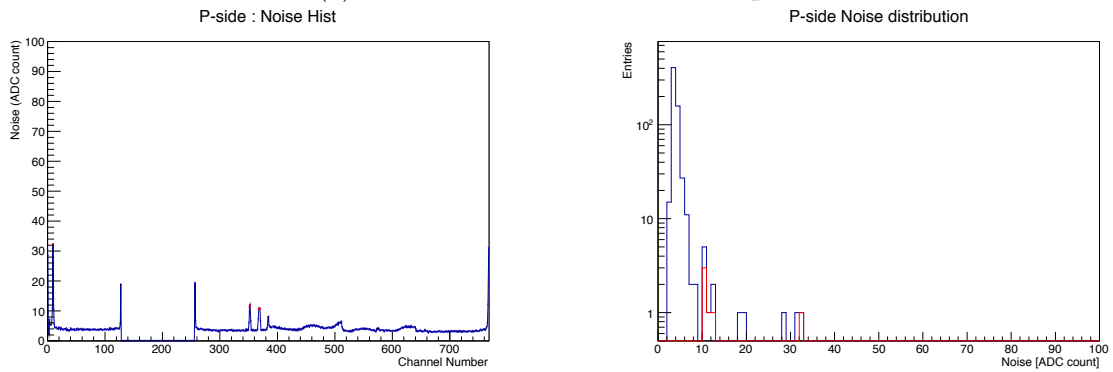
(a) Calibration curve in p-side



(b) Distribution of pulse height in p-side

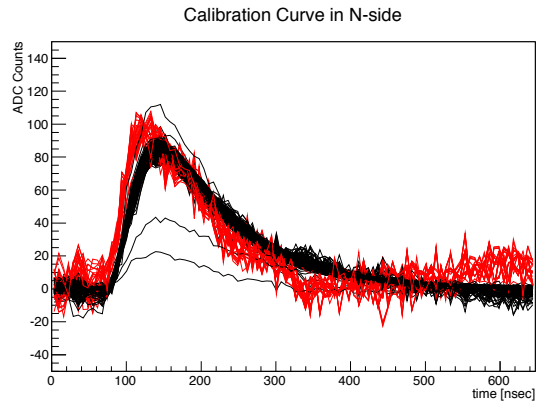


(c) Distribution of raw noise in p-side

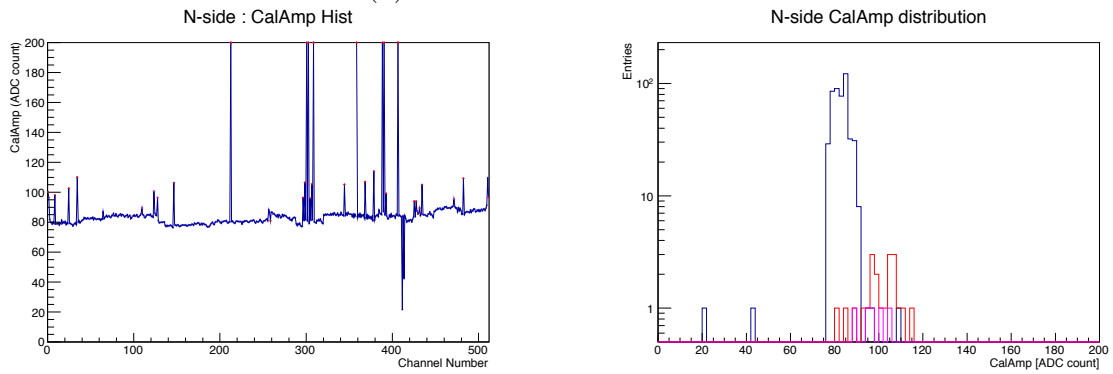


(d) Distribution of noise in p-side

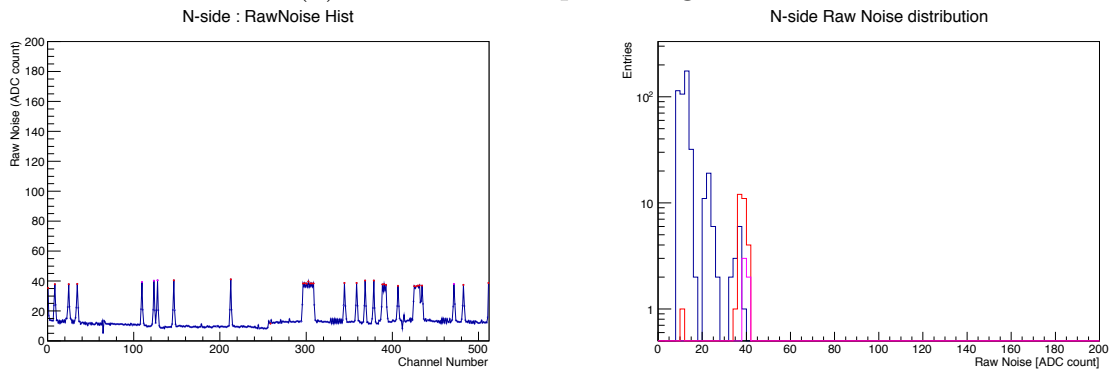
Figure 7.11: EQA data for p-side after wire-bonding in outer-loop of p-side with a bias voltage.



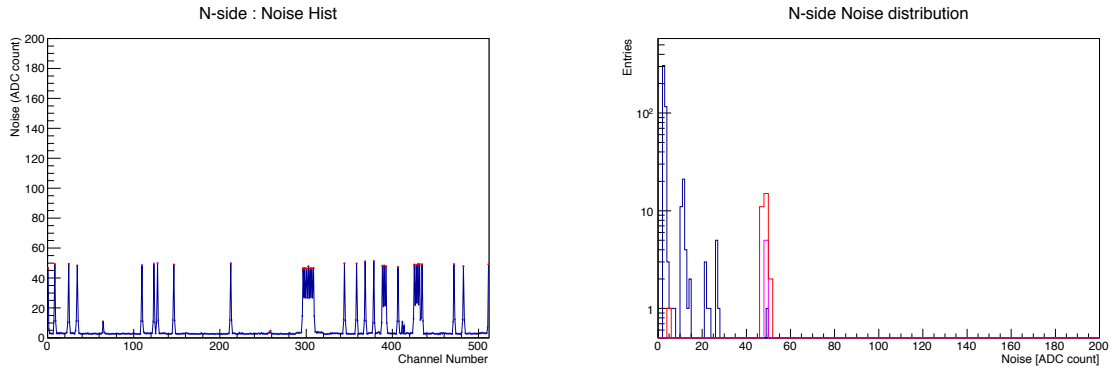
(a) Calibration curve in n-side



(b) Distribution of pulse height in n-side



(c) Distribution of raw noise in n-side



(d) Distribution of noise in n-side

Figure 7.12: EQA data for n-side after wire-bonding in outer-loop of n-side with a bias voltage.

7.11 Conclusion in Assembly Level EQA

Our purpose is to understand the behavior of the channels in each assembly procedure. Also to know how to detect the bad channels by using the information of pulse height, raw noise, and noise. We were able to confirm that our constructed EQA procedure can detect the bad channels by through the study of the procedures of this assembly level EQA.

In actual, we already succeeded to detect the electrical problems in the PA0 by the Single-DSSD module assembly, which is described in Appendix A. Our framework for assembly level EQA is working well.

8 Whole Assembly Level EQA

Purpose of this procedure is to confirm whether assembled ladder is acceptable for the Belle I experiment. As the method of achieving the purpose, ^{90}Sr β -ray source test is implemented. By this test, first we measure hit position, 1 MIP charge, the signal to noise ratio, a cluster size (explained later), and hit timing. Next we measure the signal of each channel to check and list up working channels and un-working channels. Whole setup for ^{90}Sr source test and read out test has been implemented successfully.

In this section, we show the method of ^{90}Sr β -ray source test and how to evaluate the performance of assembled ladder. In this section, we use the word “cluster” when we describe the hit events. For example, we use the word “cluster position” as the meaning of the hit position. Detail explanation of this word is described later.

8.1 Setup of β -ray Source Test

Setup of β -ray test is shown in Fig. 8.1. In this setup, we sandwiches the DSSD between two scintillators as shown in Fig. 8.2, and data-taking are done only when the trigger from two scintillators reaches at the same time. This trigger logic is shown in Fig. 8.3. Thus, only the charged particle penetrate the DSSD is detected in this setup, it enables us to measure the cluster charge for 1 MIP, cluster position, cluster signal-to-noise ratio.

In this setup, we used weak radiation source (Fig. 8.4) whose maximum energy is 2.283 MeV [14]. Because of its low energy, many electrons emitted by ^{90}Sr are stopped by the component of the ladder; especially by the rib.

We can move the hit position by using the movable stage as shown in Fig. 8.5. The quality inspection for all channels is available in this setup.

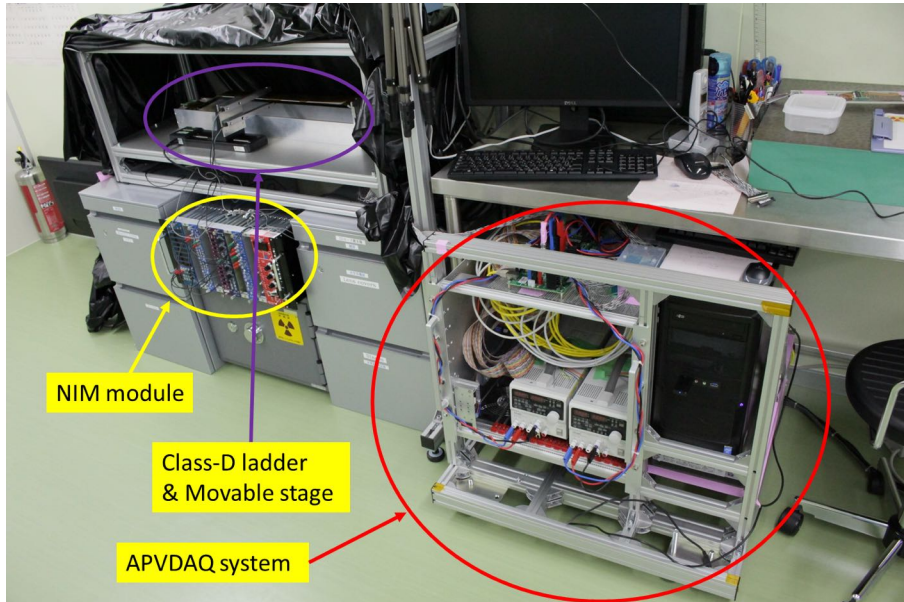


Figure 8.1: Whole setup for source test. There is whole APVDAQ near the setup of β -ray source test for taking the data. In addition there is NIM module for the trigger logic and high voltage supplier for the photomultipliers.

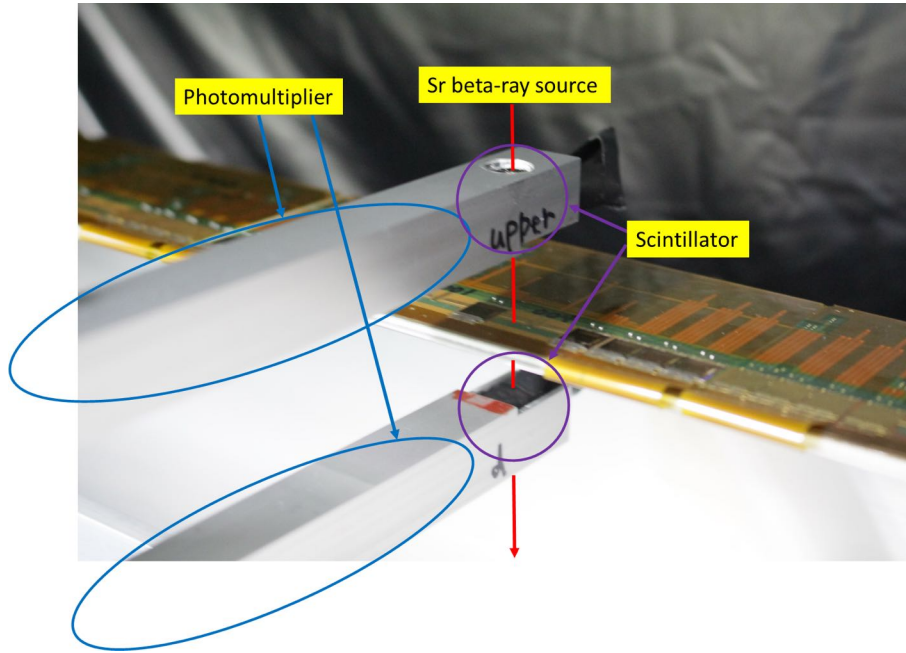


Figure 8.2: Detail of the arm of movable stage. ^{90}Sr source is put on the top of the arm. This stage allows us to get the trigger when β -ray penetrate the DSSD: scintillator, light guide, and photomultiplier are set in the two arms respectively, and trigger is sent to APVDAQ only when ^{90}Sr source hit two scintillator at the same time.

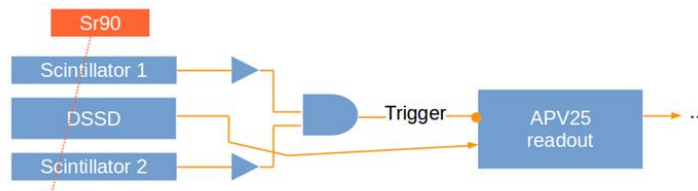


Figure 8.3: Block diagram of trigger logic. The thickness of scintillator 1 and 2 is 0.5 mm and 8 mm, respectively.



Figure 8.4: β -ray source.



Figure 8.5: Movable stage and prototype SVD ladder (Class-D). This movable stage moves through the DSSD horizontally and allows us to scan all strips in the DSSD.

Fig 8.6 shows the geometry of this setup. In this setup, trigger rate is around 3 Hz.

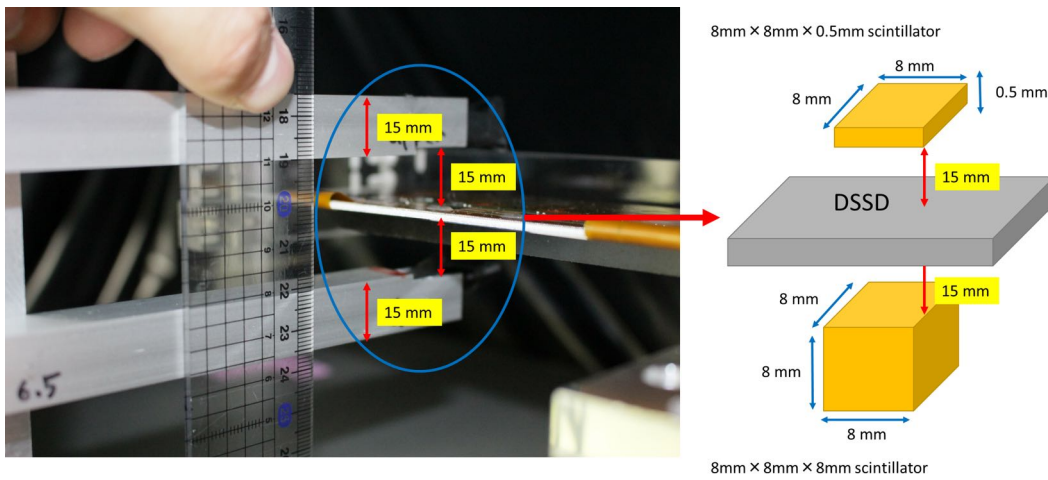


Figure 8.6: Geometry of the arms.

8.2 Method of β -ray Source Scan

To confirm whether assembled ladder is acceptable for the experiment, first of all we check whether we can detect the signals in various places of the DSSD.

For checking the quality of all channels, we considered that to hit all channels with the β -ray source is better way. In order to perform such a way, we move the β -ray source diagonally with the data-taking (like Fig. 8.7) after the ladder assembly. In this way, we can hit all channels by the β -ray source effectively.

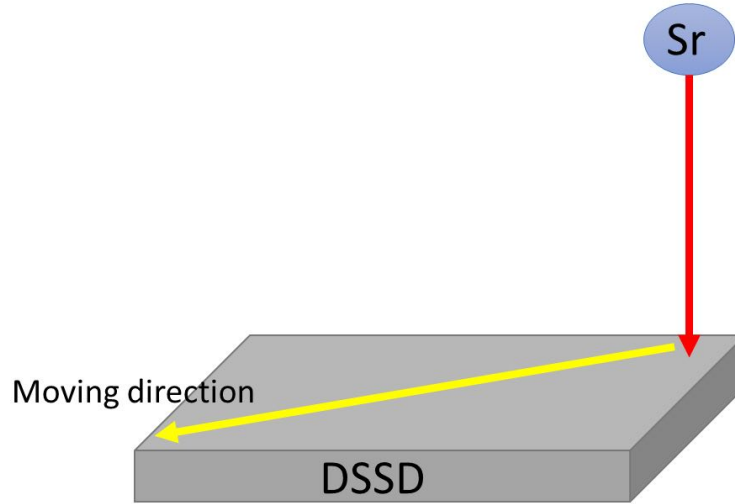


Figure 8.7: Moving direction. The inner structure of DSSD is crossed semiconductor strips. When we scan by source with moving as this picture, we can hit all channels with β -ray source.

This way seems to have no problem, however there is problem in the scan of a slant DSSD. For the slant DSSD part, it is difficult to scan by this setup because if we move this stage to the slant part, the arm of stage hit the slant DSSD. This is dangerous not only electrically but also mechanically. To prevent the ladder from this problem, safe way of scanning the slant DSSD is now on discussing.

We now have the method to scan four DSSDs on the ladder except slant DSSD.

8.3 Run mode of APVDAQ in the β -ray source test

In the section of APVDAQ, we saw there are some run modes. For the measurement with β -ray source test, “Hardware Run” of APVDAQ and six sampling mode are used as the method of data-taking. Consecutive six samples taken every 25 nsec are taken by this run mode and sampled data is used to fit by the exponential function for calculating the parameters.

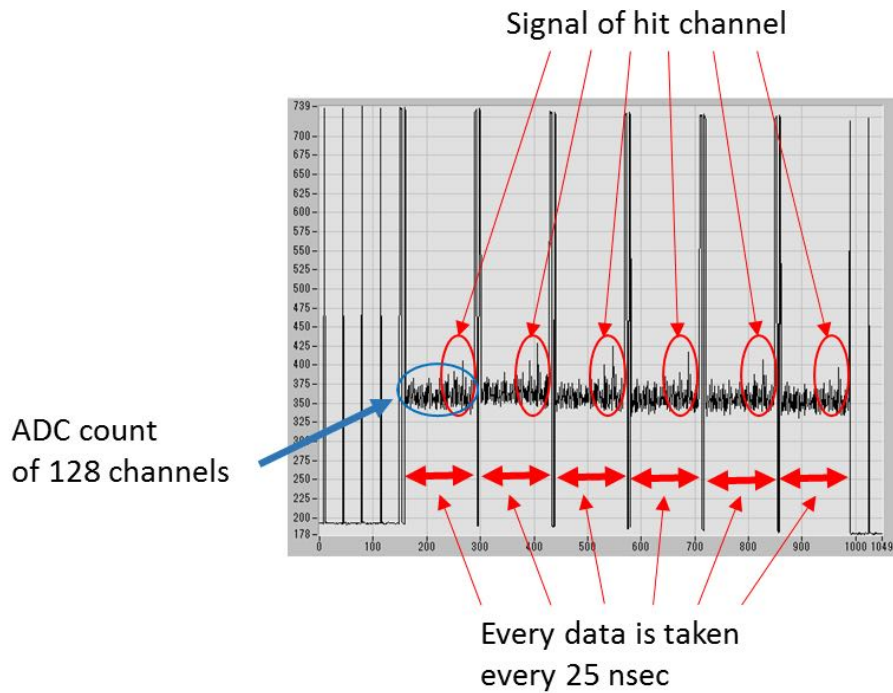


Figure 8.8: Signal in 6-sampling mode displayed by the APVDAQ. When there is a trigger, then the consecutive six samples are taken with the interval of 25 nsec and signal is seen as the spike. Each sample of this 6 wave means a raw ADC count of 128 channels. On the other hand, if there is no trigger, only sink pulses are output continuously (its frequency is 40 MHz in APV25) as shown in the left side of this display.

Only three samples near the peak are used for the fitting as the image shown in Fig. 8.9.

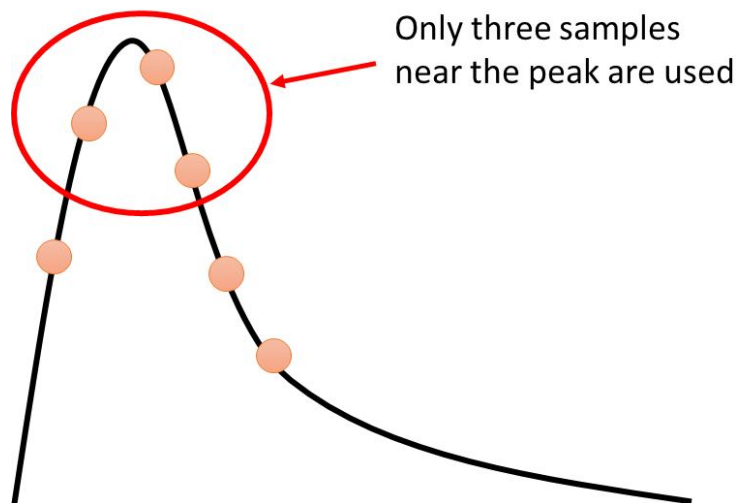


Figure 8.9: Image of the sampled six points. This is not real data. Only three samples of six are used.

8.4 Fitting Method

Ideal shaping form of CR-RC shaper is considered to be the exponential function if we assume Dirac delta function as the input.

$$f(t) = A \frac{t - t_{peak} + \tau}{\tau} \exp\left(-\frac{t - t_{peak} + \tau}{\tau}\right) \quad (8.1)$$

here t_{peak} is a peaking time, τ is a shaping time, and A is a constant. Maximum height of this function is A/e (e is a number of Napier thus $e = 2.71828\dots$) when $t = t_{peak}$. Thanks to the multi-peak mode of APV25 we can apply this fitting method by using the sampled data and also can know the peaking time and fitted pulse height. As mentioned in the section of APV25, it allows us to take consecutive samples of the shaper output signal; each sample is taken every 25 nsec. This multiple-peak mode will be used in Belle II SVD readout chain. Three samples near the peak are used for fitting and this enables us to know the hit timing.

For the calculation of each parameter, following formulae are used. Substituted parameter A_i ($i = 1 \sim 6$) are the sample taken by multi-peak mode (6 sample mode), d is an interval of the sampling thus $d = 25$ nsec

$$t_{peak} = -d \sqrt{\frac{A_N^2}{A_N^2 - A_{N-1}A_{N+1}}} - \frac{d}{\log \frac{A_{N+1}}{A_N} \frac{\sqrt{\frac{A_N^2}{A_N^2 - A_{N-1}A_{N+1}}}}{\sqrt{\frac{A_N^2}{A_N^2 - A_{N-1}A_{N+1}} + 1}}} \quad (8.2)$$

$$\tau = -\frac{d}{\log \frac{A_{N+1}}{A_N} \frac{\sqrt{\frac{A_N^2}{A_N^2 - A_{N-1}A_{N+1}}}}{\sqrt{\frac{A_N^2}{A_N^2 - A_{N-1}A_{N+1}} + 1}}} \quad (8.3)$$

$$A = \frac{A_N}{\frac{d}{\tau} \sqrt{\frac{A_N^2}{A_N^2 - A_{N-1}A_{N+1}}} \exp\left(-\frac{d}{\tau} \sqrt{\frac{A_N^2}{A_N^2 - A_{N-1}A_{N+1}}}\right)} \quad (8.4)$$

Here, A_N (ADC count) is the maximum value in six samples. Then we calculate the signal by using the maximum pulse height $Signal = A/e$ (ADC count) and the calibration constant explained in Chapter. 3. The signal is therefore written

$$Signal \text{ (electrons)} = \frac{A}{e} \times \frac{\text{Charge of calibration pulse (22400 electrons)}}{\text{Pulse height of calibration curve (ADC count)}} \quad (8.5)$$

8.5 Property of Tested Module

In this section, we show the result of β -ray source test. For this test we used assembled class-D ladder. As mentioned in Chapter. 5, only one DSSD in this ladder is readable. Thus, we see the result of only one DSSD in this section.

8.6 Cluster signal to noise ratio

In Chapter. 6, we used SNR as the ratio of the pulse height of calibration curve to the noise. However from this section, we redefine the SNR . We define two $SNRs$, SNR and cluster SNR . SNR is defined as $SNR = Signal \text{ (ADC count)} / Noise \text{ (ADC count)}$ and this is calculated for

all channels. The definition of this noise is the same as previous one. Cluster SNR is defined as follows; this is only calculated when there is the hit event.

$$\text{Cluster } SNR = \frac{\text{Total cluster charge}}{\text{Cluster noise}} \quad (8.6)$$

Here we defined cluster noise as 8.7, index i means hit and all clustered channels (, which is explained in Chapter. 8.8). ENC_i means an equivalent noise charge for channel i but here we assume that all channels in one side (p or n side) have the same ENC and we use averaged ENC ($= ENC_{\text{average}}$) obtained by Gaussian fit shown in Fig. 8.10. Then finally we obtain cluster noise by using a cluster size ($= N_{\text{cluster size}}$) as follows

$$\text{Cluster noise} = \sqrt{\sum_i ENC_i^2} \approx \sqrt{N_{\text{cluster size}}} \times ENC_{\text{average}} \quad (8.7)$$

Here, index i means for clustered channels. The SNR is therefore written as following formulae.

$$\text{Cluster } SNR = \frac{\sum_i Q_i}{\sqrt{N_{\text{cluster size}}} \times ENC_{\text{average}}} \quad (8.8)$$

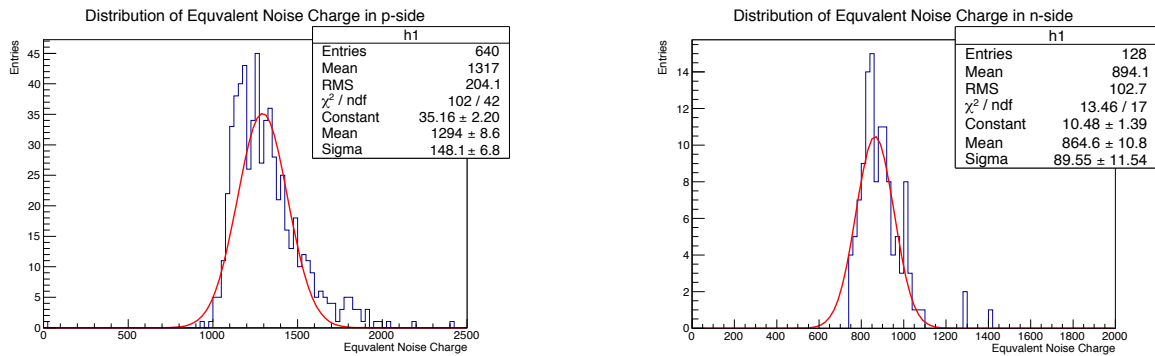


Figure 8.10: Distribution of equivalent noise charge in p and n side. Left is for p-side and right is for n-side. In our analysis, we used averaged ENC by gaussian fitting for calculating the cluster noise. The number of entries comes from the number of channel. However there are totally four APV25 chips in n-side, we only used only one APV25 chip because of the existence of the noisy channels in other APV25 chips.

After this section, we use SNR and cluster SNR .

8.7 Estimated capacitance

The ENC in the APV25 is described by $ENC(e) = 246 + 36/\text{pF}$ and thus increased by the capacitance of the signal line and the DSSD. Applying this formula for the obtained result of ENC in both p and n sides, estimated ENC in both sides in this module are 1294 e for p-side strip and 864 e for n-side strip as shown in Fig 8.10, the estimated capacitances therefore are calculated as

$$\text{p side capacitance} \sim 29 \text{ pF} \quad (8.9)$$

$$\text{n side capacitance} \sim 17 \text{ pF} \quad (8.10)$$

This capacitance includes the capacitance of the PA.

8.8 Cluster finding condition

The target of this analysis is to evaluate the performance of assembled ladder. First we find the hit event to reconstruct the hit position, hit timing, and cluster charge and so on for measuring the performance of assembled ladder. Analysis method is as below,

- Perform the CMC for all channel by subtracting the CMS. We chose only healthy strips (*noise* < 10 with the bias voltage) for the CMS calculation.
- Find the hit strip which satisfy $SNR > 5$
- Three ADC samples near the peak of the hit channel must satisfy “ $SNR > 3$ ”
- Search the strip which satisfy $SNR > 3$ (we define this strip as “clustered channel”) near the hit strip. If the number of hit strip is N , we search the clustered channel in $N-3 \sim N+3$.
- Define the cluster size as number of hit strip (one) + clustered channel

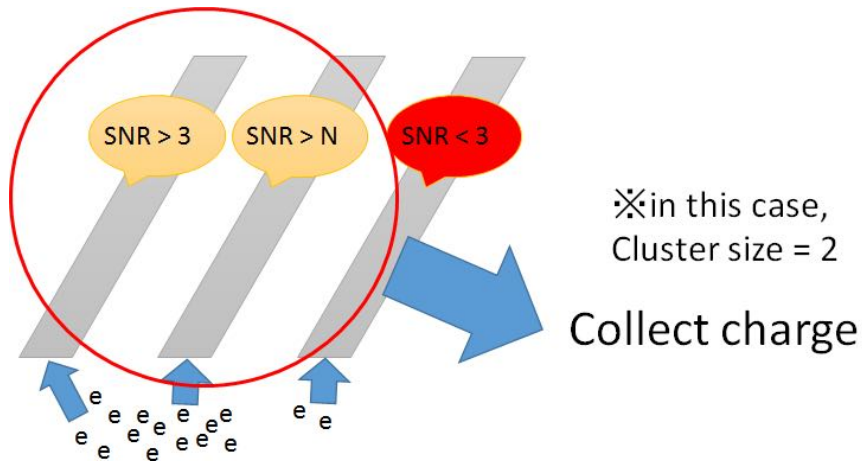


Figure 8.11: Image of a clustering. First we search a strip which satisfies $SNR > 5 = N$ (hit strip) and search the strips satisfy $SNR > 3$ near the hit strip. This image shows when cluster size = 2. Then we collect the charge from these clustered channels.

- Define the hit position as the center of mass of the charge like this.

$$\text{hit position} = \frac{\sum_i x_i Q_i}{\sum_i Q_i} \quad (8.11)$$

Index i means for clustered channels.

- Only when there are hits in both sides p and n side, clustering is performed.

8.9 Result of analysis

Following picture is the result of analysis in the source test. In this analysis, we fixed the position of β -ray source near the region of channel 400 - 768 in p-side and channel 100 - 260 in n-side. First cluster position becomes as shown in Figs. 8.12, 8.13.

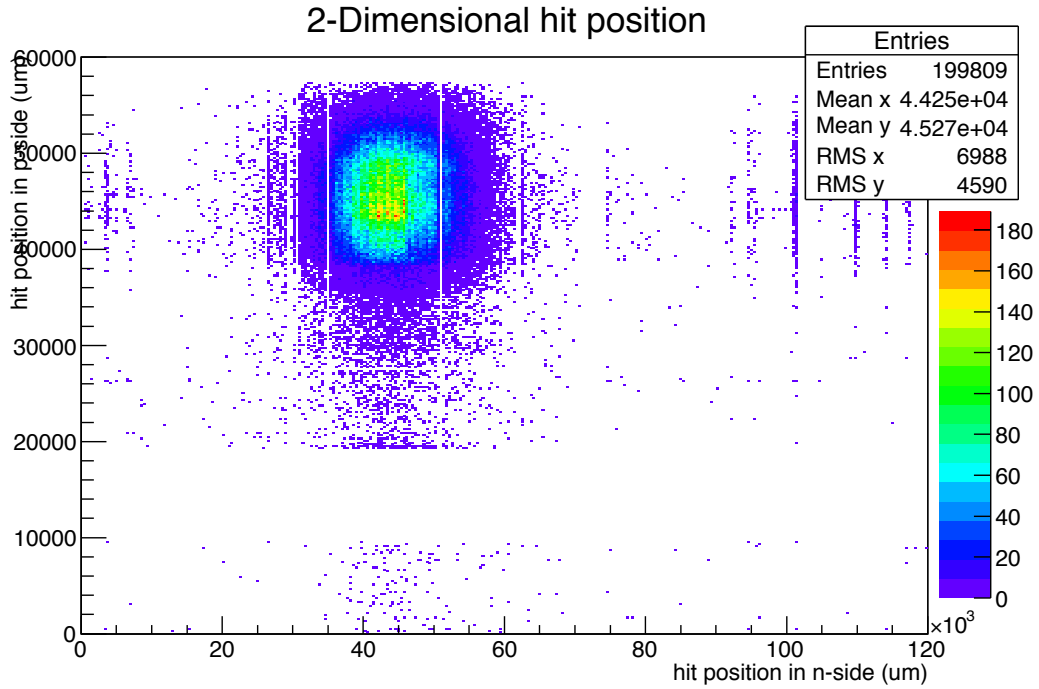


Figure 8.12: Hit map on the DSSD. Horizontal axis indicates n-side and vertical axis indicates p-side. Unit of the length is μm .

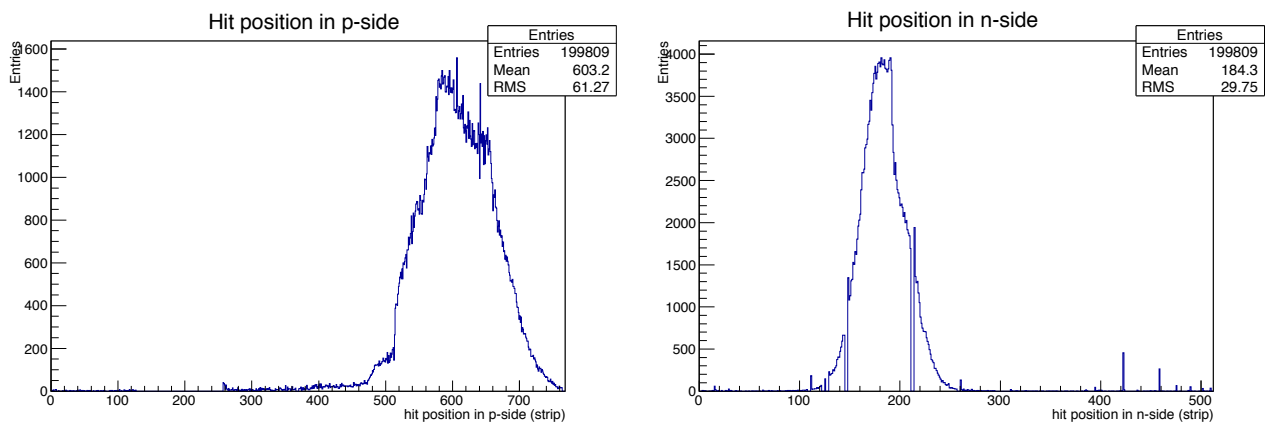


Figure 8.13: Distribution of a clustered position. Right is for n-side and left is for p-side.

This hit position is consistent with the position of the β -ray source. However, there are structures in the hit-map of p-side. If the position of β -ray source is fixed, then the distribution of the hit would be like a Gaussian. We inspected the cause of this non-uniform structure, then

we found that this non-uniform structure is caused by the structure of the ladder. Also we found that there is the rib in the position of β -ray source and this position is consistent with the position of non-uniform structure shown in Fig. 8.13. To confirm whether our assumption is correct or not, we took the data when ^{90}Sr source is put between two ribs as shown in Fig. 8.14. In this position, the distribution shows Gaussian-like shape as shown in Fig. 8.15.

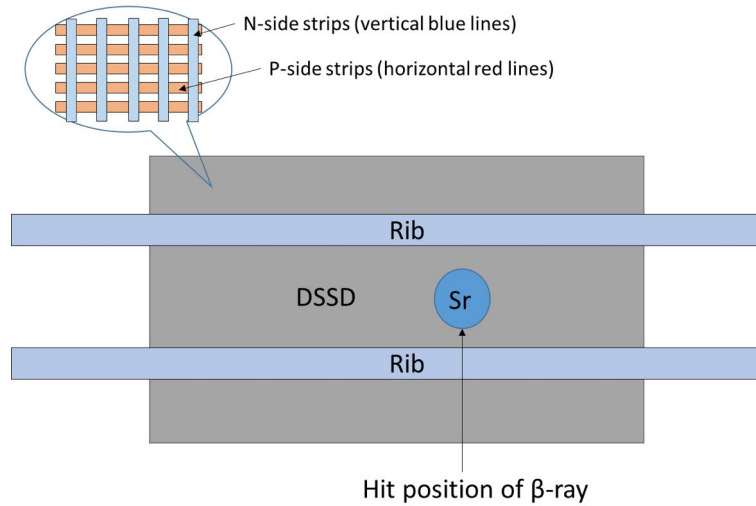


Figure 8.14: The position of β -ray source. We put the source between two ribs to confirm whether the ribs is the cause of non-uniform distribution.

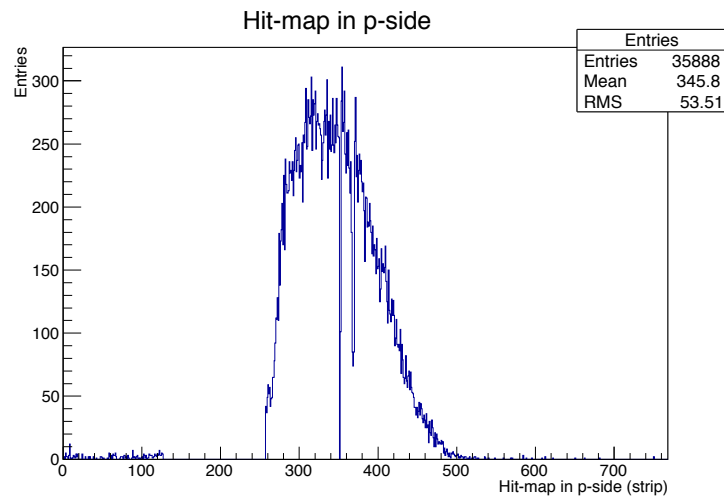


Figure 8.15: Hit map in p-side when we put the source between two ribs. Except the broken region channel 128 - 255, the distribution of hit shows Gaussian-like shape.

We therefore judged the structure shown in Fig. 8.13 is caused by the structure of ladder, not by broken channels.

Next cluster charge becomes as shown in Figs. 8.16, 8.17. In these results, the distribution of cluster charge is shown in each cluster size.

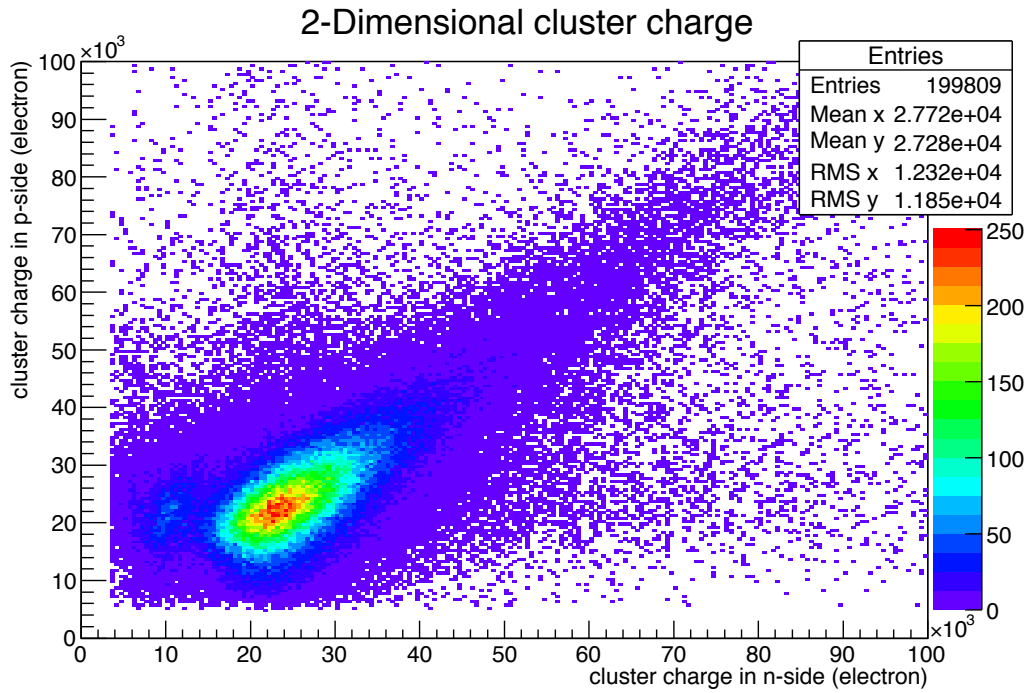


Figure 8.16: 2 dimensional cluster charge distribution. Horizontal axis indicates the cluster charge in n-side and vertical axis indicates the cluster charge in p-side. Unit of the cluster charge is electron.

cluster charge in p and n-side are shown in as following figures. Depending on the cluster size, the cluster charge is different. In n-side, the distribution of cluster charge in case of cluster size = 1 has two peaks. We will discuss this two peaks why there is small peak in n-side.

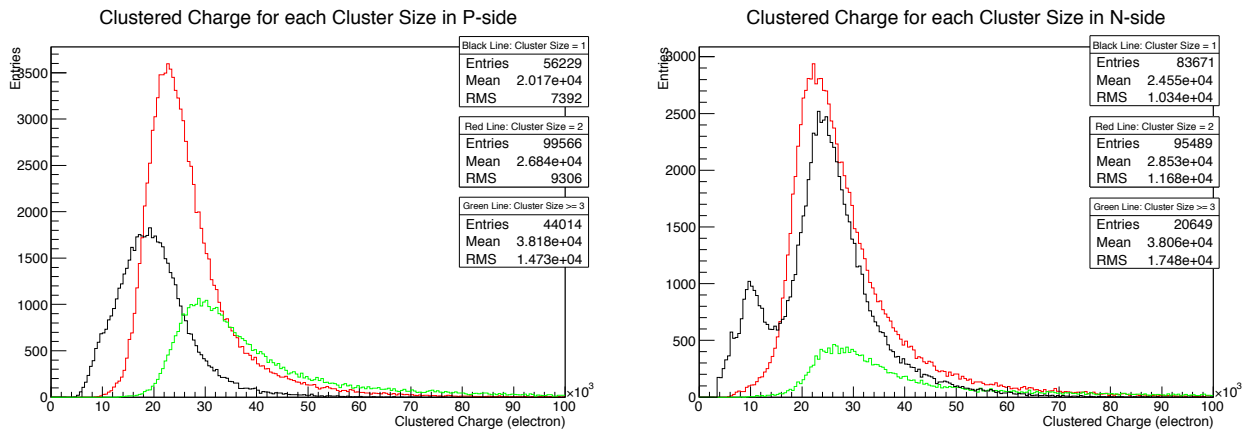


Figure 8.17: Distribution of a cluster charge for each cluster size. Black one is cluster size = 1, red one is cluster size = 2, and green one is cluster size ≥ 3 . Left is for p-side and right is for n-side.

Integrating these results, we calculated the most probable 1 MIP charge by fitting with the Landau function. Result shows the estimated cluster charge of 1 MIP is about 21100 electrons

in p-side and 22600 electrons in n-side as shown in Fig 8.9. These are not bad result comparing to the measured value of the beam test at CERN in 2008 (~ 22000 e) by using the test module made by the group in Austria (, which is different from our assembled module.) [7].

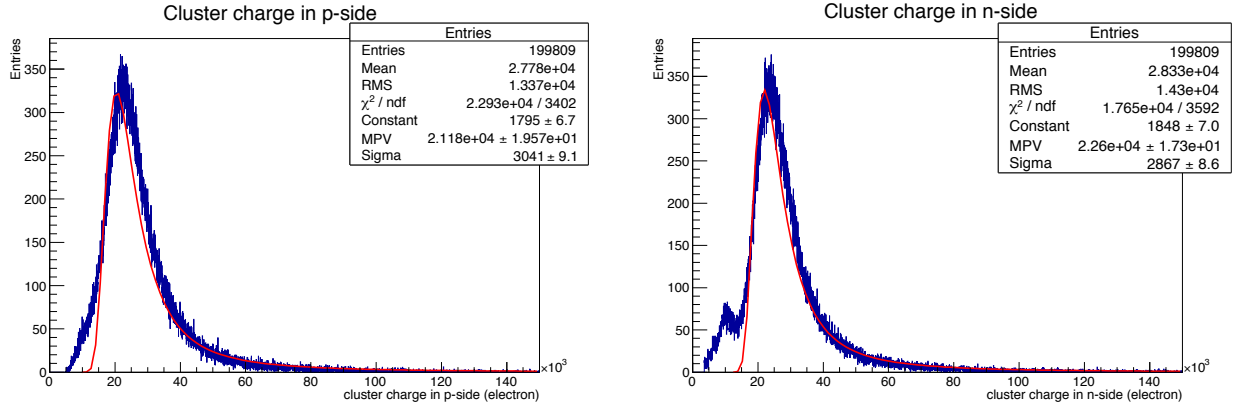


Figure 8.18: Distribution of cluster charge. Left is p-side and right is n-side. Red line is the Landau fitted curve.

There is small peak in a distribution of cluster charge in n-side when cluster size is 1 while there is no secondary peak in p-side. To consider the cause of this small peak in n-side, we first considered the differences between p and n-side.

Remembering the structure of the DSSD, in n-side, there are p-strips which prevents n-side strips from short connection. Also n-strip has wider pitch than p-strip (n-strip pitch is $240 \mu\text{m}$, p-strip pitch is $75 \mu\text{m}$). On the other hand in the distribution of cluster charge in p-side, there is no small peak and the distribution of cluster charge in each cluster size has only one peak, which is different from the situation in n-side.

To reveal the cause of this small peak, we considered the reasons as follows.

- 1. Charge is absorbed during the propagation in somewhere such as the p-strip in n-side.
- 2. Threshold of SNR of cluster channel is high. Then there are charges not collected because of the high threshold and that causes the small peak.
- 3. Low threshold of $SNR > 5$ of hit channel causes small peak. Because of this low threshold, some dummy hit events caused by noise are detected as the real hit events and involved in the calculation of the cluster charge. Then, this dummy events are appeared as the small peak.
- 4. Some noisy channels in n-side cause the small peak.

For the reason 1, there is no readout line on the p-stop strips between n-strips; there is no method to verify reason 1. However, we investigated the hit position dependence of the charge by using the Single-DSSD readable module (, not class-D ladder). We performed the laser scan to confirm whether our assumption is correct. The detail of this inspection is described in Appendix. A.7. If the p-strips between n-side strips absorb the charge, it is expected there is the position dependence of the charge. As the result shown in Appendix. A.7, there is the position dependence of the charge and there is the region where the collected charge is small. Also this position dependence appears with the interval of pitch width of n-strip ($= 240 \mu\text{m}$)

periodically. However, we cannot conclude that this reason 1 is the cause of the small peak of the cluster charge in n-side. Although we must explain why the small peak of cluster charge in n-side shows the peak at around 10000 electrons, we cannot explain this point. There is certainly the possibility that p-strips in n-side absorb the charge, however, we cannot explain the reason of the value 10000 electrons of the small peak.

To confirm whether reason 2 is the cause of small peak in n-side, we tried to change the threshold of SNR of cluster channel. We set this threshold to zero and we clustered the charge near the hit channel. The threshold of hit channel is invariant ($SNR > 5$). For the cluster in this case, we check whether four channels near the hit channel satisfy the condition $SNR > 0$ (This condition seems to be satisfied in every case. However when we subtract the CMS from the raw ADC count, $ADC < 0$ is possible). However there is still small peak in the distribution of cluster charge in n-side as shown in Fig. 8.19.

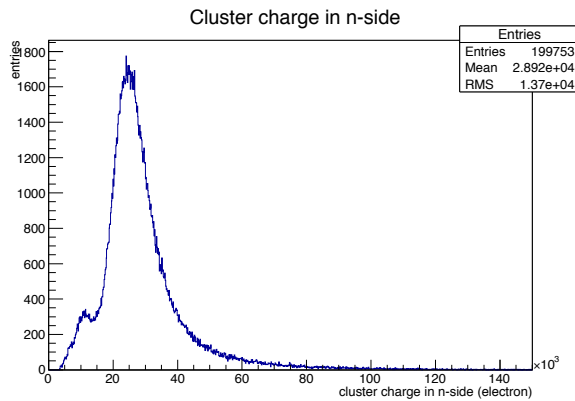


Figure 8.19: Distribution of cluster charge in n-side. We set the cluster width is 2; this means if we assume that hit channel is channel N, we collect the charge from channel N-2, N-1, N+1, N+2. Also we set the threshold of SNR is zero for cluster channel N-2, N-1, N+1, N+2.

Next, we confirmed the possibility of reason 3. Different from the case of reason 2, we set the threshold of cluster channel $SNR > 3$. Also we tried some patterns of the threshold of hit channel, $SNR > 6 \sim SNR > 20$. When we tried a case of $SNR > 15$, small peak in n-side has been disappeared as shown in Fig. 8.20.

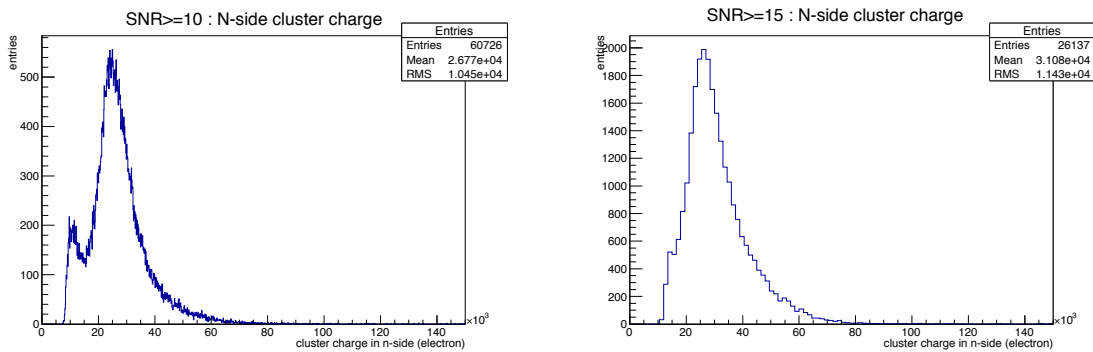


Figure 8.20: Distribution of cluster charge in n-side (cluster size = 1). Threshold of hit channel is $SNR \geq 10$ (left) and $SNR \geq 15$ (right).

As this result, we considered the small peak is caused when we use the events whose SNR is smaller than 15 and whose cluster size is 1.

Finally, to confirm whether reason 4 is the cause of small peak, we checked the hit-map in n-side with the condition cluster charge < 10000 electrons as shown in Fig. 8.21. In other words, we checked the position dependence of small peak. As the result shown in Fig. 8.21, there is peak in the region strip 170 - 200 where we put the β -ray source on it. This means the small peak is appeared in readable region, not in certain places.

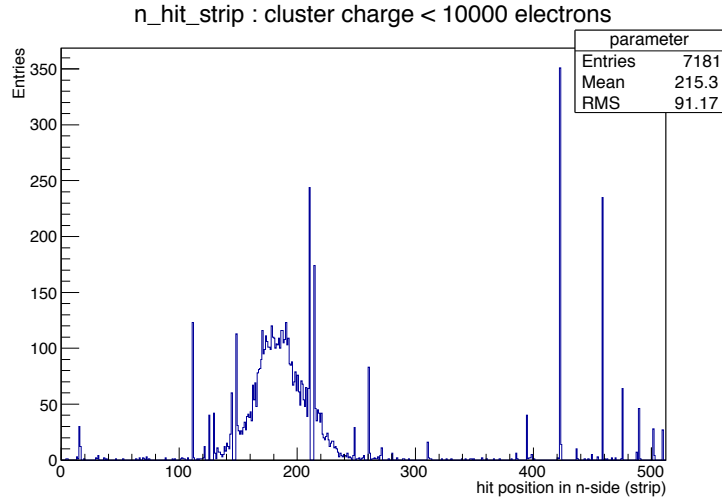


Figure 8.21: Hit-map in n-side with the condition cluster charge < 10000.

From the result shown above, we conclude following things.

- What we know:
 - There is the region where the collected charge is small in n-side and such a region appears periodically.
 - The small peak in n-side is caused by the low SNR threshold of hit channel.
 - The small cluster charge (< 10000 electrons) is also appeared in the readable region.
- What we do not know:
 - The reason why the value of small peak of cluster charge in n-side show around 10000 electrons

We therefore considered this small peak is not the phenomena of broken strips; if the small peak is caused by some noisy channels or broken channels, the position dependence of small cluster charge (< 10000 electrons) shows the peak only in unhealthy (broken or noisy) region. However, the peak of that position dependence is appeared also in readable region. From these studies, we concluded that this small peak is the normal phenomena in n-side. The small peak is appeared only when the cluster size = 1 in n-side while p-side has no small peak.

We discussed about the small peak of cluster charge in n-side for a long time. From next page, we go back to the discussion of the result of analysis. In the next page, we show the distribution of the cluster SNR in p and n-side. Results are shown in Figs. 8.22, 8.23.

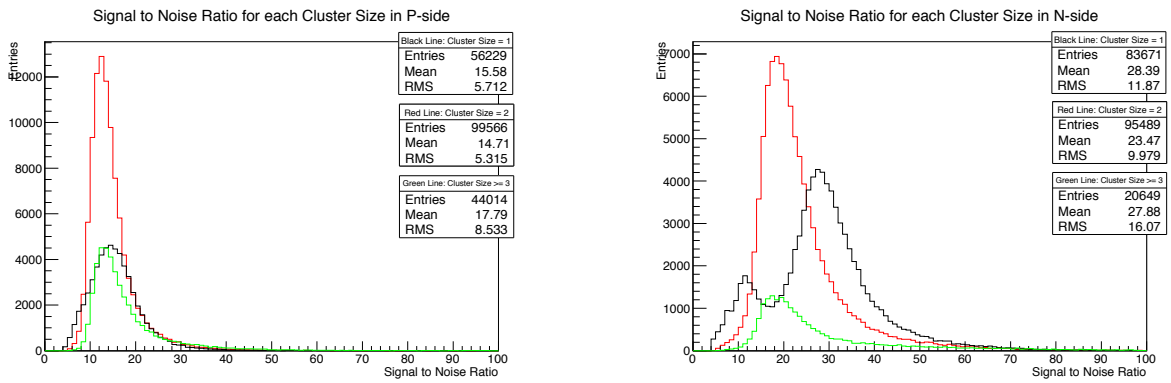


Figure 8.22: Distribution of a cluster signal to noise ratio for each cluster size. Left is for p-side and right is for n-side. Black one is cluster size = 1, red one is cluster size = 2, and green one is cluster size ≥ 3 .

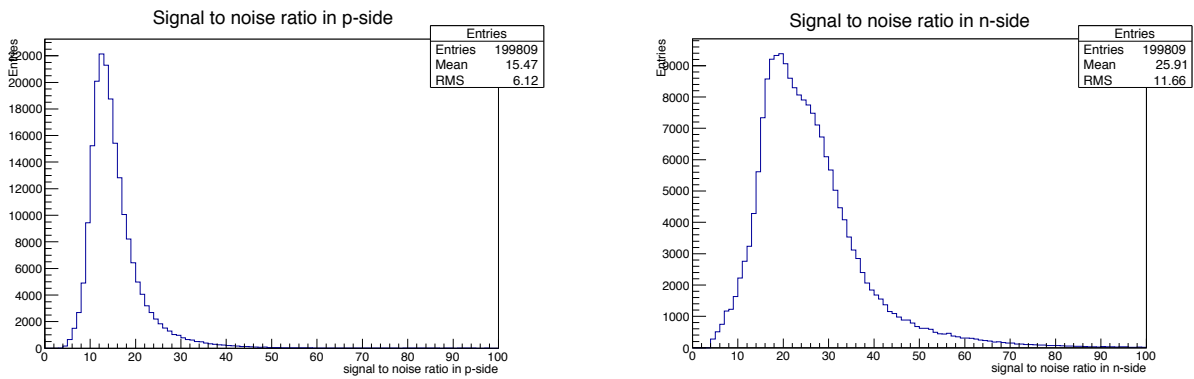


Figure 8.23: Distribution of a cluster signal to noise ratio in p and n-side.

In both side p and n side, the most probable SNR is more than 10. SNR in n-side is higher than p-side, this is because of differences of capacitance between p-strip and n-strip; p-strip has more length than n-side and the noise is larger in p-side, this makes the differences of the SNR .

Next histograms shown in Fig. 8.24 are the cluster size of p and n-side.

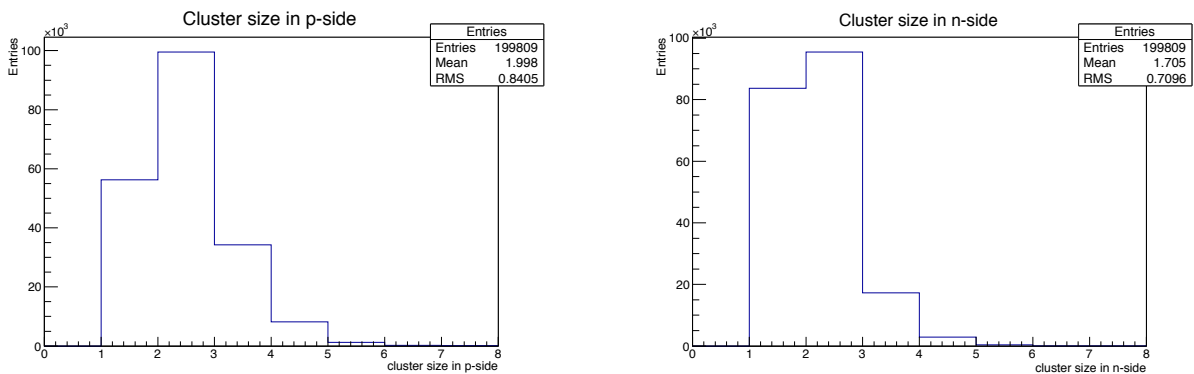


Figure 8.24: Distribution of a cluster size. Left is for p-side and right is for n-side.

Because of the differences the pitch between p and n-strip, the cluster size tend to be larger in p-side than that of n-side. In both side p and n, the most probable cluster size is 2 in our setup. This is consistent result in our setup. In this source test, all the charged particles penetrate the DSSD enter vertically. Thus, the most cluster size is 2; this most probable cluster size 2 means many charged particles pass through between two strips and generated charges are collected by two strips.

8.10 Strip by Strip Quality Inspection

The purpose of “Whole Assembly Level EQA” is to check whether assembled ladder is acceptable or not, but also to check the quality of all channels. Thus also in this procedure, whether we can detect the bad channels or not is important. For achieving this procedure, we check the pulse height (ADC count) of each channel. In this section, we took the data with moving the stage as shown in Fig. 8.7. Following results show the distribution of pulse height for each channel.

To confirm whether the way of strip by strip quality inspection is possible or not, we tested five region on the DSSD by the source. The hit-map in this test is shown in Fig. 8.25. Result shown in Figs. 8.26, 8.27 only shows the pulse height of some channels, not all channels.

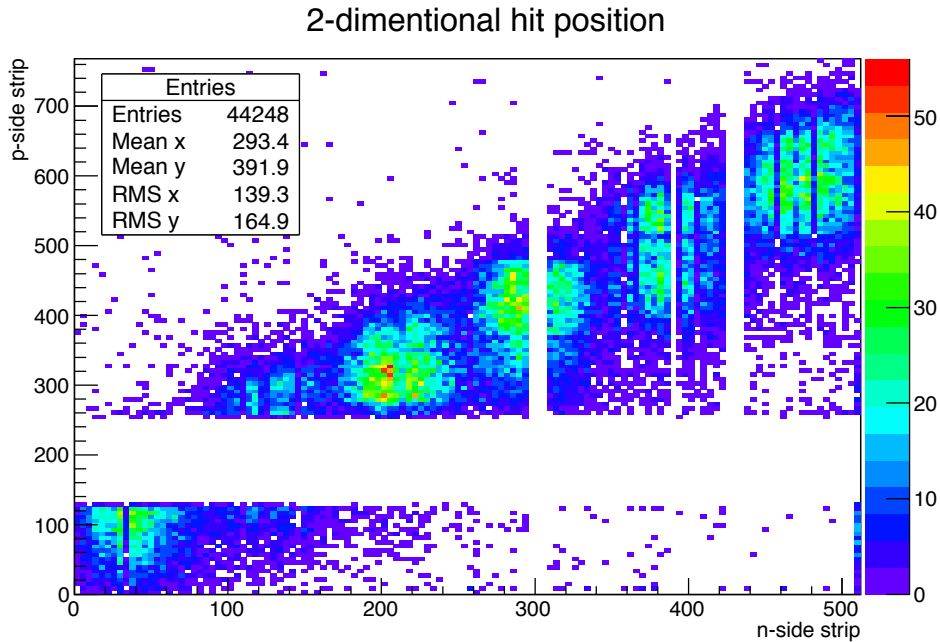


Figure 8.25: 2-dimensional hit-map. Channel 128 - 255 in p-side is broken region. There are five peak points where we put the β -ray source.

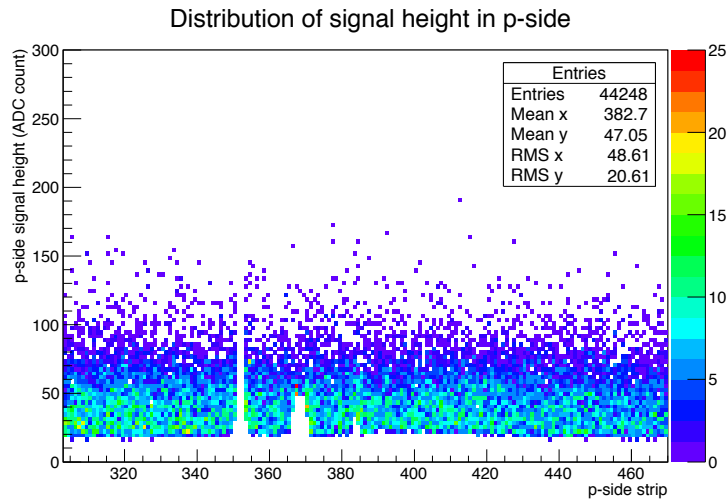


Figure 8.26: Distribution of pulse height in p-side. Horizontal axis indicates strip number in p-side. Vertical axis indicates the pulse height (ADC counts). This picture only shows region in channel 310 - 470.

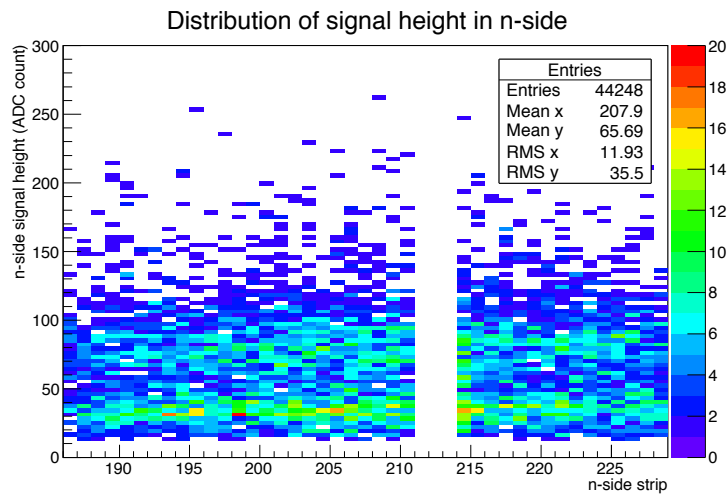


Figure 8.27: Distribution of pulse height in n-side. Horizontal axis indicates strip number in n-side. Vertical axis indicates the pulse height (ADC counts). This picture only shows region in channel 185 - 230.

From these results, there behaviors are categorized as next lists.

- Most probable behavior (Type I)
Showing the pulse height from low value to high value. This behavior is considered to be healthy.
- Showing only high pulse height (Type II)
There are some channels showing only high pulse height; for example in p-side, near channel 365. From the study in Single-DSSD readable module, these types of behavior

are considered to be caused by high noise channel or short-connected channel. Thus type II channels are categorized as bad channels.

- No entries (Type III)
There are some channels has no entries; for example near the channel 212 in n-side. From the study in the Single-DSSD readable module, this type III channels are considered to be short or open channel. Thus this type is also categorized as bad channels.

By using this information, we can know which channel is working, or which channel is non-working. We therefore can detect the bad channels by this β -ray source test. Through this study, we confirmed that this method is possible as the electrical quality inspection with the movable stage.

8.11 Conclusion in Whole Assembly Level EQA

From the result shown in Chapter. 8, we succeeded to read out the β -ray in the assembled readable module. Assembled module showed the most probable 1 MIP charge of about 21000 holes in p-side and 22600 electrons in n-side. Multiplying the energy to produce the electron-hole pair 3.6 eV by the obtained 1 MIP charge, we obtain the 1 MIP energy: 76 keV for p-side and 81 keV for n-side. We succeeded to demonstrate that we can evaluate the electrical performances of the assembled ladder, and this allows us to check the response of all channels in the DSSD.

However as mentioned in Chapter. 8.2, the way how to evaluate the performance of slant DSSD is now on discussing. After establishing this method, whole EQA procedures will be completely established. Except such a problem, all of our EQA procedures are established, but also these procedures are demonstrated by direct experiment. Summarized result is shown in Table. 7.

Table 7: Class-D ladder : Summary of result in β -ray source test.

Side	p-side	n-side	unit
Most probable cluster charge	21000	22600	hole or electron
Mean SNR	15	26	no unit
Cluster size	1-3	1-3	strip
Measured 1 MIP energy	76	81	keV

9 Conclusion

For searching the clue for the phenomena beyond the SM, new physics, the Belle II experiment will play a crucial role in indirect search. For launching the Belle II, preparations of sub-detectors are now on going.

In this thesis, we mainly saw the SVD and its EQA procedures. We constructed EQA procedures for the purpose to assemble electrically working ladder which can hard up with the experiment. As the method of achieving this purpose, we constructed mainly three pattern EQA procedures; parts level EQA, assembly level EQA, and whole assembly level EQA.

The purpose of parts level EQA is to exclude broken components not to use it for a real ladder assembly. In parts level EQA, we mainly checked the quality of Origami flexes with the APV25 chips by the APVDAQ, and classified them into two classes. Through this procedure, we succeeded to exclude broken Origami flexes whose APV25 is broken.

Second, we established assembly level EQA, whose purpose is to trace the quality of the ladder and to determine whether we can proceed to the next assembly procedures. In this assembly level EQA, we mainly implement electrical inspections in each wire-bonding procedure. We succeeded to know the behavior of bad channels through the readable module assembly, this information is used to detect bad channels during the assembly. Furthermore this procedure also succeeded to detect the problem of broken line in the PA0 (See Appendix A).

Finally, to confirm whether the assembled ladder is acceptable for the experiment or not, whole assembly level EQA is implemented. We succeeded to evaluate the performances of the assembled ladder. Also we succeeded to implemented strip by strip quality inspection by using the movable stage with the β -ray source. By these procedures, we also succeeded to obtain the information of behavior of channels in this source test. All EQA procedures play the crucial roles in whole ladder assembly procedure. These EQA procedures are strongly supported by the APVDAQ.

However, there is one more important thing. Although the EQA procedures are established by through the readable module assembly, we need to pay not to miss the broken wire-bonds or not to cause the accident such as breaking the DSSD or other components of the ladder during the assembly. These things are also very important to assemble the electrically working ladder.

We must check carefully whether there is unusual channel, or some electrical problems during the EQA procedures. To avoid missing the problems, inspection by other members is useful. Inspection from only one person is dangerous because of his or her tiredness.

As the conclusion, we established whole EQA procedures, and also we succeeded to demonstrate whole EQA procedures; except the way to perform the β -ray source test for the slant DSSD parts. .

A Diagnosis of Noisy Region in Single-DSSD Readable Module

We saw the data of class-D ladder at first. In this section, we see the data of Single-DSSD readable module, and discuss the problems in this module.

Actually, we met the problems during the assembly of this module: we met a lot of noisy channels in n-side. We discuss why this noisy channels are caused in this section. First we see the data of this readable module when we finished whole wire-bondings procedures and with a bias voltage of ± 40 V. Next we see the cause of the problems in this module. Finally we see the behavior of some bad channels such as open and short.

A.1 Property of Assembled Single-DSSD Readable Module

The data shown in the next page are taken with a bias voltage (± 40 V) after whole wire-bonding procedures. In this section we see the result after whole wire-bonding procedures with the bias voltage. We first see the result of p-side, the after we see the result of n-side.

As mentioned in Chapter. 5, we used Origami flex whose one APV25 in p-side is broken. Channel 335-383 in p-side show unusual behavior because of broken APV25. First, calibration curves in p-side and its fitted height are shown in Figs. A.1 and A.2.

The raw noise in p-side is shown in Fig. A.3. Almost all channels show almost same raw noise as that of class-D ladder. The noise in p-side is shown in Fig. A.4. Result in p-side shows similar result to that of class-D ladder, however, situation is changed in n-side.

Next, we see the result of n-side. The calibration curves in n-side as shown in Fig. A.5. There are totally 512 curves. Distribution of pulse height is shown in Fig. A.6. However, there are many channels show unusual value in region of channel 0 - 40, 340 - 380, 420 - 512. Distribution of raw noise in n-side is as shown in Fig. A.7. Different from the result of class-D ladder, there are many high raw noise channels and these channels are consistent to the channels show unusual pulse height in Fig. A.6. The noise in n-side is shown in Fig. A.8. The situation is similar to the result of raw noise.

Results of p-side are similar that of class-D ladder except the broken APV25 region. On the other hand in n-side, there are many channels show high noise. During the assembly of Single-DSSD module, we could not specify the cause of these noisy channels. After the assembly, we investigated these noisy regions, and succeeded to specify the cause of that.

From next section, we see how we specified and the behavior of bad channels for the study of the EQA.

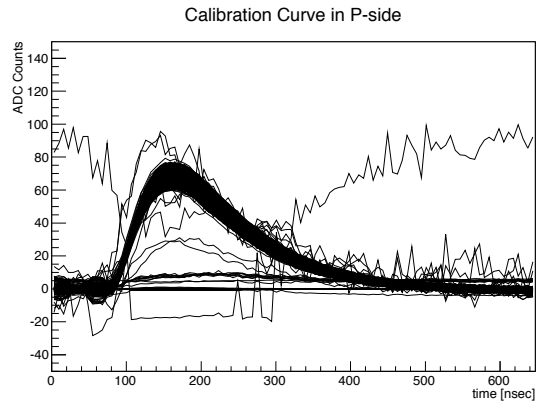


Figure A.1: Calibration curve in p-side.

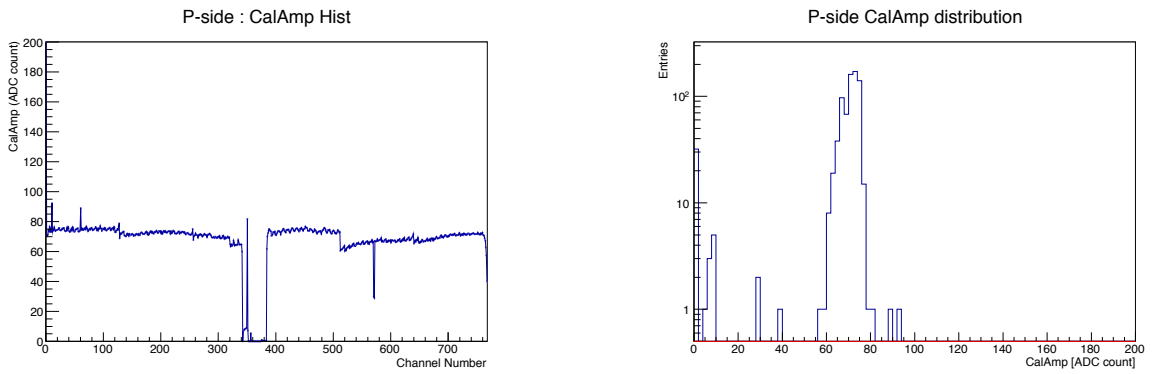


Figure A.2: Histogram of fitted pulse height in p-side.

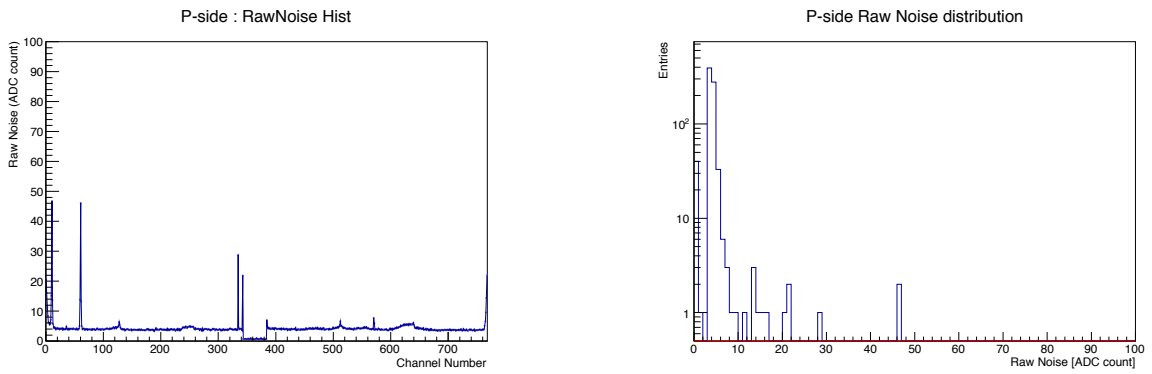


Figure A.3: Histogram of raw noise in p-side.

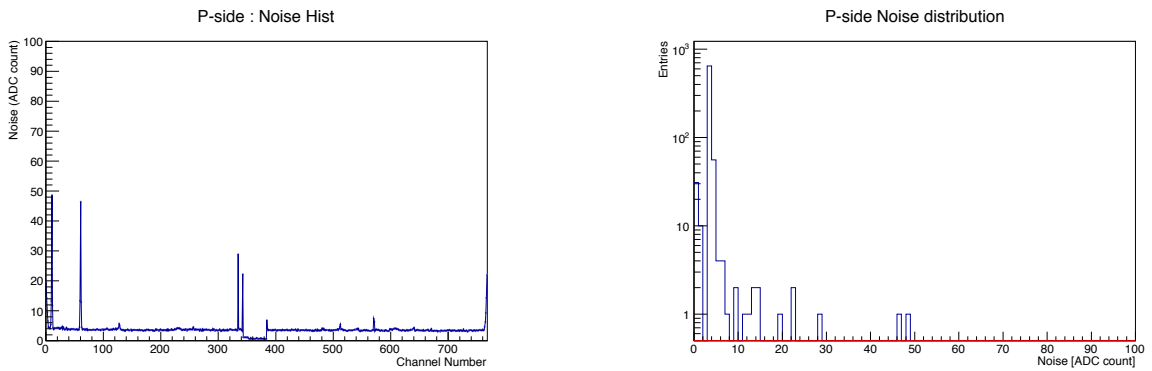


Figure A.4: Histogram of noise in p-side.

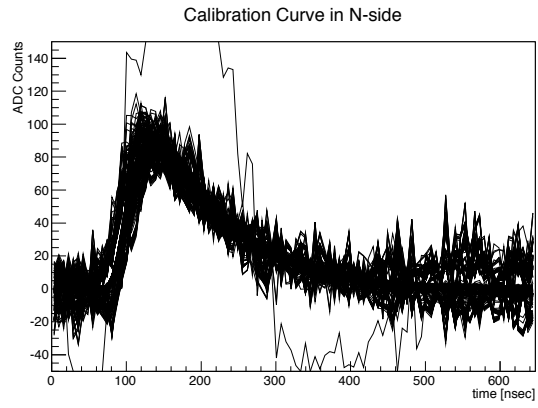


Figure A.5: Calibration curve in n-side.

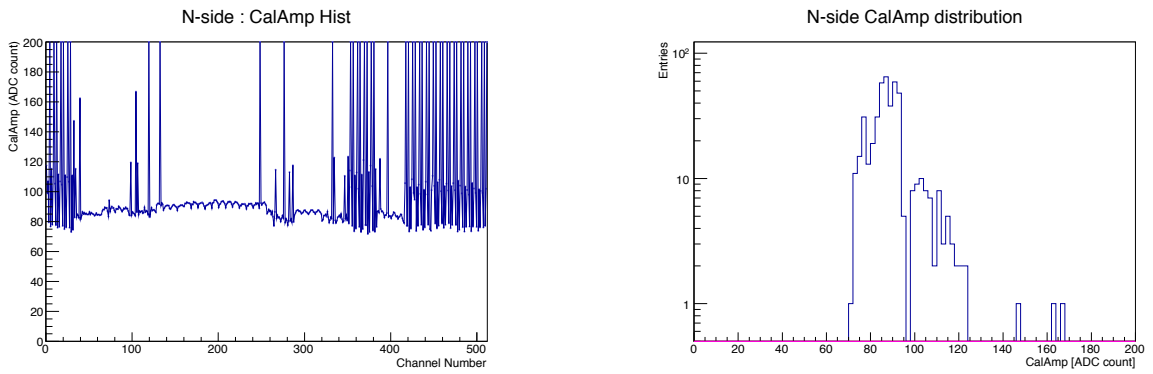


Figure A.6: Histogram of fitted pulse height in n-side.

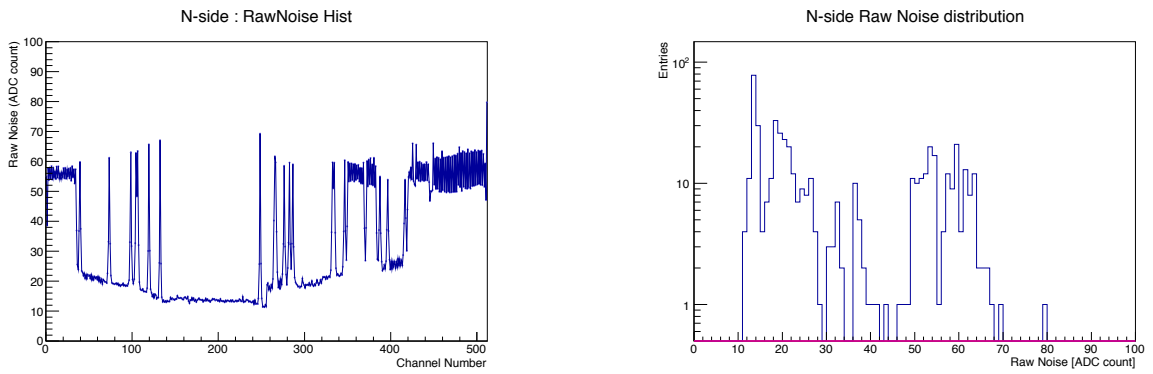


Figure A.7: Histogram of raw noise in n-side.

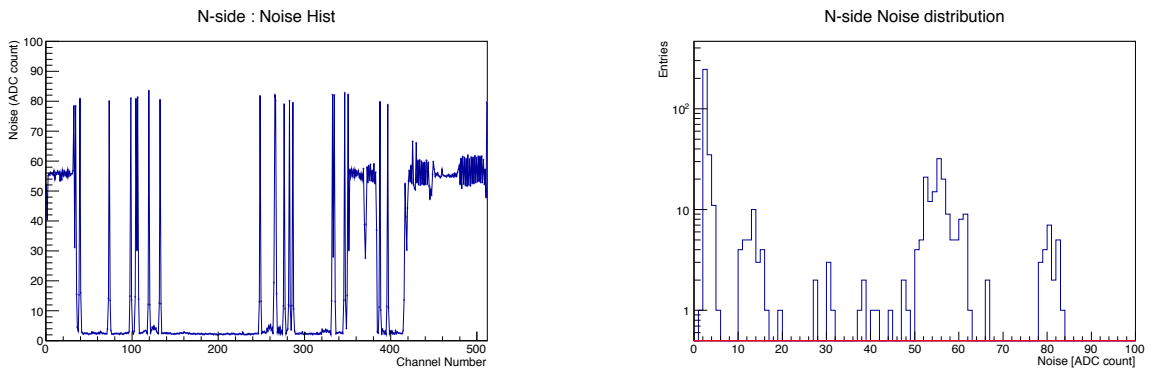


Figure A.8: Histogram of noise in n-side.

A.2 Inspection by laser scan

Purpose of laser scan is to confirm whether noisy channels can respond to the laser (Fig. A.9). We check whether the ADC count becomes higher when the laser is hitting on the strips. First we checked the response of the channel in noisy region and non-noisy region by laser scan. The wave length of the laser is about 850 nm, and spot size of the laser is less than 5 μm . By using its small spot size, channel by channel inspection is available.

We found there are many channels which did not respond to the laser and noisy channels correspond to that un-responded channels as shown in Fig. A.10. On the other hand, non-noisy channel responded to the laser.



Figure A.9: Laser scan for Single-DSSD module.

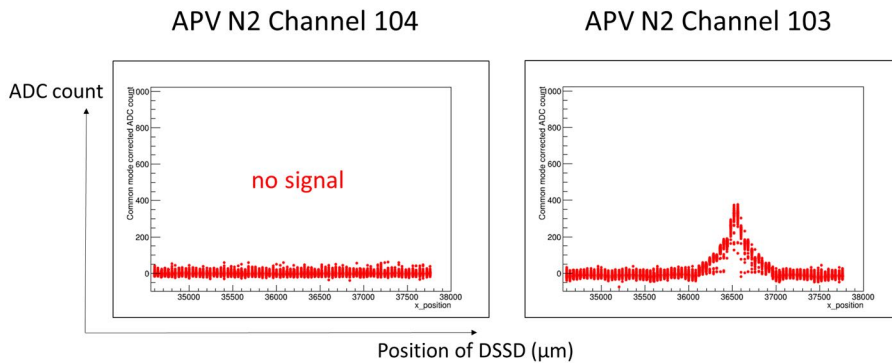


Figure A.10: Response to the laser in n-side APV8 (APV N2) before repair. Channel 104 does not show the signal from the laser.

We doubted noisy channel is open from the result of laser scan. To confirm whether our assumption is correct or not, we also implemented probe test for these channels to check the connection directly.

A.3 Inspection by Probe test

For detecting which component has problems, we checked the connection between APV25 - PA0 (APV25 side), PA0 (APV25 side) - PA0 (sensor side) and PA0 (sensor side) - DSSD by the probe test as shown in Fig. A.11. Result shows the problem in the connection between PA0 (APV25 side) - PA0 (sensor side); electrical connection was not confirmed. This indicates the existence of the broken line in the PA0.

Inspection of the PA0 by microscope shows that there is a crack near the bonding pad as shown in Fig. A.12. We checked all pad and found that crack is mainly exists in bottom pads of PA0. To make sure that crack is the cause of open, we checked the connection between the crack and confirmed there is no connection between the crack.

To study more, we tried to repair these cracks and took the data again to check its behavior.

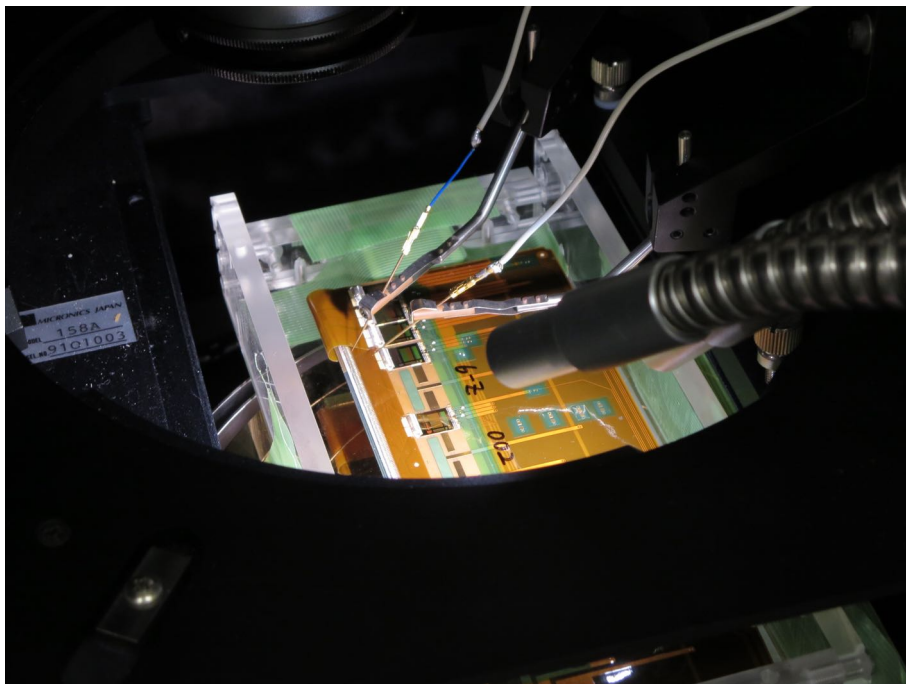


Figure A.11: Probe test for the Single-DSSD module.

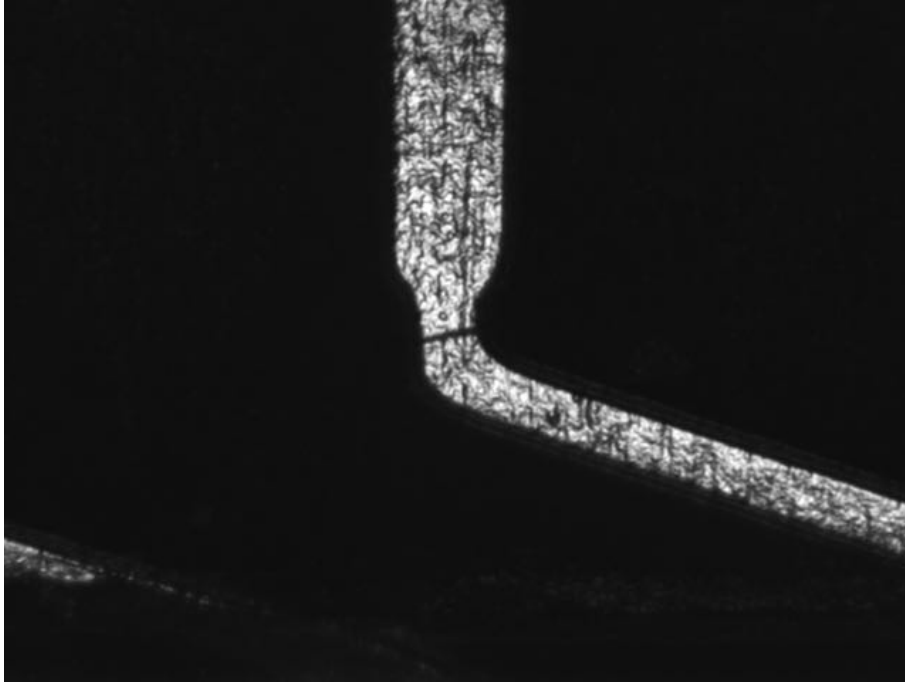


Figure A.12: Example of the cracks in the PA0. Especially many cracks exist in bottom line of PA0.

A.4 Repair crack

To repair the cracks, we tried to connect it by bonding foot like shown in Fig. A.13. Some cracks were repaired successfully, but some cracks were unrepaired; mainly two reasons are considered

- Bond-foot failed to connect
- Any other cracks exist not in near the bonding-pad where we cannot see

After repair, noisy channels are decreased as shown in Figs. A.14-A.15. Before the repair, not only open channel becomes noisy but also adjacent channels also become noisy. In our single module assembly, we confirmed the success rate of repair is about 70 percent. This is not sufficient for the electrically working ladder assembly. Our target is to connect more than 99 percent channels so this method of repair is not available in the real ladder assembly.

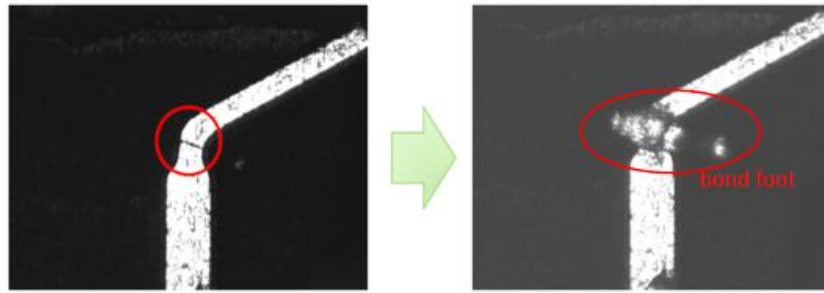


Figure A.13: Repair of the crack in PA0 by bond-foot.

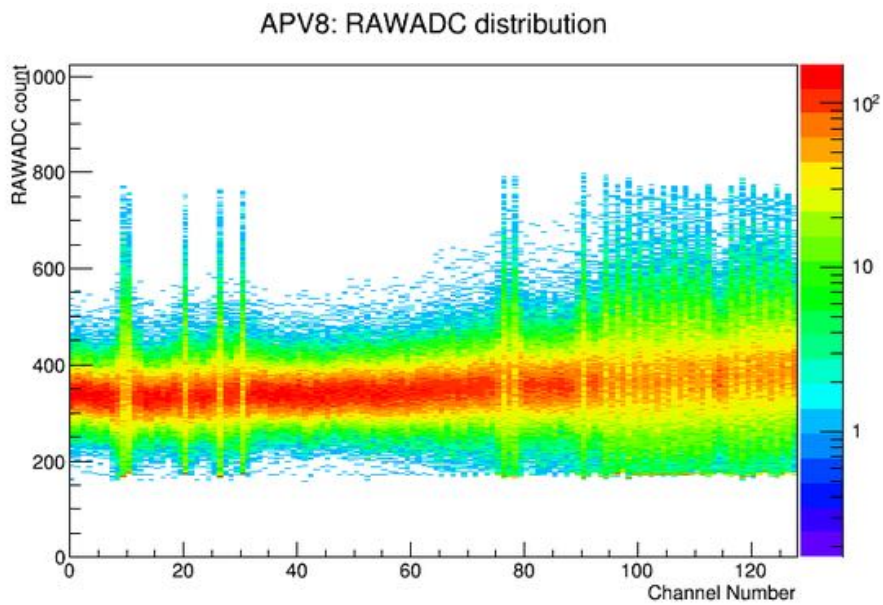


Figure A.14: Raw ADC distribution in n-side APV8 (APV N2) before repair by bond-foot. There are many noisy channels.

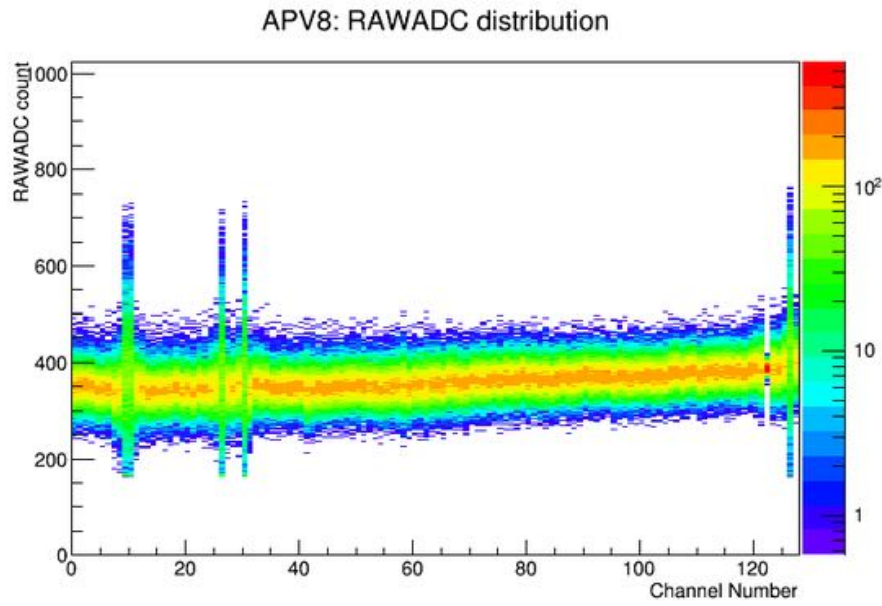


Figure A.15: Raw ADC distribution in n-side APV8 (APV N2) after repair by bond-foot. The number of noisy channel has been decreased, but there are still some noisy channels.

To confirm the conductivity of the repaired channels, we performed the laser scan again. Repaired channels changed its behavior as shown in Fig. A.16; these repaired channels responded, although these channels did not show the signal before repair.

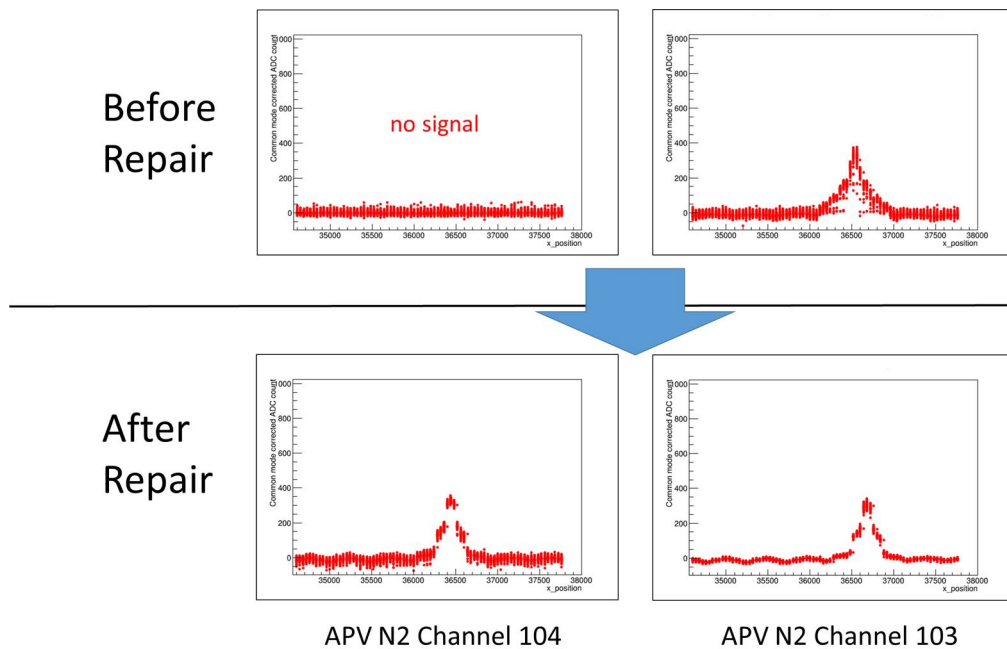


Figure A.16: Response to the laser in n-side APV8 (APV N2) before and after the repair by bond-foot. After the repair, channel shows the signal from the laser.

From this result, open channels show high noise, but also adjacent channels also show high noise. Also repaired open channels show relatively normal noise (around 10 ADC (w/o bias voltage)) and responded to the laser.

Also we confirmed that open channels show high pulse height as shown in Fig. A.17. There are two curves in this picture; red curve is the curve of open channel and black curve is the curve of good channel.

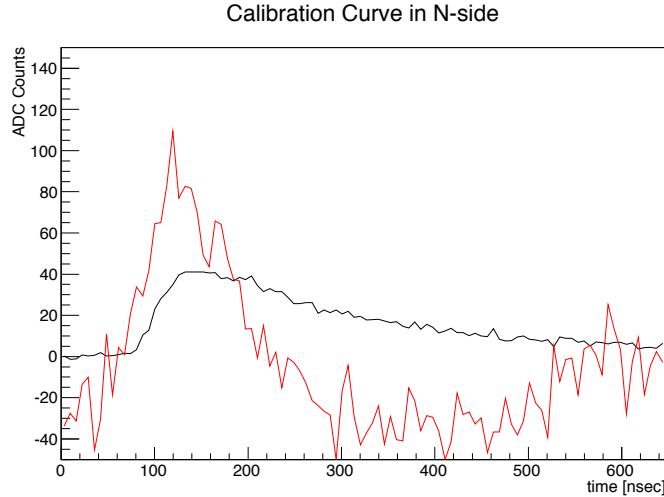


Figure A.17: Calibration curve of open channel and good channel. Red is open channel and black is good channel.

A.5 Inspection of Short Connection

We observed some channels show low pulse height during the assembly of Single-DSSD readable module. To confirm what is the cause of low pulse height, first of all we built up a following hypothesis.

- Low pulse height is caused by an increase of the capacitance: for example, by short connection. If a capacitance C becomes larger, output voltage V of channel is decreased if the total input charge of test pulse Q is invariant. Therefore output pulse height becomes lower from the formulae $CV = Q$.

To confirm this hypothesis, we made the short connections by wire-bonding like as shown in Fig. A.18 and compared the result measured before and after making the short. We made short connections between channel 45 - 46, 55 - 56, and 65 - 66 in APV N2 in the Single-DSSD readable module. Result shows the change of pulse height as shown in Fig. A.19. From this result, following things are observed.

- Low pulse height is caused by an increase of the capacitance such as short connections.
- Decreased level of the pulse height has some patterns
- Short-connected channels become noisy

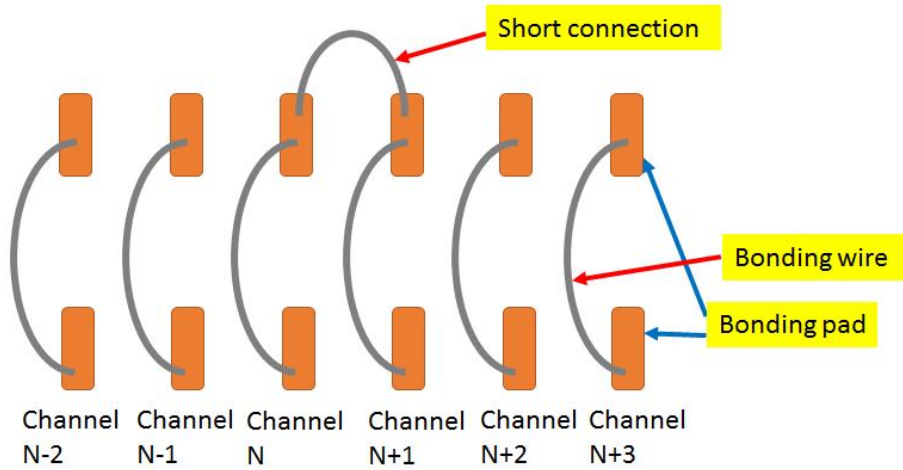


Figure A.18: Short connection performed by wire-bonding. In this picture channel N and N+1 are short-connected.

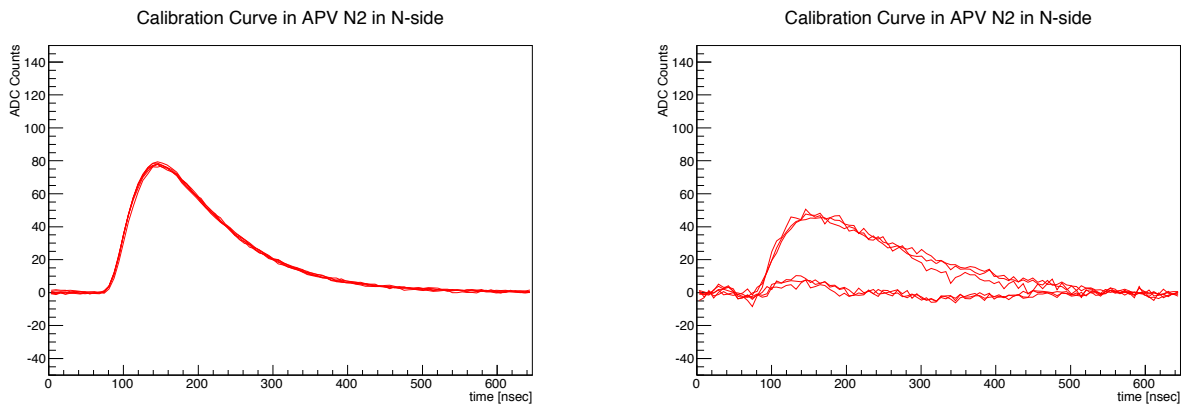


Figure A.19: Change of the calibration curves in six channels in N-side. There are totally six curves. Left is before performing the short and right is after performing the short. Pulse height becomes lower after performing the short.

A.6 Result from The Diagnosis

Following things are observed as the result of the diagnosis of the Single-DSSD modules.

- Open channel
This causes high noise, and makes adjacent channels noisy. Also open channel show high pulse height.
- Short channel
This causes low pulse height as shown in Fig. A.19. Also after performing the short-connection, short channel becomes noisier as shown in Fig. A.19.

Through procedures in this section, we succeeded to know the behavior of bad connected channels. Also in class-D ladder assembly, we confirmed that open channels and short channels show similar behavior as described in Chapter. 7.

A.7 Charge Distribution in the Laser Scan

Since we observed the small peak in the distribution of the cluster charge in n-side when cluster size = 1 in Chapter. 8, we doubted there is a hit position dependence of the cluster charge. In n-side, there are p-stops between two n-side strips to prevent the n-strips from the short connection. To investigate whether our assumption is correct, we performed laser scan to measure the hit position dependence of the charge. The setup is almost same as previous one. In this measurement, we hit the laser to the region of APV N2 channel 67-74 (strip 323 - 330). We moved the laser with the interval of $40 \mu\text{m}$ and we took 600 events in each point. Figure. A.20 shows the signal height in each position of the DSSD.

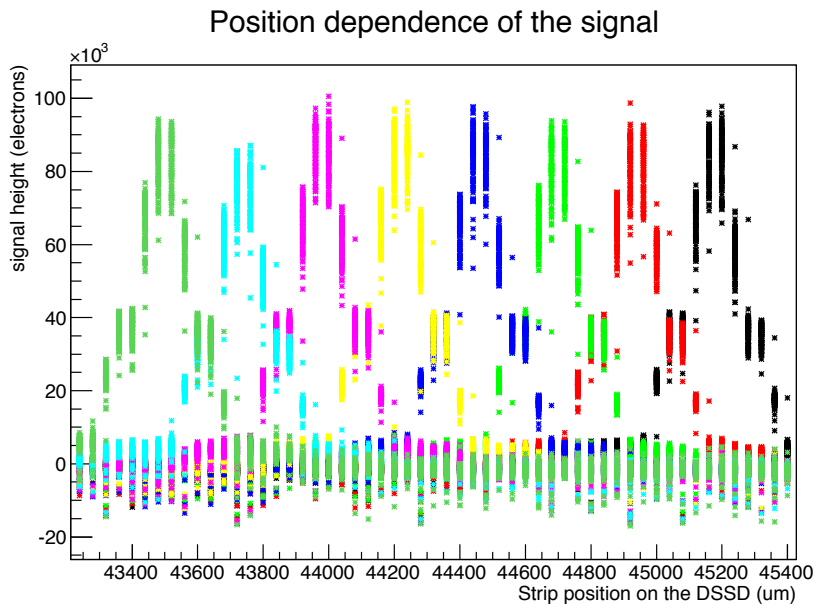


Figure A.20: Position dependence of the signal. This picture shows the response of eight channels and the signal of each channel is categorized by the color. Horizontal axis indicates the position of the DSSD where the laser is on it. Vertical axis indicates the signal height (electrons). The ordering of channel is APV N2 channel = 74, 73, ..., 68, 67 from left side.

As this result, there is the region where the signal of the channel is low; this region appears with the interval of $240 \mu\text{m}$, which is the pitch width in n-side. In the distribution of cluster charge in n-side, there is the small peak at around 10000 electrons when cluster size = 1. We also analyzed the data of laser scan. The cluster finding condition is almost the same as that of Chapter. 8; only the threshold of SNR of hit channel is different. In this analysis, we set this threshold of hit channel to $SNR > 3$. Figure. A.21 shows the cluster charge in n-side.

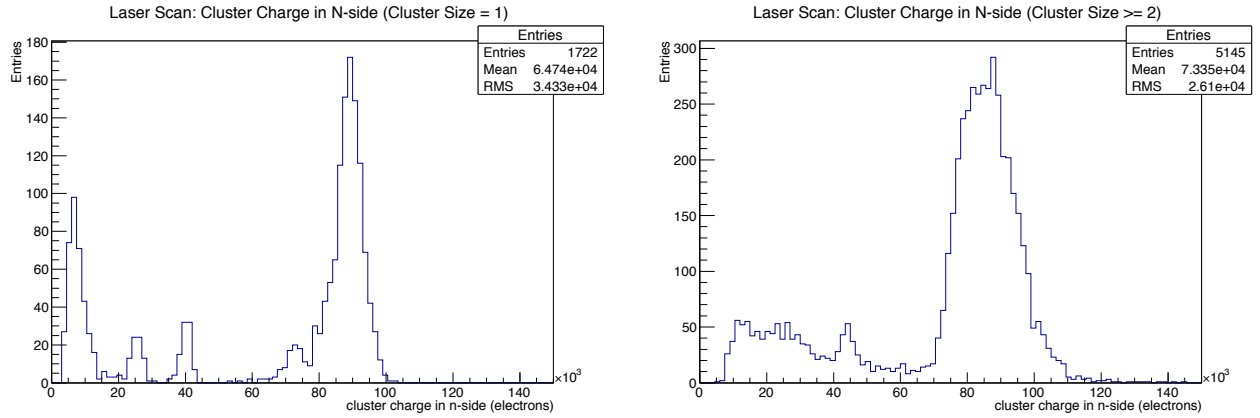


Figure A.21: Distribution of cluster charge in n-side. Left is when cluster size = 1 and right is when cluster size ≥ 2 .

When cluster size = 1, there is the small peak at around 10000 electrons while there is no such a peak when cluster size = 2. Also we investigated the laser position dependence of cluster charge when cluster size = 1 and cluster size ≥ 2 as shown in Fig. A.22.

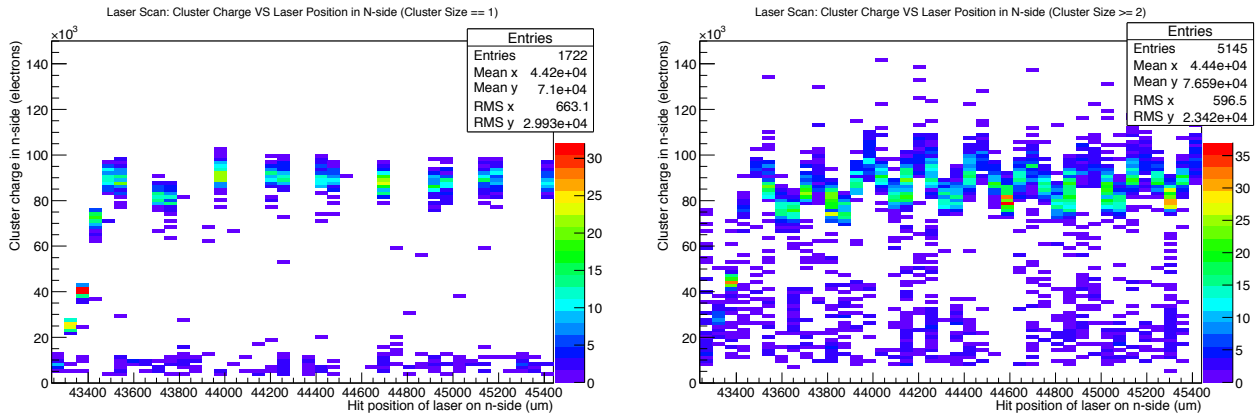


Figure A.22: The laser position dependence of cluster charge in n-side. Horizontal axis indicates the laser hit position in n-side (μm) and vertical axis indicates the cluster charge in n-side (electrons). Left is when cluster size = 1 and right is when cluster size ≥ 2 .

As this result, when cluster size = 1, there is the case when the small peak whose value is at around 10000 electrons. Although the laser and the β -ray are different, we observed that small peak in both cases when cluster size = 1 in n-side. Also as shown in Fig. A.22, there is the region where the cluster charge is low; this region appears when the laser is hitting between two n-strips. From these results, it is doubted the p-stops in n-side may absorb the charge. However, we still cannot conclude the cause of small peak. Because to show that the small peak is caused by the p-stops, we must investigate how much electrons are absorbed by the p-stops. In this discussion, we only discussed the laser position dependence of cluster charge to investigate whether there is the possibility that the p-stops absorb the charge.

B Result of β -ray source test in the Single-DSSD Readable Module

We also performed the β -ray source test for the Single-DSSD Readable Module. In this section, we only see the result of that. The analysis method is same as described in Chapter. 8.

First, Figs. B.1, B.2 show the cluster position. There are non-uniform structure around 40000 - 44000 μm in p-side. We confirmed that this is caused by the rib. Because of the weak radiation source we used, there are many particles stopped by the rib.

Different from the case of class-D ladder, cluster charge in p and n-side is smaller as we see in this section.

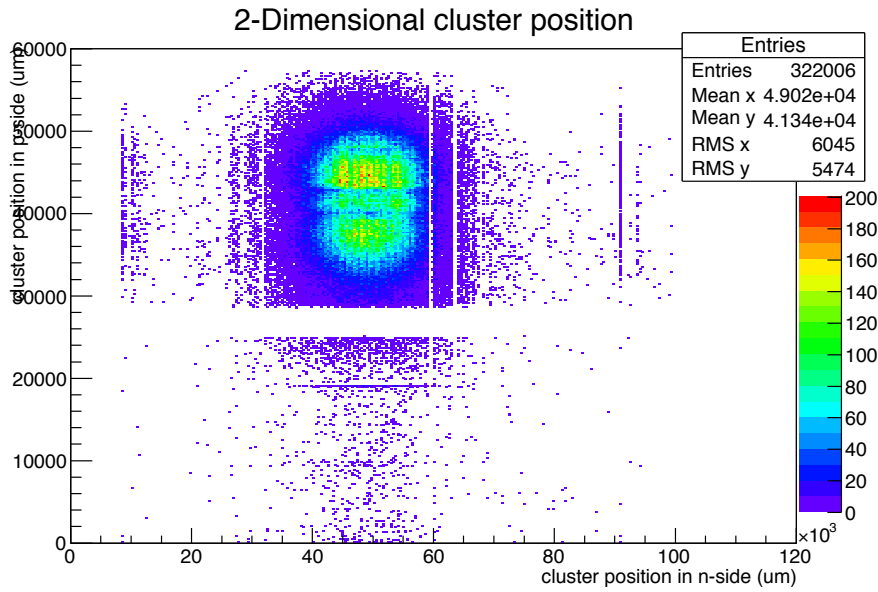


Figure B.1: Single-DSSD readable module Hit map on the sensor. Horizontal axis indicates for n-side and vertical axis indicates for p-side. Unit of the length is μm .

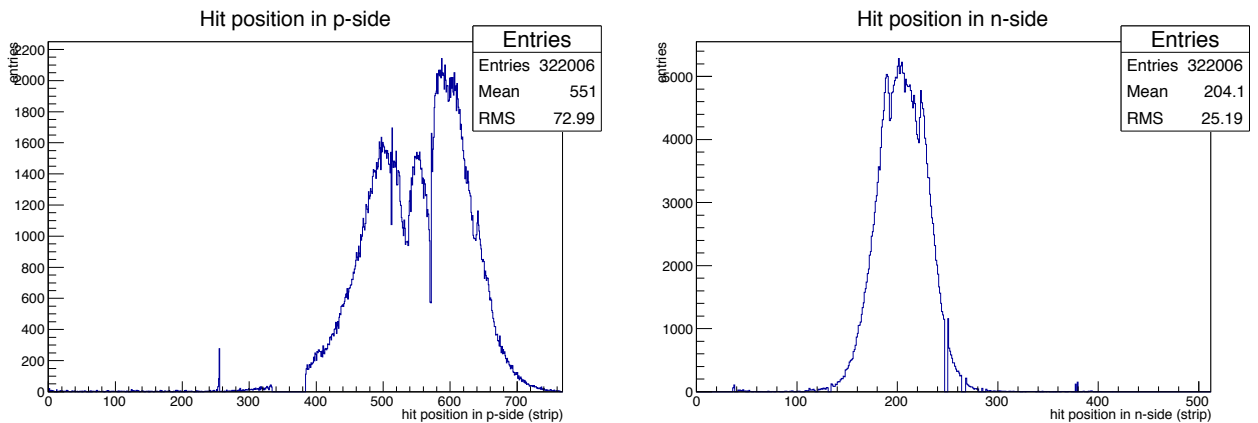


Figure B.2: Distribution of a clustered position. Right is for n-side and left is for p-side.

Next, we see the cluster charge for p and n-side as shown in Figs. B.3, B.4. B.5

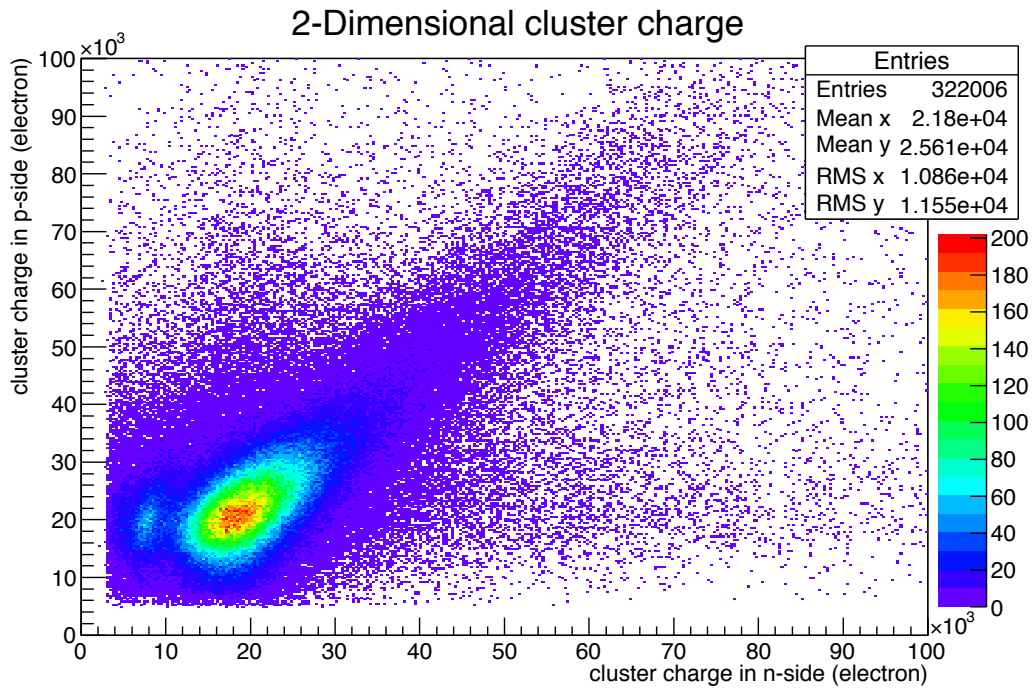


Figure B.3: Single-DSSD readable module : Cluster charge map. Horizontal axis indicates for n-side and vertical axis indicates for p-side. Unit is electron.

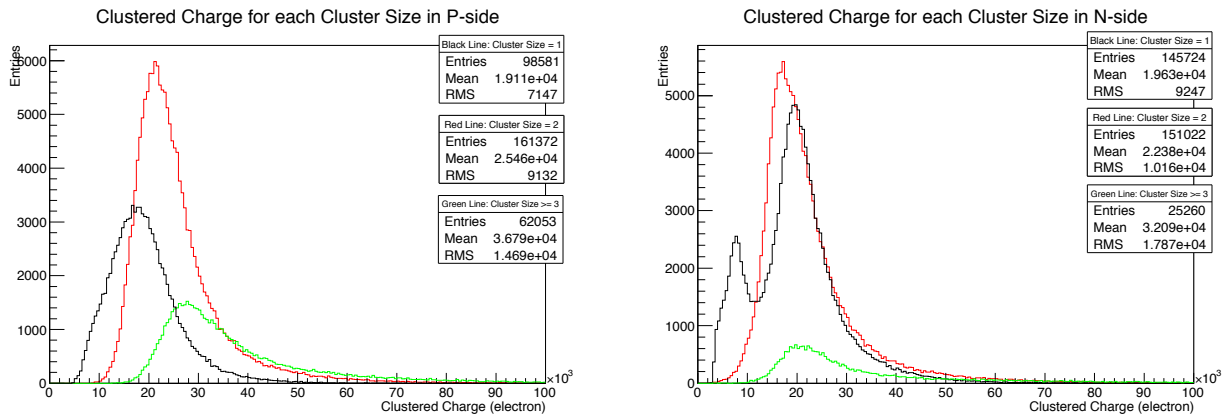


Figure B.4: Distribution of cluster charge of Single-DSSD readable module. Left is for p-side and right is for n-side. Black is cluster size = 1, red is = 2, and green is ≥ 3 .

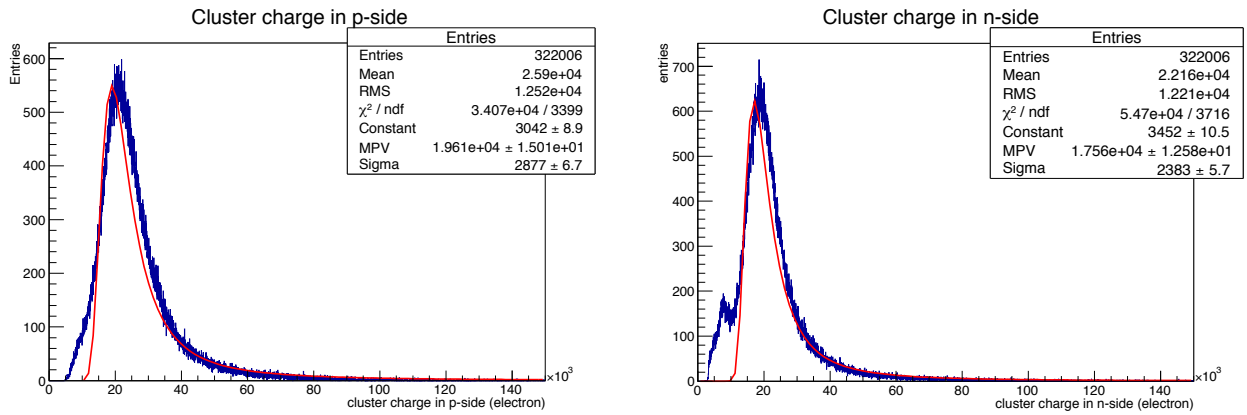


Figure B.5: Distribution of cluster charge of Single-DSSD readable module. Left is for p-side and right is for n-side.

Next, Fig. B.6, B.7 shows the distribution of SNR .

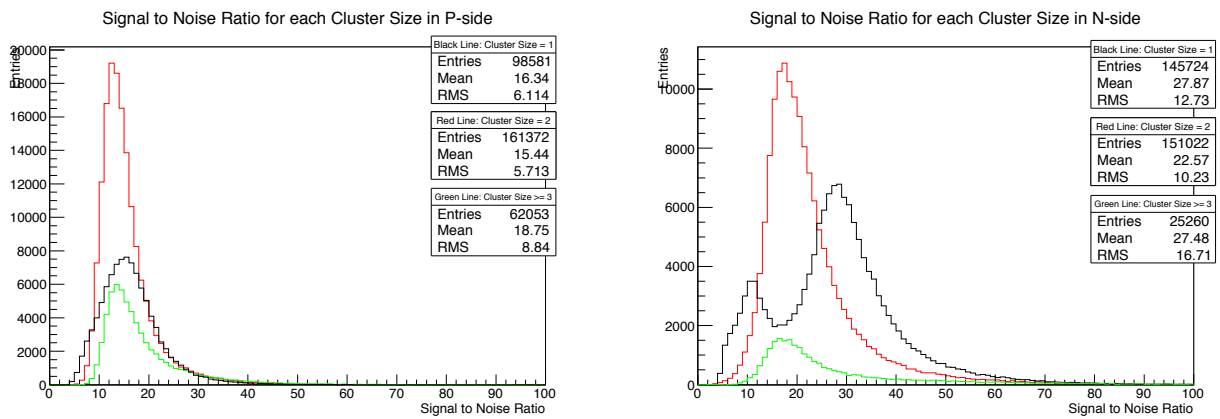


Figure B.6: Signal to noise ratio of Single-DSSD readable module. Left is for p-side and right is for n-side. Black is cluster size = 1, red is = 2, and green is ≥ 3 .

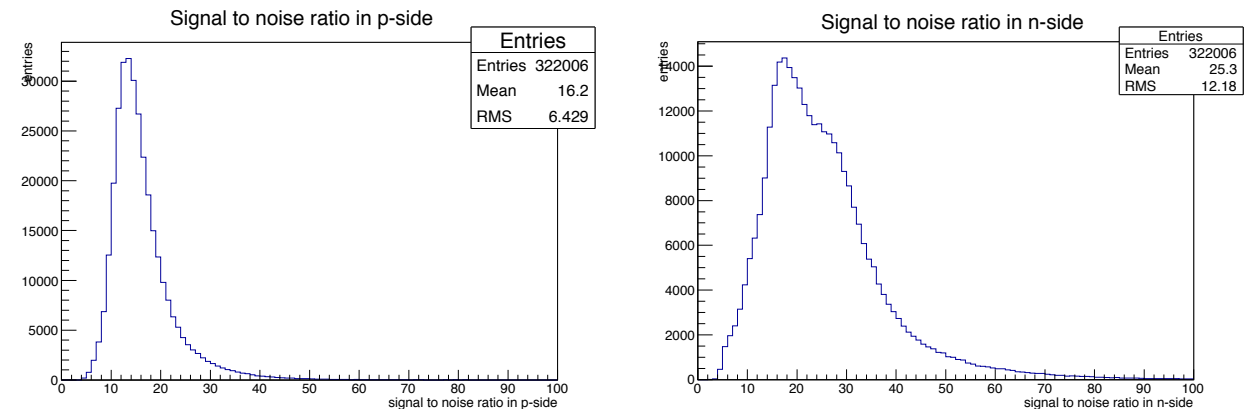


Figure B.7: Signal to noise ratio of Single-DSSD readable module. Left is for p-side and right is for n-side.

We calculated this SNR from the averaged noise by Gaussian fit as shown in Fig. B.8. Then we applied the formulae of SNR described in Chapter. 8.

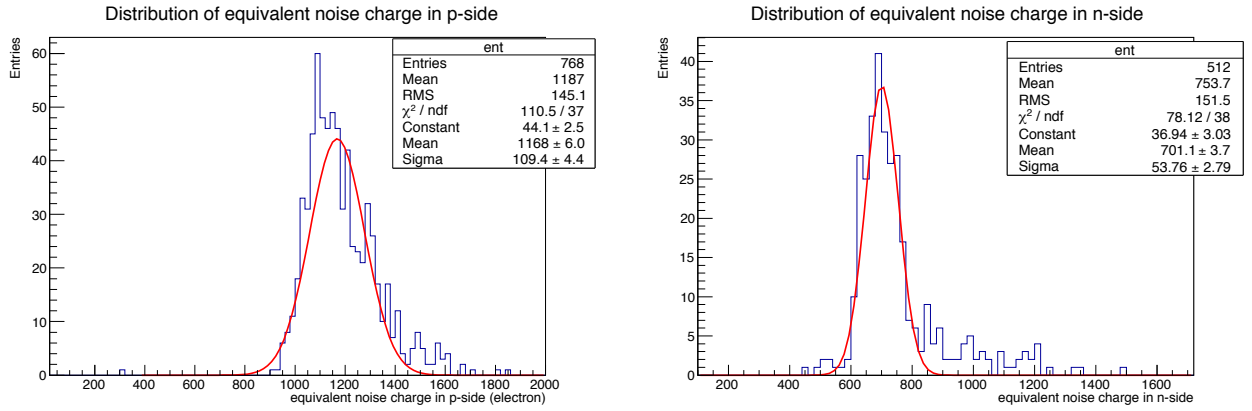


Figure B.8: Equivalent noise charge of Single-DSSD readable module. Left is for p-side and right is for n-side.

Next, Fig. B.9 shows the distribution of cluster size.

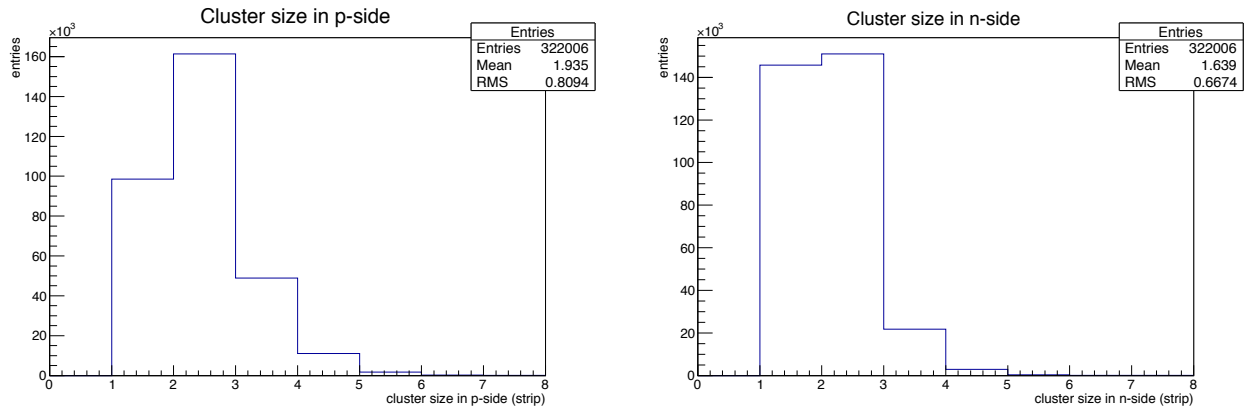


Figure B.9: Cluster size of Single-DSSD readable module.

As the summary of these results, following list (Tab. 8) is obtained by the source test in the Single-DSSD readable module. We calculated 1 MIP energy by multiplying 3.6 eV (energy to produce the e-h pair) by the most probable cluster charge.

Table 8: Single-DSSD readable module : Summary of result in β -ray source test.

Side	p-side	n-side	unit
Most probable cluster charge	19600	17600	hole or electron
Mean SNR	16	25	no unit
Cluster size	1-3	1-3	strip
Measured 1 MIP energy	71	63	keV

C Class-D Ladder : Detail Analysis in β -ray Source Test

In Chapter. 8, we only saw the method of EQA. We did not discuss the obtained data in detail. For example, the result of t_{peak} , τ , and the fitness of Landau function to the obtained data of cluster charge.

C.1 Distribution of Peaking Time

Next histograms shown in Fig. C.1 are the distribution of peaking time of p and n-side.

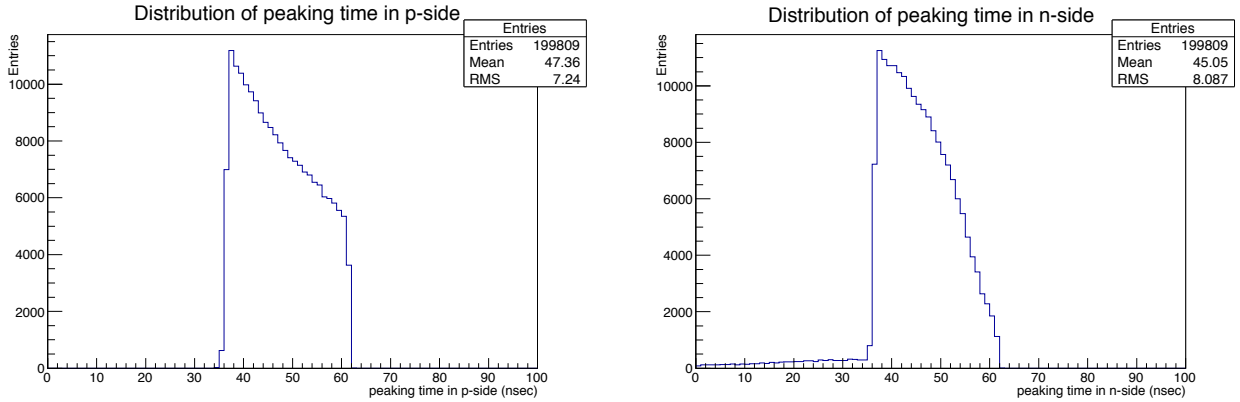


Figure C.1: Distribution of a peaking time before adjusting the timing. Left is for p-side and right is for n-side.

In p-side, there is no tail while n-side has a long tail. First we doubted that the timing of ADC sampling was not good. If so, we can solve this tail problem by adjusting the timing of the data-sampling. After confirming this problem, we checked the timing of the ADC sampling and found the timing was not good. Then we adjusted the timing of sampling as shown in Fig. C.2.

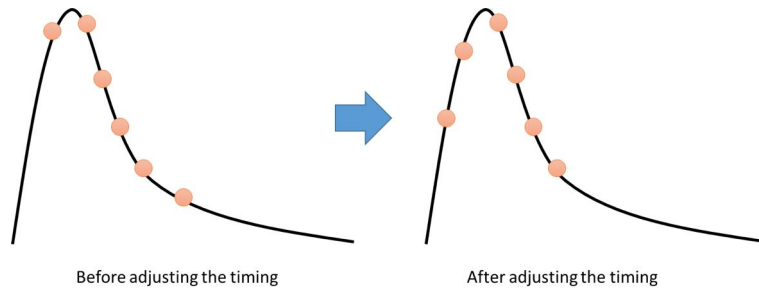


Figure C.2: The timing of sampling the data. Left is before adjusting the timing, and right is after adjusting the timing.

After adjusting the timing, the distribution of peaking time becomes flatter as shown in Fig. C.3. As result shown in Fig. C.3, there is no tail in the distribution of peaking time after adjusting the timing. According to the research in [16], when two of three samples near the peak are almost same, calculation of peaking time is not done well.

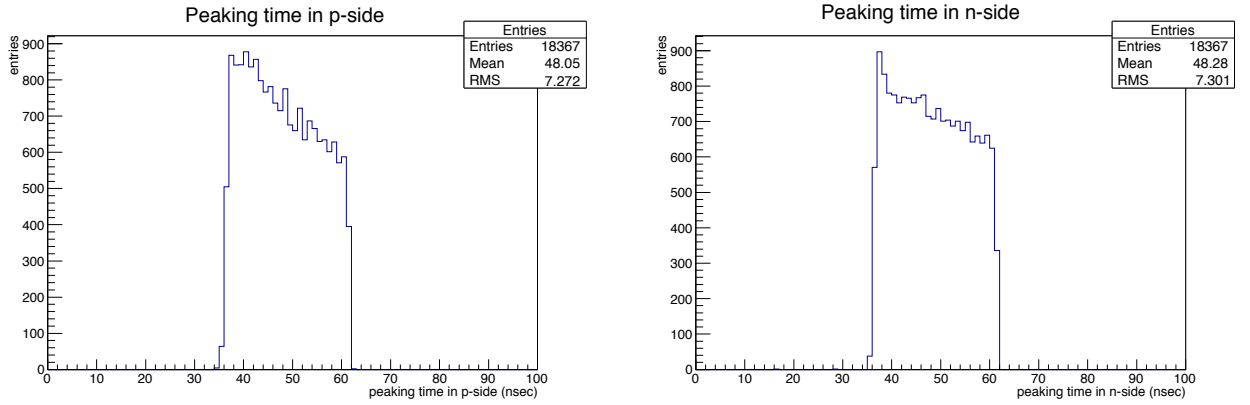


Figure C.3: Distribution of a peaking time after adjusting the timing. Left is for p-side and right is for n-side.

As described in Chapter. 8, we found the peak position within the accuracy of the clock width of 25 nsec. It is therefore expected that the resolution of the peaking time would be $25/\sqrt{12} \sim 7.2$ nsec (The reason why there is the factor of $\sqrt{12}$ is described in Appendix D). The result shown above seems to be consistent.

In our measurement, ^{90}Sr β -ray source is randomly emitted and thus there is no timing adjustment between the timing of emitting the β -ray and the clock of the APV25. We only adjusted the timing between the timing of data-sampling and the trigger timing. Therefore these distributions of peaking time are expected to be flat within around the clock width of 25 nsec. However the results show there is slope in the left side of the distribution and thus not flat.

Actually, the assumed exponential function is not ideal function against to the real output from the sensor. Some reasons are pointed out about this method [16]; this exponential function shown above is got by assuming the dirac delta as the input. This may cause the not good fitting value of the peaking time. Considering seriously, the dirac delta input is not realizable because it has infinite pulse height and infinitesimal width. However in the real signal has the finite pulse height and the finite width. Using this exponential function might cause different results. In actual, the shape of calibration curve taken by ‘‘Internal Calibration Scan’’ is little different from the exponential function as shown in Fig. C.4; the real data is not fit near the maximum point of the exponential function, but fit to calibration curve.

We used following formulae as the fitting function.

$$f(t) = 0 \quad (t < t_{peak} - \tau) \quad (\text{C.1})$$

$$f(t) = A \frac{t - t_{peak} + \tau}{\tau} \exp\left(-\frac{t - t_{peak} + \tau}{\tau}\right) \quad (t > t_{peak} - \tau) \quad (\text{C.2})$$

The calibration curve shown in Fig. C.4 (black curve) is obtained by connecting each point with a cubic spline.

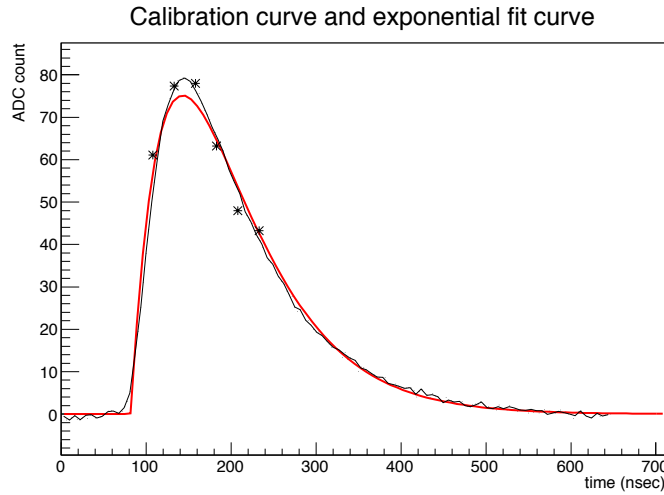


Figure C.4: Calibration curve (black) and exponential fit curve (red). There are six points taken by the APVDAQ.

Although there is a problem about the method of fitting, we used this calculation method for calculating fitted pulse height. This method seems to be successfully done as shown in the result in Chapter. 8, but not for the hit timing.

C.2 Distribution of shaping time

Fig. C.5 shows the distribution of shaping time for p and n-side.

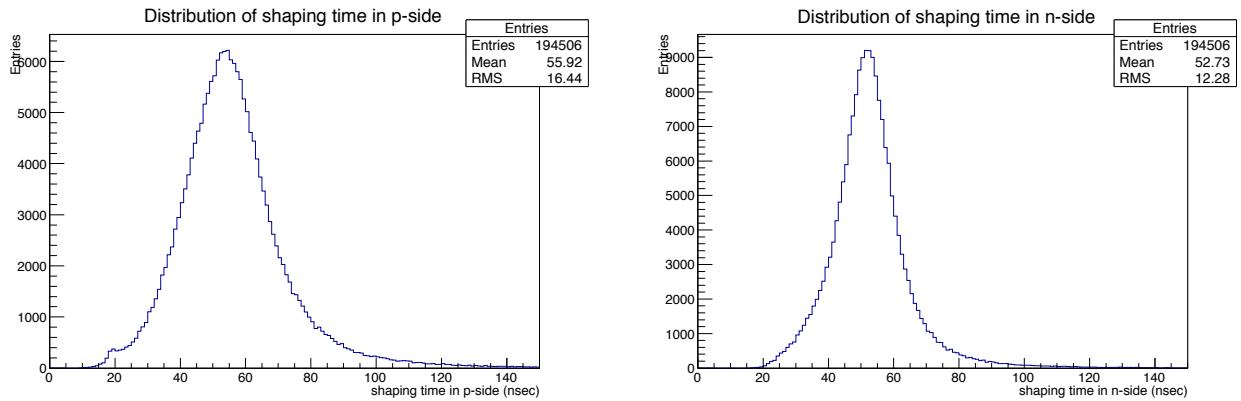


Figure C.5: Distribution of a shaping time. Left is for p-side and right is for n-side.

The shaping time in p-side is larger than that of n-side.

C.3 Landau Fit for the Distribution of Cluster Charge

In Chapter. 8, we used the distribution of cluster charge whose cluster size is 1. In this section, we only see the result whose cluster size is ≥ 2 . By using the software for the fitting

in ROOT [13] developed by Conseil European pour la Recherche Nuclaire (CERN) [15], we performed the Landau fit.

Fig. C.6 shows the distribution of cluster charge in p-side.

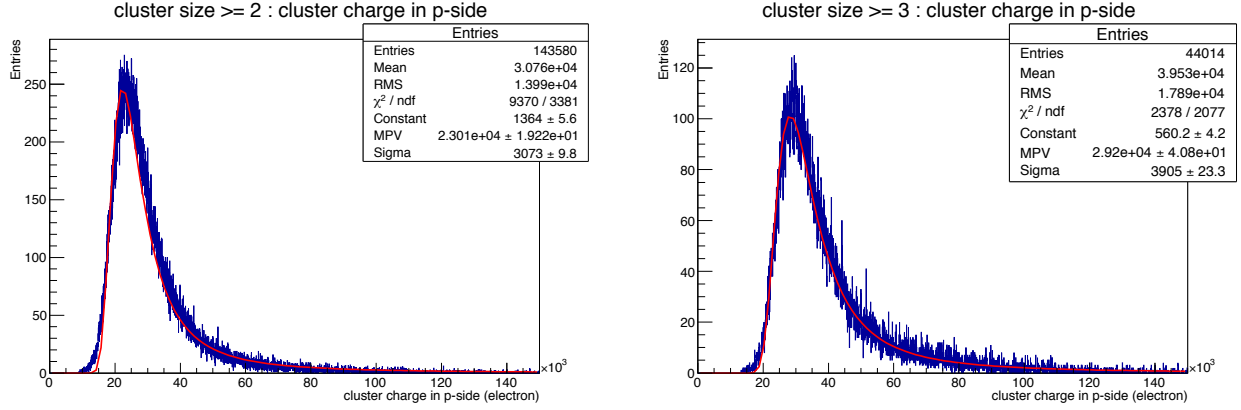


Figure C.6: Distribution of cluster charge in p-side. Red line is the Landau fitted curve.

As this result indicates, the curve of cluster size 3 is fitted better than that of cluster size 2. Next, Fig. C.7 shows a case of n-side.

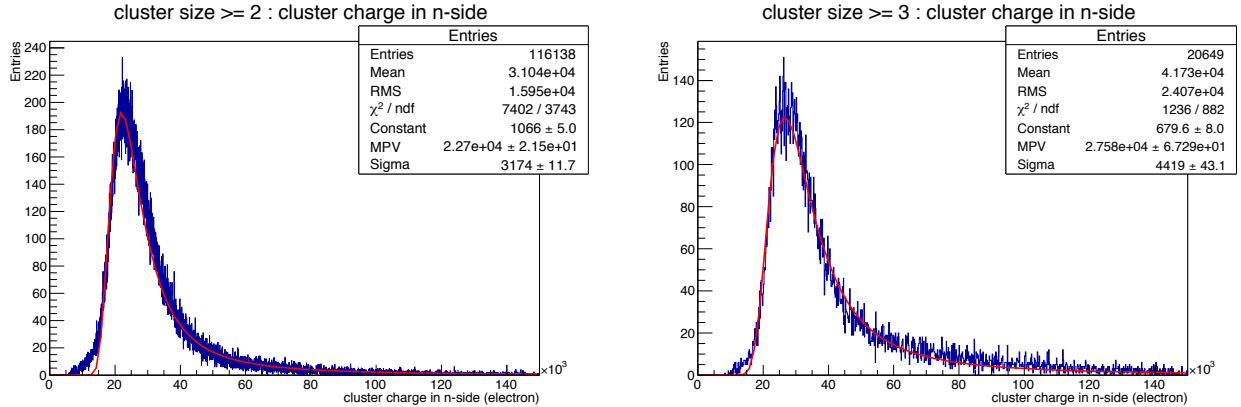


Figure C.7: Distribution of cluster charge in n-side. Left is a case of cluster size ≥ 2 , and right is a case of cluster size ≥ 3 . Red line is the Landau fitted curve.

In n-side, the curve of cluster size 3 is fitted better than that of cluster size 2. From these results, we confirmed the distribution of cluster charge is fitted to the Landau function. This is consistent result because in our setup, we only use the event when the electron penetrates the DSSD as described in Chapter. 8. If the electrons lose the all kinetic energy in the DSSD, the shape of distribution can be Gaussian-like. However, in our case, electron does not lose its all kinetic energy; electron loses part of its energy.

C.4 Asymmetry Cluster Charge between P-side and N-side

We investigated the difference of the cluster charge p (Q_p) and n-side (Q_n) for each event. The distribution of this difference ($Q_p - Q_n$) is shown in Fig. C.8.

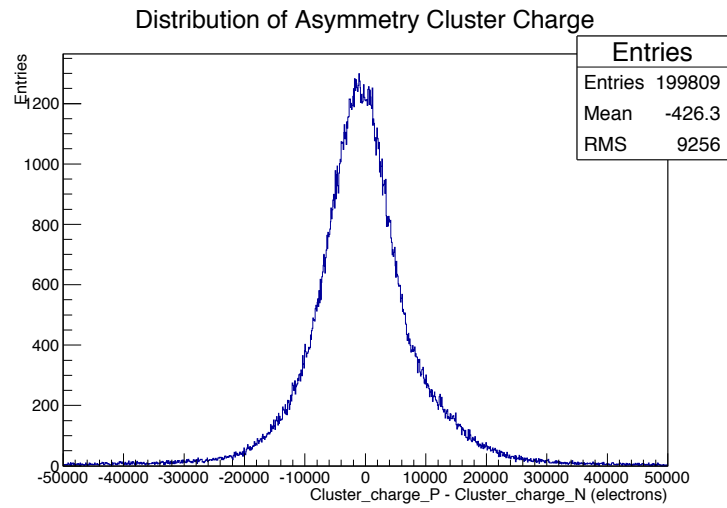


Figure C.8: The distribution of asymmetry cluster charge ($Q_p - Q_n$).

As this result, the difference of the cluster charge between p and n-side shows the peak around -400 electrons; the cluster charge in n-side is higher than that of p-side.

D Noise and Position Resolution of the DSSD

In this section, we see the influence of shot noise and the position resolution of the DSSD.

D.1 Shot noise in the DSSD

Until now, we only saw the noise of capacitive coupling in the APV25. In this section, we see how large shot noise in the DSSD is. The spectral noise density of shot noise is written as following formulae [17].

$$i^2 = 2eI \quad (\text{D.1})$$

Here, i is the shot noise density, e is the charge of electron, and I is the current of DSSD. In our case, the current in the DSSD becomes $\sim 10 \mu\text{A}$. Converting the current into the charge, we can know how many electrons are generated in the DSSD as the noise. The unit of A is $\text{A} = \text{C} \cdot \text{s}$. Converting the unit C into the number of electrons, we obtain the number of electron 6.24×10^{18} . Applying this value to the Eq. D.1, and assuming that the current in the DSSD is $10 \mu\text{A}$, we obtain the noise charge of shot noise as follows.

$$\begin{aligned} i^2 &= 2e \times 10 \mu\text{A} \\ &= 2 \times (10 \times 10^{-6}) \times 6.24 \times 10^{18} e \\ &\sim 1.2 \times 10^{14} e \end{aligned} \quad (\text{D.2})$$

From this result, we obtain $i \sim 10^7 e$. If we assume the Poisson distribution and the RMS of i is the noise, ENC of shot noise becomes $\sqrt{i} \sim 3 \times 10^3 e$. Next, we assume this total charge is distributed in each strip in the DSSD. Then we obtain the ENC for each strip as follows.

$$ENC_{\text{p-side}} = \frac{3 \times 10^3 e}{768 \text{ (the number of strips in p-side)}} \sim 4 e \quad (\text{D.3})$$

$$ENC_{\text{n-side}} = \frac{3 \times 10^3 e}{512 \text{ (the number of strips in n-side)}} \sim 6 e \quad (\text{D.4})$$

Comparing this result to the ENC by capacitive coupling described as $ENC(e) = 246 + 36/\text{pF}$, this shot noise is not the crucial factor for the total noise.

However, if the temperature in the DSSD becomes higher, the current increases as follows [17].

$$I_R \propto T^2 \exp\left(-\frac{E_g}{2kT}\right) \quad (\text{D.5})$$

Here, T is the temperature (K), E_g is the band gap energy of silicon thus $E_g = 1.12 \text{ eV}$, and $k = 1.38 \times 10^{-23} \text{ J/K}$ is a Boltzmann constant. In actual, the DSSD becomes hotter because of the heat from APV25s [7]. We will use a CO2 cooling pile to cool down the APV25s in the Belle II experiment.

If the temperature of DSSD becomes from 300 K to 330 K, then the current becomes

$$\frac{330^2 \times \exp(-\frac{E_g}{2k \times 330})}{300^2 \times \exp(-\frac{E_g}{2k \times 300})} \sim 8.6 \text{ times} \quad (\text{D.6})$$

According to [7], the temperature of APV25 became 67.7 degree when the APV25s are uncooled. Comparing the result when the APV25s are cooled down (-8.5 degree) to the result when APV25s are uncooled (67.7 degree), the shot noise will be lager and non-negligible if we assume the formulae Eq. D.5.

D.2 Position Resolution of the DSSD

In general, the position resolution of the strip sensor is determined by its pitch width p as following formulae. We assume the uniform distribution.

$$\sigma = \sqrt{\frac{\int_{-p/2}^{p/2} x^2 dx}{\int_{-p/2}^{p/2} dx}} = \frac{p}{\sqrt{12}} \quad (\text{D.7})$$

In case of DSSD, the position resolution becomes

$$\sigma_{\text{p-side}} = \frac{75 \mu\text{m}}{\sqrt{12}} \sim 22 \mu\text{m} \quad (\text{D.8})$$

$$\sigma_{\text{n-side}} = \frac{240 \mu\text{m}}{\sqrt{12}} \sim 70 \mu\text{m} \quad (\text{D.9})$$

Considering to take the center of mass of charge as described in Chapter. 8, the hit position X is written by

$$X = \frac{\sum_i x_i Q_i}{\sum_i Q_i} \quad (\text{D.10})$$

x_i is the position of clustered channel and Q_i is the clustered charge in the strip i . For example, if the charged particle passes through between strip 1 - 2 and generated electrons or holes are collected by strip 1 and strip 2, the hit position is written by

$$X = \frac{x_1 Q_1 + x_2 Q_2}{Q_1 + Q_2} \quad (\text{D.11})$$

In Chapter. 8, we discussed the SNR . This SNR is important to measure the X precisely. The resolution of X (σ_X) is explained by following formulae [18],

$$\begin{aligned} \sigma_X^2 &= \left(\frac{\partial X}{\partial Q_1}\right)^2 (\sigma_{Q_1})^2 + \left(\frac{\partial X}{\partial Q_2}\right)^2 (\sigma_{Q_2})^2 + 2\text{cov}(Q_1, Q_2) \frac{\partial X}{\partial Q_1} \frac{\partial X}{\partial Q_2} \\ &= \left(\frac{(x_1 - x_2)Q_2}{(Q_1 + Q_2)^2}\right)^2 (\sigma_{Q_1})^2 + \left(\frac{(x_2 - x_1)Q_1}{(Q_1 + Q_2)^2}\right)^2 (\sigma_{Q_2})^2 + 2\text{cov}(Q_1, Q_2) \frac{(x_1 - x_2)Q_2}{(Q_1 + Q_2)^2} \frac{(x_2 - x_1)Q_1}{(Q_1 + Q_2)^2} \end{aligned} \quad (\text{D.12})$$

Here, $\text{cov}(Q_1, Q_2)$ is defined as the expectation value of $(Q_1 - \langle Q_1 \rangle)(Q_2 - \langle Q_2 \rangle)$ and thus $\text{cov}(Q_1, Q_2) \equiv E((Q_1 - \langle Q_1 \rangle)(Q_2 - \langle Q_2 \rangle))$. Also, if we assume $x_2 > x_1$, then $x_2 - x_1$ correspond to the pitch width p . Now, we consider $Q_1 + Q_2$ is the signal S and σ_{Q_i} is the noise N_i . We therefore obtain the formulae

$$\sigma_X^2 = \left(-p \frac{Q_2}{S}\right)^2 \left(\frac{1}{S/N_1}\right)^2 + \left(p \frac{Q_1}{S}\right)^2 \left(\frac{1}{S/N_2}\right)^2 - 2p^2 \text{cov}(Q_1, Q_2) \frac{Q_1}{N_1} \frac{Q_2}{N_2} \frac{N_1 N_2}{S^4} \quad (\text{D.13})$$

To estimate σ_X simply, we consider the simple case; we ignore third term. We thus get

$$\sigma_X^2 = \left(-p \frac{Q_2}{S}\right)^2 \left(\frac{1}{S/N_1}\right)^2 + \left(p \frac{Q_1}{S}\right)^2 \left(\frac{1}{S/N_2}\right)^2 \quad (\text{D.14})$$

Assuming that the generated charges are collected by two strips equally; for example, we consider the case when $N_1 = N_2 = 1000 e$, $Q_1 = 5000 e$, $Q_2 = 5000 e$, and $S = 10000 e$. We therefore get

$$\sigma_X \sim 5.3 \mu\text{m} \quad \text{for p side} \quad (\text{D.15})$$

$$\sigma_X \sim 16.8 \mu\text{m} \quad \text{for n side} \quad (\text{D.16})$$

Assuming $N_1 = N_2 = 1000 e$, $Q_1 = 15000 e$, $Q_2 = 15000 e$, and $S = 30000 e$, we get

$$\sigma_X \sim 1.7 \mu\text{m} \quad \text{for p side} \quad (\text{D.17})$$

$$\sigma_X \sim 5.4 \mu\text{m} \quad \text{for n side} \quad (\text{D.18})$$

Assuming $N_1 = N_2 = 1000 e$, $Q_1 = 25000 e$, $Q_2 = 25000 e$, and $S = 50000 e$, we get

$$\sigma_X \sim 1.1 \mu\text{m} \quad \text{for p side} \quad (\text{D.19})$$

$$\sigma_X \sim 3.4 \mu\text{m} \quad \text{for n side} \quad (\text{D.20})$$

These resolutions are better than the estimated value of Eq. (D.8), (D.9).

Since we have not measured the $\text{cov}(Q_1, Q_2)$, we ignored the third term of Eq. D.13; if this third term becomes larger, the position resolution would be worse. Also, we are now considering the case when the cluster size = 2. If the charged particle passes through the DSSD not vertically and the cluster size becomes larger, the position resolution would be worse. As this result, we can see high SNR is important to measure the hit position precisely.

Acknowledgements

In my research of SVD, every time I was supported by all kind member in the SVD, but also my friends. Remembering all time I spent in this two years, there were many unforgettable things.

First, all of my researches were started when my supervisor Prof. H. Aihara gave me the chance of research of the SVD. Before I started the research of the SVD, Aihara-san gave me a lot of advices so that I can learn the physics and electronics. Furthermore, when I was not able to speak and hear English at all, Aihara-san gave me a lot of opportunity that I can communicate with many friends come from all over the world. Such a opportunity played a crucial role for me. Although my skill of English was *never* good in that time, I acquired that skill gradually. Without such a opportunity, I could not try to speak English, but also to improve my posture forward to the research. In actual, that acquired skill enables me to communicate with the members of the SVD coming from overseas. Aihara-san always gave me a lot of opportunities. Thank you very much Aihara-san.

Also, I would like to thank Prof. S. Yamashita and Prof. J. Tanaka for checking my master thesis. Thank you very much.

Prof. Y. Onuki and Prof. T. Higuchi gave me the opportunity to learn the APVDAQ in Austria. I also did not know how to learn this system at all; furthermore, I did not know C++ programming cord at all. In that time, Higuchi-san gave me very important lecture about the programming very kindly. Also Prof. C. Imler and F. Markus also gave me a lot of important opportunities and a lot of tools of APVDAQ. They are always very kind to us, I was very supported by them. Without their help and kindness, I could not accomplish my research with APVDAQ. Danke schön.

After coming back to Japan, Prof. T. Tsuboyama gave me enormous opportunities so that I can learn electronics of the SVD. Also, Tsuboyama-san gave me a lot of important and educational advices during this two years, which must be very important for my whole life. Without his kindness, if there was no chance to meet him, I could not learn the electronics of the SVD, but also I could not get the confidence in my research.

Prof. K. Hara and Prof. K. Nakamura helped me every time. They told me a lot of things to accomplish my research. Although I was not able to analyze the data of the DSSD, Nakamura-san and other members in the SVD kindly told me how to analyze the data of the β -ray source test, which is described in Chapter. 8.

In the IPMU, I was supported by T. Higuchi-san, N. Sato-san, T. Morii-san, Y. Seino-kun, and T. Yoshinobu-kun. When we assembled the Single-DSSD readable module and class-D ladder, they supported my research to perform the assembly level EQA and whole assembly level EQA, which are described in Chapter. 7, 8. Although we were in hurry that time, they allowed me to spend the time for my research. I really appreciate their kindness. The time spent with them must be the unforgettable memories for me.

From Korea, Prof. S. Uozumi, H. Jeon, C. Joo, and K. Kang strongly supported me. When I was studying the EQA procedure, C. Joo told me the detail of the behavior of the strips in the DSSD, but also he told me a lot of things of the APV25 and the APVDAQ. Uozumi-san, H. Jeon, and K. Kang helped us when we were studying the Single-DSSD readable module. That is especially that we were able to proceed to the next step of the study.

When I started my research, I did not know about the SVD at all; every time, I made uncountable mistakes. In such a situation, N. Shimizu-san supported me when I was struggling to solve the problems. Thanks to his help, I understood the assembly of SVD ladder gradually. He supported me every time, and I was able to learn a lot of things.

Onuki-san and one student Mitsutaka Nakao also helped us when we prepare the

whole setup of the β -ray source test. Almost all the setup was prepared by Onuki-san and Nakao-kun. That is especially why I was able to write the contents of the β -ray source test. Without the help from Onuki-san, Nakao-kun, and other members of the SVD, I could not only finish the analysis of the data, but also I could not study the detail of the DSSD.

Also, when I started to write this thesis, all members in the SVD strongly supported me. Every time they gave me a lot of advices, which is very important for me to learn how to write the paper in English.

In the University of Tokyo, I would like to thank all members in this laboratory. Thank you very much H. Aihara-san, E. Denis-san, M. Yokoyama-san, Y. Onuki-san, K. Kono-san, S Mineo-san, N. Clement-san, N. Shimizu-san, Y. Suda-san, T. Koga-kun, H. Niikura-san, N. Chikuma-kun, H. Hosomi-kun, Y. Jin-kun.

Finally, I would like to thank my family and all friends in my hometown. My family and my friends always encouraged me since I was a high school student. When I was worrying whether I should enter the university or not, I was encouraged by my family and I was able to decide my way. All of their kindness gave me strong confidence, and this confidence enables me to enter the Yokohama National University (YNU); before I enter the University of Tokyo as the graduate student, I was the undergraduate student of YNU. Furthermore, when I was worrying whether I should change the department from engineering to physics, many advices from my family and my friends strongly helped me. Without their encouragement, I would already gave up to enter the department of physics in the University of Tokyo when I was the student of YNU. But now, I am the student of the physics, and I was able to spend my time towards to my dream.

References

- [1] T. Aushev *et al.*, arXiv:1002.5012 [hep.ex]
- [2] G. C. Branco *et al.*, arXiv:1106.0034 [hep-ph]
- [3] <http://belle2.kek.jp/>
- [4] <http://www.hep.princeton.edu/~marlow/svd/va1/va1ta.pdf>
- [5] Y. Nakahama / Research and Development of a Pipeline Readout System for the Belle Silicon Detector (2006)
- [6] M.J. French *et al.*, Nucl. Instrum. Meth. **A466** (2001) 359.
- [7] Belle II technical design report (arXiv:1011.0352)
- [8] <http://legacy.kek.jp/newskek/2003/mayjun/svd.html>
- [9] AirexAG(Switzerland) www.airexag.ch.
- [10] R. Bainbridge *et al.*, Nucl. Instrum. Meth. **A543** (2005) 619-644
- [11] APVDAQ reference manual /
http://www.hephy.at/project/electronic2/PDF/ARCHIV/BELLE/APVDAQ/V1/apvdaq_reference_manual.v0.06.pdf
- [12] N. Shimizu / Development of the Silicon Vertex Detector for Belle II experiment
- [13] <https://root.cern.ch/>
- [14] American Physical Society / Physical Review D (2012) 385
- [15] <http://home.web.cern.ch/>
- [16] Christian Irmeler / Upgrade Studies for the Belle Silicon Vertex Detector (2008)
- [17] Helmuth Spieler / Semiconductor Detector Systems (OXFORD SCIENCE PUBLICATIONS)
- [18] W. R. Leo / Techniques for Nuclear and Particle Physics Experiments